The Interplay of Orography, Aerosols, and Secondary Ice Production in Shaping Clouds and Precipitation over Contrasting Island Environments

Master's Thesis in
Meteorology and Climate Physics
by

Bhawuk Verma

January 2026

INSTITUTE OF METEOROLOGY AND CLIMATE RESEARCH
KARLSRUHE INSTITUTE OF TECHNOLOGY (KIT)

Advisor:	Prof. Dr. Corinna Hoose
Co-Advisor:	Prof. Dr. Michael Kunz
Supervisors:	Dr. Gabriella Wallentin, Dr. Christian Barthlott

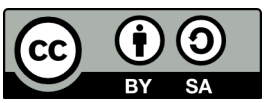

Abstract

This study investigates the combined effects of orography, aerosol concentration, and secondary ice production (SIP) on cloud microphysics and surface precipitation in contrasting island environments of Corsica and Iceland. Orography plays a crucial role in initiating convection and influencing precipitation patterns. Aerosols act as a seed for cloud formation and SIP increases the ice crystal number concentration. Simulations are performed with the convection-permitting ICOsahedral Non-hydrostatic (ICON) model at 1 km grid spacing for three days. Two deep-convective cases over Corsica and one stratiform case over Iceland are chosen. Reference (or original) orography is systematically scaled from flat terrain to idealized mountain heights of 1, 2, 3, and 4 km. Aerosol perturbations are represented by four different concentrations of cloud condensation nuclei (CCN). SIP is included via rime splintering, droplet shattering, and ice–ice collisional breakup.

The results are analyzed in a sequential way that isolates (i) orographic effects under fixed CCN concentration without SIP, (ii) CCN concentrations sensitivity at 1 and 3 km scaled orography without SIP, and (iii) the changes in these sensitivities when SIP is activated. Over Corsica, pre-convective and convection initiation mechanism respond systematically to increasing terrain height, but the timing, location, and organization of convection differ between the two days. Over Iceland, where thermally driven circulations are weak, a frontal passage case is analyzed and surface precipitation increases linearly with orography scaling. Analysis of the three cases reveals that surface precipitation sensitivity to CCN concentrations differs between the two domains. Over Iceland, increasing CCN concentrations consistently suppresses surface precipitation across both orographic scalings, but over Corsica, the response varies between cases and depends on whether warm-rain or cold-rain microphysical processes dominate. However, taller mountains consistently increase the surface precipitation over both island domains (at every CCN concentration).

Activating SIP produces distinct effects in the two domains. Over Iceland, SIP enhances precipitation across all CCN concentrations and orographic scalings. This is linked to the strengthening of the microphysical pathways responsible for precipitation formation. For Corsica, SIP impacts are strongly dependent upon the dominating microphysical pathways. In the cold-rain dominated case, SIP enhances precipitation significantly at low CCN concentrations, but has little effect at high CCN concentrations across both 1 and 3 km scalings, while the warm-rain dominated case exhibits a more complex and non-linear response. Overall, the results demonstrate that representing SIP can substantially alter microphysical pathways and precipitation outcomes, and that the combined sensitivities to orography and CCN concentrations depend on the prevailing cloud regime. These results emphasize the necessity to represent SIP processes in numerical models. This work

highlights the importance and non-linear impacts of SIP. Further understanding of SIP processes, especially in convective clouds, is vital for future modelling of these clouds.

Zusammenfassung

Diese Studie untersucht die kombinierten Auswirkungen von Orografie, Aerosolkonzentration und sekundären Eisbildungsprozessen auf die Wolkenmikrophysik und den Niederschlag am Boden in zwei unterschiedlichen Inselregionen (Korsika und Island). Die Orografie spielt eine entscheidende Rolle bei der Auslösung von Konvektion und der Beeinflussung von Niederschlagsmustern. Aerosole fungieren als Wolkenkondensationskerne (CCN) und stellen damit die „Keime“ für die Wolkentropfenbildung bereit; sekundäre Eisproduktion (SIP) erhöht die Anzahlkonzentration von Eiskristallen. Die Simulationen werden mit dem konvektionserlaubenden ICOsahedral Non-hydrostatic (ICON) Modell bei einem Gitterabstand von 1 km für drei reale Fallstudien durchgeführt. Es werden zwei Fälle mit hochreichender Konvektion über Korsika und ein stratiformer Fall über Island ausgewählt. Die Referenz- (oder ursprüngliche) Orografie wird systematisch von flachem Gelände auf idealisierte Berghöhen von 1, 2, 3 und 4 km skaliert. Aerosolperturbationen werden durch vier verschiedene Konzentrationen von Wolkenkondensationskernen dargestellt. SIP werden über Raureifsplitterung (Hallett–Mossop-Prozess), Tropfenzersplitterung beim Gefrieren und Eis–Eis-Kollisionsbruch einbezogen.

Die Ergebnisse werden sequenziell analysiert, wobei (i) orografische Effekte bei fester CCN-Konzentration ohne SIP, (ii) die Sensitivität bezüglich der CCN-Konzentrationen bei 1 und 3 km skalierter Orografie ohne SIP und (iii) die Änderungen dieser Sensitivitäten bei Aktivierung von SIP. Über Korsika reagieren die präkonvektiven Bedingungen und Mechanismen der Konvektionsauslösung systematisch auf die zunehmende Geländehöhe, aber der Zeitpunkt, der Ort und die Organisation der Konvektion unterscheiden sich zwischen den beiden Tagen. Über Island, wo thermisch angetriebene Zirkulationen schwach sind, wird ein Fall mit Frontdurchgang analysiert. Die Niederschläge an der Oberfläche nehmen hier linear mit der Orographieskalierung zu. Die Analyse der drei Fälle zeigt, dass sich die Sensitivität der Niederschläge an der Oberfläche auf CCN-Konzentrationen zwischen den beiden Gebieten unterscheidet. Über Island unterdrückt eine Zunahme der CCN-Konzentrationen durchweg die Niederschläge, während über Korsika die Reaktion zwischen den Fällen variiert und davon abhängt, ob Warm- oder Kaltregenprozesse die mikrophysikalischen Prozesse dominieren. Eine Zunahme der orografischen Skalierung erhöht jedoch durchweg die Niederschläge über beiden Inseln (bei jeder CCN-Konzentration).

Die Aktivierung von SIP zeigt in den beiden Gebieten unterschiedliche Effekte. Über Island verstärkt SIP die Niederschläge über alle CCN-Konzentrationen und orografischen Skalierungen hinweg. Dies hängt mit der Verstärkung der mikrophysikalischen Pfade zusammen, die für die Niederschlagsbildung verantwortlich sind. Über Korsika hängen die SIP-Effekte stark von den dominierenden mikrophysikalischen Prozesspfaden der Niederschlagsbildung ab. Im Fall bei dem kalte

Prozesse dominieren, erhöht SIP den Niederschlag bei niedrigen CCN-Konzentrationen deutlich. Es zeigt sich jedoch bei hohen CCN-Konzentrationen sowohl für 1- als auch 3 km-Skalierungen eine nur geringe Wirkung, während im Fall bei dem warme Prozesse dominieren, eine komplexere, nichtlineare Reaktion auftritt. Insgesamt zeigen die Ergebnisse, dass die Darstellung von SIP die mikrophysikalischen Pfade und Niederschlagsergebnisse erheblich verändern kann und dass die kombinierten Sensitivität gegenüber Orografie und CCN-Konzentrationen vom vorherrschenden Wolkenregime abhängen. Die Arbeit zeigt die Notwendigkeit, SIP-Prozesse in numerischen Modellen darzustellen. Diese Arbeit unterstreicht die Bedeutung sowie die nichtlinearen Auswirkungen der sekundären Eisproduktion. Ein tieferes Verständnis der SIP-Prozesse, insbesondere in konvektiven Wolken, ist für die zukünftige Modellierung dieser Wolken entscheidend.

Preface

Generative artificial intelligence (AI) tools (ChatGPT and DeepL) were employed solely for refinement purposes during the preparation of this thesis and outputs were carefully reviewed. In coding, AI (free version ChatGPT) helped identify errors, optimize code and plots quality, and suggest Python functions, which were verified against official documentation. In writing, AI (free version DeepL and Writefull) improved grammatical accuracy, flow and readability through sentence restructuring and vocabulary suggestions. Also, DeepL was used for translating the English abstract to German language. Crucially, AI was not used to generate initial code or written content.

Special thanks to the National High-Performance Computing Center at the Karlsruhe Institute of Technology (NHR@KIT) for providing computing and storage resources.

Contents

1 Introduction

Clouds play a pivotal role in the Earth's climate system (Lamb and Verlinde, 2011). They act as the crucial regulators of radiation (both incoming and outgoing) and water budgets, significantly influencing the planet's energy balance and climate. However, their accurate representation in climate models remains a crucial challenge due to the complex nature of the convection and other sub-grid-scale processes (Forster et al., 2023). Thus, accurately understanding the physical processes governing cloud formation, evolution, and interaction with the surrounding environment is crucial for improving climate predictions and weather forecasting (Lamb and Verlinde, 2011).

Complex terrain strongly modulates regional climate, enhancing precipitation on windward slopes and reducing it on leeward slopes. This contributes to pronounced interannual variability in precipitation and affects regional climate dynamics (Austin and Dirks, 2005; Roe, 2005). Mountains influence atmospheric flow through lifting, deflection, and blocking, thereby affecting the initiation and development of precipitating convection. This was demonstrated during a heavy precipitation episode in the first Special Observation Period (SOP 1) of the Hydrological cycle in the Mediterranean Experiment (HyMeX) (Barthlott and Davolio, 2015; Ducrocq et al., 2013). When terrain elevation was capped at 10 m in the simulation, intense precipitation along the French and Italian coastlines disappeared. This shows that early convection was triggered by coastal orography, as blocking of moist Mediterranean inflow produced a convergence line parallel to the coast. A robust understanding of these mechanisms is therefore essential for improving weather forecasting, climate modelling, and water resource management in complex-terrain regions (Barthlott and Kirshbaum, 2013). Convection initiation and intensification are closely linked to the intricacies of orography, which require improved quantitative representation in models (Kirshbaum et al., 2018). Numerical weather prediction (NWP) models still face major challenges over complex orography, through both terrain representation and orography-related physical parameterizations (Wang and Wu, 2022).

The uplifting of the air masses caused by the orography may interact with the aerosols present in the atmosphere. Aerosols are microscopic particles that can act as cloud condensation nuclei (CCN) or ice nucleating particles (INP) (Seinfeld and Pandis, 2016). This interaction, also known as aerosol-cloud interactions (ACI), influences cloud macrophysical and microphysical properties and can modulate surface precipitation and its spatial distribution (Barthlott and Hoose, 2018; Gordon et al., 2023). The role of aerosol concentration in precipitation formation has become a major research focus (Choudhury et al., 2019), as it serves as a source of uncertainty in predicting the effect on parameters such as radiation and near-surface temperature (Seifert et al., 2012). Several studies have been conducted in the past to understand how aerosols influence convection and precipitation (Fan et al., 2016; Tao et al., 2007). For example, one study showed that both radiative

and microphysical aerosol effects can lead to either enhanced or reduced rainfall (Rosenfeld et al., 2008). Another study assessed aerosol effects together with land-surface uncertainty via soil moisture to quantify impacts on convective precipitation (Barthlott et al., 2022a). They found a consistent positive soil moisture–precipitation feedback across scenarios, independent of synoptic forcing. However, aerosol impacts differed between weak and strong forcing, further underscoring the complex relationship between aerosols and precipitation. Thus, an improved understanding of ACI is essential for accurate future climate projections.

Mixed-phase clouds contain both liquid water and ice particles. Deep convective clouds are one of the most common types of mixed-phase clouds, with liquid phase layers at the bottom and ice only at the top, and a mixed-phase region in between. Secondary ice production (SIP) is a crucial process happening within the mixed-phase layers of these clouds. This process significantly impacts ice crystal number concentrations. According to Korolev et al. (2020), multiple mechanisms based on laboratory studies have been proposed: droplet shattering during freezing (Lauber et al., 2018; Mason and Maybank, 1960), rime-splintering (Hallett and Mossop, 1974), collisional breakup of ice crystals (Takahashi et al., 1995; Vardiman, 1978), ice particle fragmentation due to thermal shock (Gold, 1963), fragmentation during sublimation (Oraltay and Hallett, 1989) and INP activation in transition supersaturation around freezing drops (Dye and Hobbs, 1968).

The previous discussion highlights the individual effects of orography and aerosols on convection and precipitation. However, fewer studies have examined their coupled interactions, particularly in island settings with contrasting geography and meteorology such as Corsica and Iceland. This complexity necessitates further research, particularly in understanding the role of different aerosol concentrations in orographic precipitation. Therefore, this thesis investigates how orography influences aerosol–cloud interactions. In addition, although SIP processes can strongly enhance ice crystal number, most weather and climate models still omit SIP in their cloud microphysical schemes (Han et al., 2024). This is especially relevant for the aerosol-cloud interaction studies, where the SIP mechanisms are not considered at all. By incorporating SIP mechanisms, this thesis aims to improve the representation of cloud microphysical processes in aerosol–cloud interaction studies, with a focus on orography–aerosol coupling.

The island domains are chosen because mesoscale surface heterogeneities, here primarily orography, combined with abundant low-level moisture from adjacent water bodies, create favorable conditions for frequent localized convection (Robinson et al., 2008; Wilson and Schreiber, 1986). Using two contrasting islands also allows a targeted comparison of how orography modulates aerosol–cloud interactions across distinct cloud regimes. Over Corsica, the focus is on mixed-phase deep convection, whereas over Iceland the prevailing regime is cold, shallow stratiform cloud.

The Western Mediterranean is also prone to heavy rainfall and flooding in late summer and autumn, with events often exceeding 100 mm within less than 6 h (Ricard et al., 2011; Romero et al., 2000). Despite their impacts, such high-precipitation events remain difficult to forecast operationally. Complex terrain complicates the representation of boundary-layer processes, which in turn limits quantitative precipitation forecasting skill (Barthlott et al., 2011; Hanley et al., 2014). This further

underlines the need for accurate orographic representation in state-of-the-art NWP models over complex-terrain regions.

Against this background, this thesis aims to provide a holistic understanding of the combined effects of orography, aerosol concentration, and secondary ice production mechanisms on precipitation patterns in contrasting meteorological regimes of Corsica and Iceland and seeks to answer the following research questions:

1. How does changing the orographic scaling affect convection and rain initiation, and convective parameters under standard CCN conditions without SIP processes?

2. How does varying CCN concentration modify cloud microphysics and surface precipitation across different orographic scalings in the absence of SIP processes?

3. How does activating SIP processes alter the sensitivity of cloud microphysics and surface precipitation to CCN concentration and orographic scaling?

To address these research questions, the convection-permitting ICOsahedral Non-hydrostatic (ICON) model is used in its Limited Area Model (LAM) configuration. The LAM setup resolves convection explicitly. Flat, 1, 2, 3 and 4 km orography scalings are deployed to investigate the different terrain heights impact on convection initiation. Four CCN concentrations are implemented, spanning from maritime to polluted continental conditions. SIP is represented using three mechanisms: rime splintering, droplet shattering, and collision breakup. However, only 1 and 3 km scaled terrain heights are implemented to assess the CCN and SIP impacts. Three real days are chosen for the simulations. Two days of 27 August 2024 and 04 August 2024 are dedicated to studying deep convection over Corsica. These days are selected because convection initiates over the island during daytime, driven by local breeze circulations that are further modulated by orography. Such conditions have been shown to influence the larger-scale precipitation signal (Fernández et al., 2003; Gao et al., 2006). One day of 07 May 2023 is dedicated to shallow convection in Iceland. Since local breeze-driven convection is less common in Iceland than in Corsica, a day with frontal passage is chosen instead.

This thesis is structured as follows: Chapter **2** delves into the background meteorological information regarding moist orographic convection, ACI, and SIP mechanisms. Chapter **3** describes the data and methods used in this thesis. It provides a detailed explanation of the ICON model configuration, the simulation setup, and the selection criteria for the chosen days. The chapter also explains how orographic scaling, different CCN concentrations, and SIP parameterizations are implemented in the model, and compares the orographic features of both islands. The results are presented in Chapters **4**, **5**, and **6** and are discussed with a sequential approach. These chapters are organized into three parts, each addressing one of the research questions outlined above. Chapter **4** first examines the impact of orographic scaling on convection under constant intermediate CCN conditions and with SIP disabled. Chapter **5** then analyses the sensitivity of precipitation and microphysical processes to varying CCN concentrations under different orographic scalings and with SIP disabled as well. Finally, Chapter **6** presents the results with activated SIP processes and evaluates how SIP modifies the interaction between orographic scaling and CCN concentration. A brief schematic of how results

are discussed is shown in Figure **1.1**. The thesis concludes with a summary of the main results and an outlook for future research in Chapter **7**.

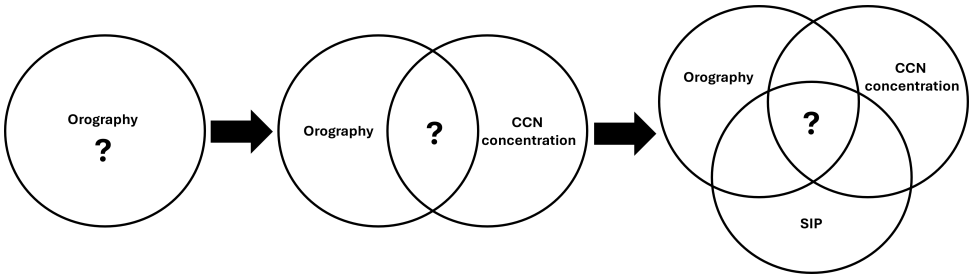

Figure 1.1: Schematic of the approach adopted for the discussion of results. The question mark (**?**) represents the parameters that are affected because of one element or interaction of different elements.

2 Theoretical Background

This chapter establishes the fundamental meteorological principles governing moist orographic convection, aerosol-cloud interactions, and secondary ice production. First, the focus is on introducing the thermodynamic principles and convective measures necessary to understand moist orographic convection. Subsequently, moist orographic convection itself is discussed, explaining the physical mechanisms crucial for understanding how terrain disrupts airflow and induces upward motion, leading to cloud formation. This is followed by an introduction to aerosol-cloud interactions and cloud microphysics. Finally, the chapter elaborates on the mechanisms of secondary ice production.

2.1 Basic thermodynamic principles

2.1.1 Potential and equivalent potential temperature

The concept of potential temperature, θ, is crucial for understanding atmospheric stability. It represents the temperature a parcel of air would attain if lifted (expansion) or lowered (compression) adiabatically to a standard reference pressure, typically 1000 hPa (Markowski and Richardson, 2010). It can be written as:

$$\theta = T\left(\frac{p_0}{p}\right)^{\kappa}, \qquad \kappa = \frac{R_d}{c_p}, \tag{2.1}$$

p_0 is the the reference pressure which is usually chosen as 1000 hPa.

However, the previous assumption of a dry adiabatic process is not applicable in moist atmospheric conditions where latent heat release from condensation significantly influences temperature changes (Holton, 2013). Therefore, the equivalent potential temperature, θ_e is introduced, which accounts for the latent heat released during condensation, providing a more comprehensive measure of atmospheric stability in moist environments (Trapp, 2013). According to Bolton (1980), it can be written as:

$$\theta_e = T\left(\frac{1000}{p}\right)^{0.2854\,(1-0.00028\,r)} \exp\left[\left(\frac{3.376}{T_{\mathrm{LCL}}} - 0.00254\,r\right)(1+0.00081\,r)\right], \tag{2.2}$$

where p is the pressure (in hPa), r is the mixing ratio (in $\mathrm{g\,kg^{-1}}$), and T_{LCL} is the temperature at the lifting condensation level (in K). The concept of LCL will be introduced in Section 2.1.3.

2.1.2 Static stability

Static stability considers the temperature of a displaced parcel relative to the environmental temperature surrounding the parcel. By comparing the parcel lapse rate to the environmental lapse rate, six different stability states can be defined (Bryan and Fritsch, 2000; Trapp, 2013):

Table 2.1: Stability regimes based on comparison of parcel and environmental lapse rates.

Condition	**Stability regime**
$\Gamma_m > \gamma$	Absolutely stable
$\Gamma_m = \gamma_s$	Saturated neutral
$\Gamma_d > \gamma > \Gamma_m$	Conditionally unstable
$\Gamma_m < \gamma_s$	Saturated absolutely unstable
$\Gamma_d = \gamma$	Dry neutral
$\Gamma_d < \gamma$	Dry absolutely unstable

Here, γ and γ_s are the lapse rates of unsaturated and saturated environments, respectively. Γ_d is the dry adiabatic lapse rate, and Γ_m is the moist adiabatic lapse rate. It will be shown in the Section 2.2.1 that among these stability regimes, the conditionally unstable case plays a crucial role in orographically induced convection initiation, particularly over complex terrain (Kalthoff et al., 2010).

2.1.3 Convective measures

While conditional instability is a necessary precursor for convective initiation, it is not always sufficient, as an inhibiting layer often needs to be overcome (Houston and Niyogi, 2007). This necessitates a deeper understanding of various convective parameters, such as Convective available potential energy (CAPE), convective inhibition (CIN), lifting condensation level (LCL), level of free convection (LFC), that quantify the atmospheric potential for supporting deep moist convection. (Schultz et al., 2000).

LCL

The LCL represents the altitude at which a lifted air parcel, initially unsaturated, cools adiabatically to its dew point temperature, leading to condensation. This level marks the base of the convective cloud and is a crucial parameter for initializing convection in numerical models (Holton, 2013).

LFC

The LFC is defined as the height at which an ascending air parcel, having reached saturation at the LCL, becomes warmer than the surrounding environmental air, thereby achieving positive buoyancy

and enabling self-sustaining ascent (Trapp, 2013). This critical level signifies the onset of buoyant convection, allowing the parcel to rise without further external forcing.

CAPE

CAPE quantifies the integrated buoyant energy available to an air parcel from its level of free convection (LFC) to its equilibrium level (EL), representing the maximum potential kinetic energy a parcel can attain through buoyant acceleration (Trapp, 2013). It is computed as the vertical integral of buoyancy B from LFC to EL:

$$\mathrm{CAPE} = \int_{\mathrm{LFC}}^{\mathrm{EL}} B\,dz, \tag{2.3}$$

CIN

Even though larger CAPE values indicates a higher potential for deep convection, there is no guarantee that convection will always initiate with those higher values. This is primarily due to the presence of a convective inhibition layer, which acts as a cap, requiring a certain amount of energy to be overcome before convection can be realized. It is computed similarly to CAPE, but integrating the negative buoyant energy from the parcel's initial level to the LFC (Trapp, 2013):

$$\mathrm{CIN} = \int_{\mathrm{sfc}}^{\mathrm{LFC}} B\,dz, \tag{2.4}$$

where sfc denotes the surface, LFC the level of free convection, and B is the parcel buoyancy.

Generally, low values are preferred for the realization of CAPE as large CIN values can suppress convection even in environments with substantial CAPE. However, if the lifting is sufficiently strong to locally overcome convective inhibition, deep convection can still initiate, particularly when strong localized forcing mechanisms, such as orographic lifting provide sufficient upward vertical velocity to overcome the energetic barrier (Metzger et al., 2014). This is assessed by parameter such as:

$$w_{\mathrm{diff}} = w_{\mathrm{max}} - w_{\mathrm{CIN}}, \tag{2.5}$$

where a positive value indicates that CAPE can be released (Barthlott and Kirshbaum, 2013). Here, $w_{\mathrm{CIN}} = \sqrt{2\,\mathrm{CIN}}$ is the vertical velocity a parcel must exceed in the boundary layer to overcome the convective inhibition and $w_{\mathrm{max}} = \sqrt{2\,\mathrm{CAPE}}$ is the maximum vertical velocity in the updraft.

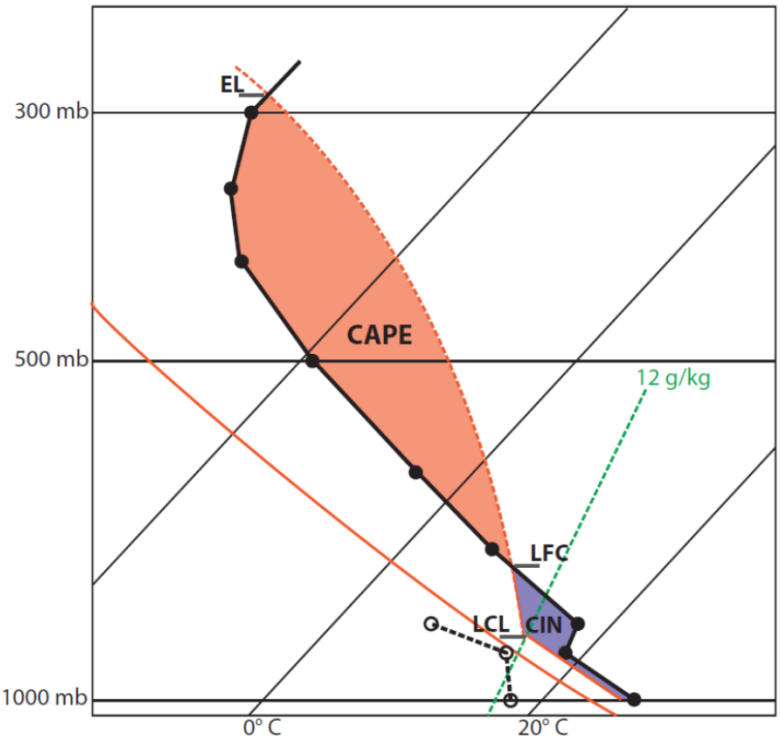

Figure 2.1: Skew-T log-*p* thermodynamic diagram with a representative sounding (black line). The shaded blue region between the surface and the LFC indicates convective inhibition (CIN), while the shaded orange region between the LFC and the EL corresponds to convective available potential energy (CAPE). From Trapp (2013)

All these convective parameters can be visualized through the skew-T log-*p* thermodynamic diagram (Figure **2.1**). It is visible that CAPE increases if cold air is advected into higher layers and warmer air is present in lower layers, which in turn reduces CIN and lowers the LFC.

2.2 Moist orographic convection: Physical mechanisms

Orographic precipitation events can be classified as either stratiform or convective, depending upon the static stability and structure of the cloudy regions (Kirshbaum and Durran, 2004). The necessary conditions and the physical mechanisms governing moist orographic convection (stratiform and convective) are detailed below.

2.2.1 Moist static instability

A moist-unstable atmosphere is characterized by a state where an air parcel, once lifted to saturation, continues to ascend due to positive buoyancy. This is often indicated by a moist adiabatic lapse rate that is steeper than the environmental lapse rate (Bryan and Fritsch, 2000). When sufficiently moist lower-level air is lifted over terrain, the forced ascent can cause an entire layer of the atmosphere to saturate (Kirshbaum and Durran, 2004). In this type of orographic cloud, convective or stratiform

cloud type can be predicted by checking the potential instability in the upstream atmospheric profile (Banta, 1990; Kirshbaum et al., 2018)

Using θ_e to diagnose moist stability

Equivalent potential temperature (θ_e) is a conserved thermodynamic variable during moist adiabatic processes, making it a robust diagnostic for assessing the potential for moist convection (Trapp, 2013). A decrease of equivalent potential temperature with height ($\frac{\partial \theta_e}{\partial z} < 0$) signifies a potentially unstable situation, indicating that if a layer is lifted to saturation, parcels from the bottom of the layer will become warmer than those from the top, leading to convective overturning (Kirshbaum and Durran, 2004).

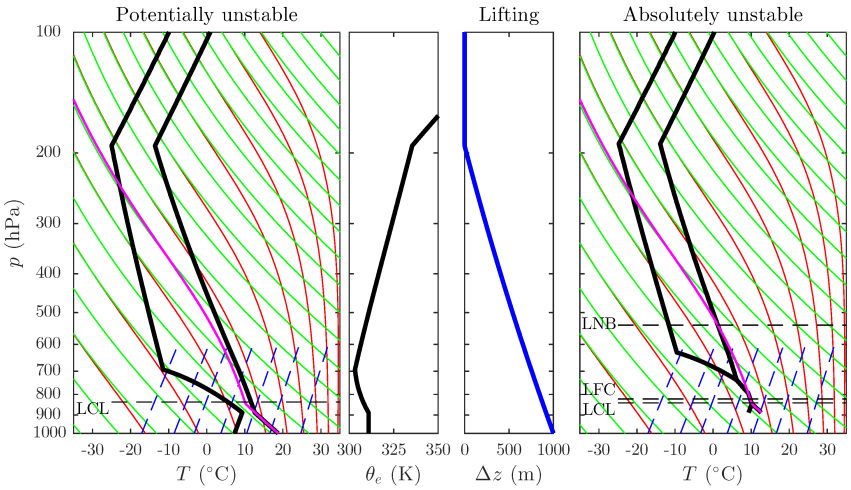

Figure 2.2: Left panels: showing environments that are initially absolutely stable and potentially unstable. Right panels: vertical lifting by $\Delta z(p)$ destabilizes the ∼800–700 hPa layer, making it absolutely unstable. From Kirshbaum et al. (2018)

The layers which exhibit conditional instability, forced lifting through orography can facilitate realizing the instability, leading to vigorous convective activity (Barthlott and Kirshbaum, 2013; Kirshbaum et al., 2018). Conditional and potential instability often coexist. However, its not always necessary. It can be seen from Figure **2.2** that shows an example of a sounding that is initially potentially, but not conditionally unstable (left two panels). However, when lifted upward, part of the layers saturates and become unstable. This distinction is crucial for understanding how orographic lifting can prime the atmosphere for convection, even when initial conditions might not appear conducive.

2.2.2 Low-level convergence

Low-level convergence plays a pivotal role in initiating and sustaining orographic convection. Boundary-layer dynamics, including the supply of moist, unstable air to the updraft region, help maintain a favorable environment for deep convective development (Demko et al., 2009). However, the occurrence of low-level convergence is a complex interaction of mountain airflow dynamics for

mechanically and thermally forced flows, upstream wind velocity and wind direction (Kirshbaum et al., 2018; Metzger et al., 2014).

Mechanically forced flows

When thermal forcing is absent, strong upstream wind velocity approaching the terrain either ascends or detours around it. According to Smith (1989), for a stable stratified flow, this response is determined by two key parameters:

Non-dimensional mountain height $(M) = Nh_m/U$

where N is the Brunt–Väisälä frequency, h_m is the mountain height, and U is the upstream wind speed; and

Terrain aspect ratio $(r) = a_y/a_x$, where a_y and a_x are the characteristic lengths of the mountain in the along-flow and cross-flow directions, respectively. The schematics of these parameters are shown in Figure **2.3**.

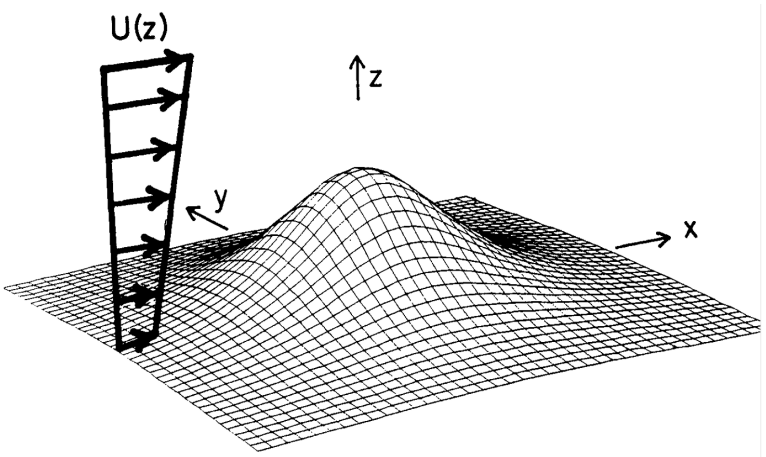

Figure 2.3: Schematic of an airflow approaching a mountain. a_x and a_y are the lengths in the x and y directions, respectively. $U(z)$ is the shear of the upstream wind in the z-direction. From Smith (1989)

If $M > 1$ and $r \gtrsim 1$, then the flow is "blocked" and diverted around the obstacle (Figure **2.4b**) , generating enhanced convergence zones either on the upstream side where the flow splits, or on the downstream side where the flow rejoins. Conversely, for flow with $M < 1$ and $r \ll 1$, the flow is "unblocked" and air predominantly flows over the mountain (Figure **2.4a**) and convergence occurs over the windward slopes. Under stable stratification, mechanically generated mountain waves can propagate vertically and extend terrain-induced motions through a large depth of the troposphere, yielding deep, layered precipitating clouds.

In conditionally unstable environments with nonzero CIN, in an unblocked flow (Figure **2.5a**), it is required that some streamlines are lifted sufficiently to overcome convective inhibition and initiate buoyant ascent (Lin et al., 2001). For a blocked flow (Figure **2.5b**) where $M \gtrsim 1$, if there is an upstream blocking, the convergence zone is established on the upstream side, which can locally

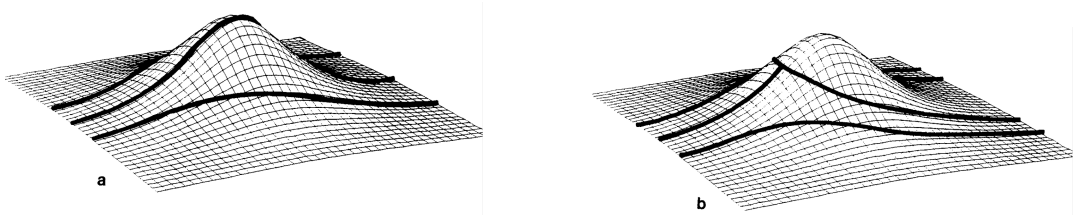

(a) Non-split flow across a mountain.

(b) Split flow across a mountain.

Figure 2.4: Possible geometries of flows across a mountain in a stably stratified flow. Split flow is characterized by the existence of a stagnation point at which streamlines can divide. From Smith (1989)

reduce or eliminate convective inhibition, leading to convection initiation there (Barthlott and Kirshbaum, 2013). A well-observed case of such a phenomenon was observed over northeastern Italy during the HyMeX campaign, where the blocking of a low-level jet by the Alps led to significant orographic convection initiation (Davolio et al., 2015). For lee-side convergence (Figure **2.5c**), the approaching flow rejoining on the lee side can create convergence zones that are favorable for convective initiation.

Thermally forced flows

In thermally forced flows, diabatic daytime surface heating or nighttime cooling over mountainous terrain gives rise to thermally direct diurnal cycle circulations (Zardi and Whiteman, 2012). This mechanism is primarily associated with the deep convective clouds and precipitation. It is common to observe these flows in island environments such as Corsica which receive strong solar insolation (Barthlott and Kirshbaum, 2013). Thats why understanding thermally forced flows are crucial in the context of this thesis.

Daytime flows: During the day, solar radiation heats the mountain slopes, leading to the formation of anabatic winds that are buoyant and ascend the terrain (Nugent et al., 2014). These flows are also generated by the pressure gradient forces induced by thermal perturbations over the heated terrain (Zardi and Whiteman, 2012) (Figure **2.5d**). The upward ascent, converging near or downwind of the mountain crest, provides a strong updraft that penetrates into the free troposphere, thereby promoting moist convection initiation and growth (Kirshbaum, 2010) .

Nighttime flows: Conversely, nighttime radiative cooling of the slopes induces katabatic winds due to reversal of the buoyancy and pressure gradient forces (Figure **2.5e**) (Zardi and Whiteman, 2012) . This can initiate the convection when the downslope flow converges in the valley bottom or mountain base.

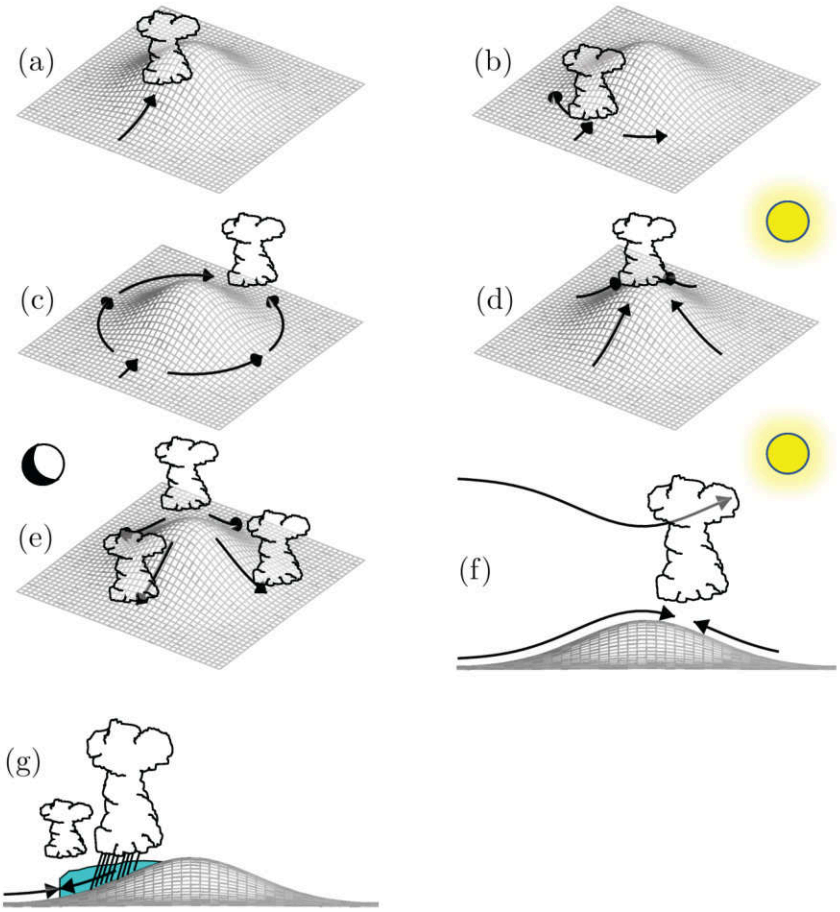

Figure 2.5: Schematic of convergence triggering and convection initation mechanisms. **(a)** mechanical unblocked, **(b)** mechanical upstream blocking, **(c)** mechanical split and lee-side convergence, **(d)** thermal anabatic flow, **(e)** thermal katabatic flow, **(f)*** combined mechanical and thermal flow with mountain-wave ascent aloft (not discussed here), **(g)*** quasi-stationary cold pool beneath precipitating convection (not discussed here). From Kirshbaum et al. (2018)

2.2.3 Preconditioning

For deep moist convection to occur, either by mechanically forced or thermally driven ascent, the local environment must be sufficiently preconditioned, typically characterized by low CIN and high CAPE (Kirshbaum et al., 2018). However, the mechanisms to achieve this preconditioning is different for both mechanical and thermally forced flows.

In a **mechanically forced flow**, preconditioning is related to the static destablization and humidification of the approaching flow. This includes reducing atmospheric boundary layer (ABL) CIN (de la Torre et al., 2004; Kirshbaum, 2016) and increasing the CAPE through boundary-layer heating and moisture accumulation (Demko and Geerts, 2010). Thus, a delicate balance between sensible and latent heat fluxes is essential for optimal preconditioning, facilitating both the erosion of convective inhibition and the accumulation of CAPE. In a **thermally forced flow**, nighttime katabatic winds drain radiatively cooled air into valleys, restricting the formation of inversion layers over the peaks. Consequently, CIN is lowest in the morning and early afternoon, as observed during the COPS IOP8b campaign, as observed during the COPS IOP8b campaign (Behrendt et al., 2011). Air is

much drier over the mountain ridges than in the valleys, implying that convection initiated over ridges would require substantial moistening from below to become deep and sustained (Adler and Kalthoff, 2014). This uplift of humid air effectively increases the CAPE by advecting moisture, facilitating deeper convection development.

2.3 Aerosols

Atmospheric aerosols are defined as fine solid particles or liquid droplets suspended in the atmosphere with diameters typically ranging from a few nanometers to tens of micrometers (Seinfeld and Pandis, 2016). These particles originate from both natural and anthropogenic sources (Arfin et al., 2023). The natural aerosols include volcanic ash, sea salt, dust, and biogenic emissions, while anthropogenic aerosols are primarily composed of sulfates, nitrates, soot, and organic carbon from industrial activities, biomass burning, and vehicular emissions. The antropogenic aerosols are also categorized as secondary aerosols as they are formed through chemical reactions of gaseous precursors (Fan et al., 2025). Whereas natural aerosols are directly emitted into the atmosphere and are categorized as primary aerosols. Aerosols can act as cloud condensation nuclei (CCN) or ice nucleating particles (INP), depending on their hygroscopicity and chemical properties (Kanji et al., 2017; Seinfeld and Pandis, 2016).

CCN are hydrophilic aerosols. They serve as sites for cloud droplet formation once supersaturation with respect to liquid water is reached (Hande et al., 2016). This allows droplet formation at supersaturations much lower than those needed for homogeneous nucleation (Altaratz et al., 2014). The detailed description of CCN activation is given in Section **2.4.1**. Insoluble aerosols that act as ice-nucleating particles (INPs) provide surfaces for heterogeneous ice formation at temperatures above the homogeneous freezing limit of about $-38°$C (Korolev et al., 2017). This heterogeneous ice nucleation processes involves ice formation via deposition nucleation where ice forms directly from water vapor, immersion freezing where a supercooled liquid droplet containing an INP freezes, or contact freezing where an INP collides with a supercooled droplet (Hoose and Möhler, 2012). In this thesis, only the effect of varying CCN concentrations is considered.

2.4 Cloud microphysics

The essential requirements for cloud formation are sufficient moisture, cooling mechansim to reach supersaturation, and aerosol particles (Lamb and Verlinde, 2011). Supersaturation occurs when the environmental vapour pressure e reaches the saturation vapour pressure $e_s(T)$. $e_s(T)$ is given by the Clausius–Clapeyron relation (Clapeyron, 1834; Clausius, 1850):

$$e_s(T) = e_0 \exp\left[\frac{L_v}{R_v}\left(\frac{1}{T_0} - \frac{1}{T}\right)\right], \tag{2.6}$$

where L_v is the latent heat of vaporisation, R_v the gas constant for water vapour, and T_0 and $e_0(T_0)$ denote the temperature and vapour pressure at the triple point of water.

Clouds consist of liquid and solid (cloud-ice, snow, graupel and hail) hydrometeors. Cloud microphysical processes describe how these particles grow, interact and change size or phase. They are often grouped into warm-rain processes that occur in liquid-phase clouds at temperatures above 0°C and cold-rain processes that involve ice hydrometeors at temperatures below 0°C. Clouds between about 0°C and −38°C are mixed-phase clouds, where supercooled liquid droplets and ice crystals coexist (Korolev et al., 2017). Clouds below −38°C are ice only.

2.4.1 Warm-rain processes

CCN activation

Hydrophilic aerosol particles absorb water vapour and grow into cloud droplets once the ambient relative humidity exceeds a critical supersaturation (Lamb and Verlinde, 2011). Supersaturation occurs when the partial pressure of water vapour exceeds the saturation vapour pressure. Newly formed droplets are in unstable equilibrium and must reach a critical radius r_c to grow further. This CCN activation is described by Köhler theory. It quantitatively links droplet size, curvature and solute concentration and defines the Köhler curve (Lamb and Verlinde, 2011). The curve gives the vapour pressure over a solution droplet as a function of radius and includes the Kelvin effect (from curvature) and the Raoult effect (from solute). The full equation for the saturation vapour pressure, S is written as:

$$S \approx 1 + \frac{A}{r} - \frac{B}{r^3} \tag{2.7}$$

The term A/r is the Kelvin effect and describes the increase in saturation vapor pressure over a curved surface. This necessitates higher supersaturations for smaller droplets. The term A depends weakly on the temperature. The term B/r^3 represents the Raoult effect and it accounts for the reduction in saturation vapor pressure due to dissolved solutes, with B depending on the solute and its chemical properties. The balance between Kelvin and Raoult effects defines the critical supersaturation and critical radius r_c (see Figure **2.6**). Droplets that reach r_c become activated , while smaller droplets evaporate or remain as unactivated haze particles.

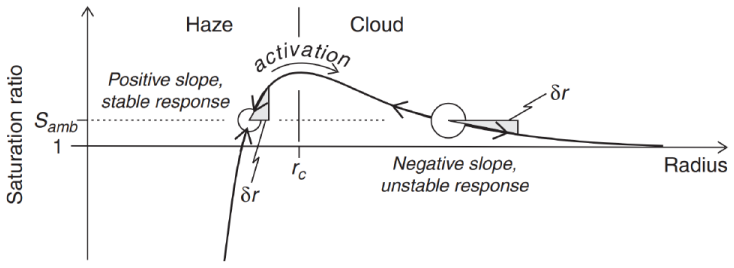

Figure 2.6: Schematic of the Köhler equation defined in Equation **2.7**. From Lamb and Verlinde (2011)

Condensational growth and rain formation

Once activated, cloud droplets grow in radius (r_d) mainly by condensation, as water vapour deposits on their surfaces (Lamb and Verlinde, 2011). The mass growth rate is

$$\frac{\mathrm{d}m_d}{\mathrm{d}t} = 4\pi r_d \rho_w G s, \tag{2.8}$$

where G_s is the effective diffusivity, ρ_w the density of water, and m_d the droplet mass. This implies that smaller droplets grow faster by condensation ($\mathrm{d}r_d/\mathrm{d}t \propto r_d^{-1}$) and $r_d(t) \sim \sqrt{t}$. Condensational growth slows once the radius reaches about $20\,\mu$m, whereas raindrops larger than $50\,\mu$m are observed (Seifert and Beheng, 2006). Their further growth is explained by collision–coalescence (collection) process, in which larger, faster-falling droplets collect smaller droplets along their path (Lamb and Verlinde, 2011). The efficiency of this process depends upon the size of both the large collector droplet and the smaller droplets being collected. The maximum efficiency achievable for collision-coalescence ranges between 50–60% (Lamb and Verlinde, 2011).

In the ICON model (described later), the term **autoconversion** defines the rain formation with the collision–coalescence process. Subsequent rapid growth of raindrops is represented by **accretion**, where larger raindrops collect smaller cloud droplets and other raindrops.

2.4.2 Cold-rain processes

Homogeneous and heterogeneous nucleation (primary ice formation)

In the absence of an efficient freezing mechanism, liquid water can exist in a supercooled state down to approximately $-38°$C. According to the classical nucleation theory (CNT) mentioned in Ickes et al. (2014), freezing depends upon interfacial tension between ice and water, which determines the energetic barrier of the nucleation process. However, at temperatures below $-38°$C, supercooled water and solution droplets spontaneously freeze through **homogeneous nucleation** (Hoose and Möhler, 2012).

However, at temperatures above $-38°$C, ice formation typically occurs **heterogeneously**. This is facilitated by the surfaces of INPs (Vali et al., 2015). The pathways through which these particles initiate freezing include deposition nucleation, condensation, immersion, and contact freezing (Hoose and Möhler, 2012). They are also shown in Figure **2.7**. Deposition nucleation occurs when water vapor directly deposits onto an INP, forming ice without an intermediate liquid phase. Condensation freezing happens when the water vapor first condenses into a supercooled liquid droplet on the INP and subsequently freezes (Nicosia et al., 2017). Immersion freezing occurs when an INP is submerged within a supercooled liquid droplet, initiating freezing from within the droplet. Finally, contact freezing involves an INP colliding with a supercooled droplet and initiating freezing at the point of contact.

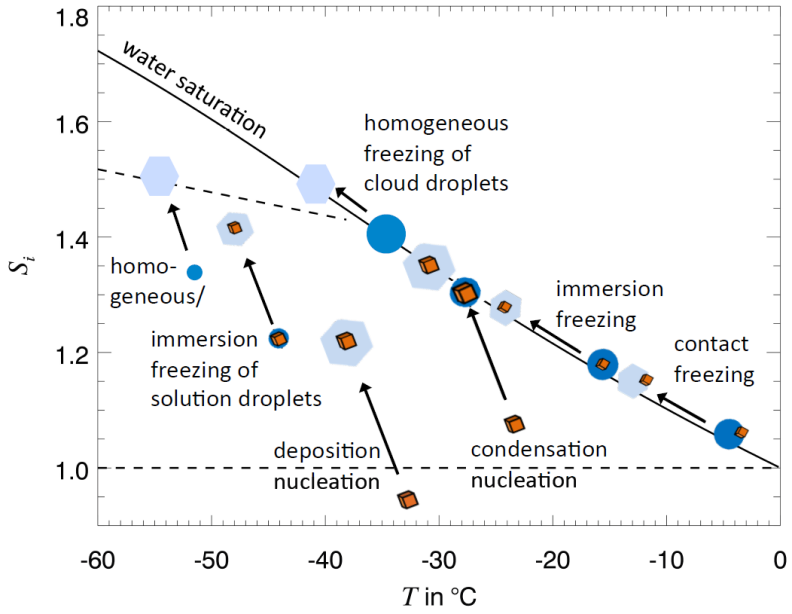

Figure 2.7: Variation of different nucleation pathways with temperature (x-axis) and supersaturation (y-axis). From Hoose and Möhler (2012)

Growth by riming and aggregation

Riming is the freezing of supercooled liquid droplets onto the surface of an ice hydrometeor. It is characteristic of mixed-phase clouds (Levizzani and Kidd, 2025). Riming depends on collision efficiency, droplet size, and the supercooled liquid water content (Lamb and Verlinde, 2011; Wang and Ji, 2000). It increases the mass of rimed ice hydrometeors, while their number concentration stays unchanged. In the current model setup, riming is parameterized following Seifert and Beheng (2006). It includes riming of ice, snow, graupel, and hail by supercooled liquid water. The parameterization scheme itself is explained in the later section. Different aerosol concentrations can modify riming by shifting droplet size distributions and thus collision efficiencies (Cui et al., 2011).

Aggregation involves the collision of ice crystals and and subsequently sticking together. The most common aggregate forms are snowflakes, which are combinations of various ice crystal habits. It is most effective at temperatures near 0°C (Lamb and Verlinde, 2011). However, aggregation efficiency also depends on the ice crystal habit involved and the relative fall speed. The aggregation of ice hydrometeors increases the mass concentration of the particles and decreases their number concentration. It is also parameterized by Seifert and Beheng (2006) and involves same particle type aggregation mechanisms (ice-ice to ice, snow-snow to snow, graupel-graupel to graupel and hail-hail to hail) and different particle type aggregation (ice-snow to snow, ice-graupel to graupel, snow-graupel to graupel and snow-hail to hail).

Secondary ice production (SIP) processes

Observed ice crystal number concentrations in mixed-phase clouds often exceed values predicted from INP concentrations alone (Field et al., 2017; Georgakaki et al., 2022; Lauber et al., 2021). This is attributed to another critical mechanism of secondary ice production (SIP) in mixed-phase clouds.

It significantly augments the ice crystal number concentration within certain temperature regimes. It is extensively researched in the laboratory (Korolev et al., 2020). However, it is not well represented in many numerical models (Han et al., 2024) and many recent studies have shown the impact of including SIP processes in the model on cloud microphysics and precipitation (Costa-Surós et al., 2025; Grzegorczyk et al., 2025; Sotiropoulou et al., 2021a).

Out of the six mechanisms mentioned in Korolev et al. (2020), three are typically considered most significant: rime splintering, also known as the Hallett-Mossop process (Hallett and Mossop, 1974), droplet shattering during freezing (Brownscombe and Thorndike, 1968; Lauber et al., 2018; Mason and Maybank, 1960), and ice-ice collisional breakup (Takahashi et al., 1995; Vardiman, 1978). The remaining mechanisms (ice crystal fragmentation during sublimation, activation of INPs in transient supersaturation, and thermal shock ice fragmentation) are not discussed in this thesis.

Rime splintering occurs when supercooled droplets rime onto larger frozen particles and eject small ice splinters. The first experimental evidence was provided by Hallett and Mossop (1974). It is active between -3 and -8°C when supercooled droplets are larger than 25μm or smaller than 13μm (Field et al., 2017). **Droplet shattering** occurs when supercooled droplets freeze rapidly. The freezing droplet expands and releases ice fragments. It is most effective for droplets larger than 50μm and at -10 to -15°C (Lauber et al., 2018). The **collision breakup** refers to the fracturing of frozen hydrometeors upon collision. This process is expected to occur in all types of clouds with ice formation. The fragments generated depends upon the temperature (Takahashi et al., 1995), fraction of riming (Vardiman, 1978) and collision kinetic energy (Phillips et al., 2017). Takahashi et al. (1995) analyzed the the collision breakup by setting up the controlled experiment of two graupel particles and found that most number of fragments are generated around $-15\,$°C.

2.5 The ICON model

The Icosahedral Non-hydrostatic (ICON) model is an operational forecast model developed by the German Weather Service (DWD), the Max-Planck Institute for Meteorology (MPI-M), the German Climate Computing Centre (DKRZ) and KIT (Zängl et al., 2014). It has been in operational use since 2015. ICON is non-hydrostatic and can therefore simulate convection-permitting scales without the hydrostatic approximation. The hydrostatic approximation assumes a balance between the vertical pressure gradient and gravity and is not valid for rapidly developing deep convection. By explicitly resolving vertical motion, ICON supports high-resolution simulations at grid spacings finer than about 2 km.

The horizontal grid of ICON is derived from a refined spherical icosahedron. An icosahedron projected onto the sphere yields 20 equilateral spherical triangles, which are recursively subdivided to reach the desired resolution. An ICON grid is denoted RnBk, where n is the number of equal sections of the original icosahedral edges and k the number of subsequent bisections (Reinert et al., 2024). The number of cells n_{cells} is

$$n_{\text{cells}} = 20\,n^2\,4^k. \tag{2.9}$$

The grid resolution is determined by the number of cells. More cells imply finer resolution and a smaller distance between grid points. This is quantified by the effective grid spacing $\overline{\Delta x}$, defined from the mean triangle area of the grid (Reinert et al., 2024):

$$\overline{\Delta x} = \frac{R_{\text{earth}}}{n2^k}\sqrt{\frac{\pi}{5}} \approx \frac{5050}{n2^k}\ [\text{km}], \tag{2.10}$$

where R_{earth} is the Earth's radius.

The model utilizes an unstructured triangular grid with Arakawa C-type staggering, enabling variables to be precisely located at different points within the same grid cell. ICON employs the Smooth Level Vertical Coordinate (SLEVE) system for its vertical coordinates, allowing for accurate representation of terrain-following layers near the surface while transitioning to constant height levels higher in the atmosphere (Leuenberger et al., 2010). This hybrid approach ensures high accuracy in simulating boundary layer processes over complex topography while maintaining computational efficiency at higher altitudes.

The ICON model has two principal components - **the dynamical core** and the **parameterization schemes (physics)**. The **dynamical core** is responsible for solving the fundamental atmospheric equations governing fluid motion. The equation system of the ICON model is based upon the prognostic variables suggested by Gaßmann and Herzog (2008). The coupled primitive equations are: horizontal momentum equation (edge-normal component), vertical momentum equation, thermodynamic equation, mass continuity equation, tracer continuity equations and equation of state. The explanations for the full set of equations are outlined in Gaßmann and Herzog (2008) and Zängl et al. (2014). The ICON dynamical core solves these coupled equations on an unstructured icosahedral triangular grid using a split-explicit time-stepping scheme that separates fast acoustic modes from slower advective processes (Reinert et al., 2024). The resulting numerical solution provides the 3D atmospheric state: velocity, temperature, pressure, and density at each model level.

The **parameterizations** address sub-grid scale physical processes that cannot be explicitly resolved by the dynamical core due to computational constraints. Many atmospheric processes occur at scales smaller than the typical grid spacing of numerical weather prediction and climate models. Thus, these parameterizations are crucial for representing the collective effects of these unresolved processes. These include processes such as cloud microphysics, turbulence, radiation, and convection. The important parameterization relevant for this thesis are thoroughly discussed in the Section **3.4**.

3 Data and Methods

This chapter introduces the methods used in this thesis: numerical modelling approach (ICON model setup), design of the sensitivity experiments, parameterization implemented and statistical measures.

3.1 Model setup description

The simulations of the present thesis are conducted with the version 2024.10 of the ICON model. The convection-permitting Limited Area Model (LAM) configuration is used in this thesis. The simulation domains of this thesis are two contrasting island environments of Corsica and Iceland (shown in the sub-figures on the right side of Figures **3.1** and **3.2**). The R19B08 grid is used for the current simulations. This corresponds to a horizontal resolution of approximately 1 km. It covers the entire domain of Corsica and Sardinia as well as some parts of Italy as well (left sub-figure of Figure **3.1**). However, for the Mediterranean simulations, the focus of analysis is solely on the Corsica domain. For the sub-polar Iceland simulations, the grid covers the entire island and its immediate surrounding waters (left sub-figure of Figure **3.2**). Also, the Corsica domain has about 311 693 grid points and the Iceland domain has approximately 485 196 grid points. Both domains utilize height-based terrain-following 100 vertical levels. For all the simulation days, initial and boundary conditions (IBCs) are derived from ICON-EU and remapped to the target ICON-LAM R19B08 grid using the DWD ICON remapping tools (iconremap). Afterwards, the ICON model run is initiated to produce the model output files that are subsequently post-processed for further analysis. All simulations are initialized at 00:00 UTC with an integration time of 24 h.

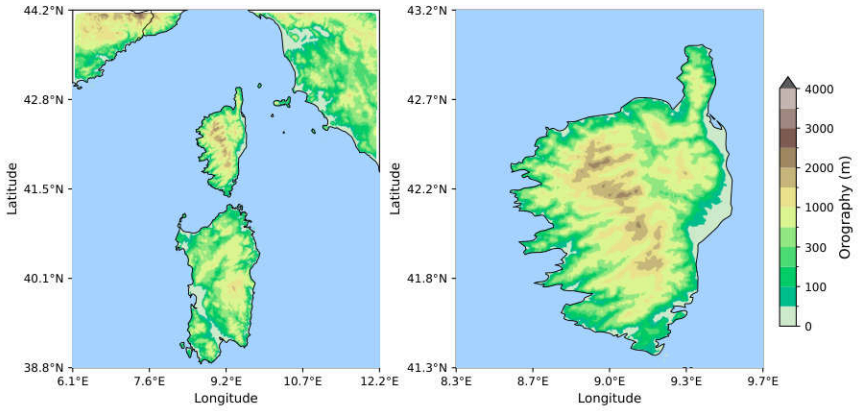

Figure 3.1: **(left)**:ICON model topography of the full Mediterranean domain (Corsica, Sardinia and some parts of Italy), **(right)**: topography of Corsica only.

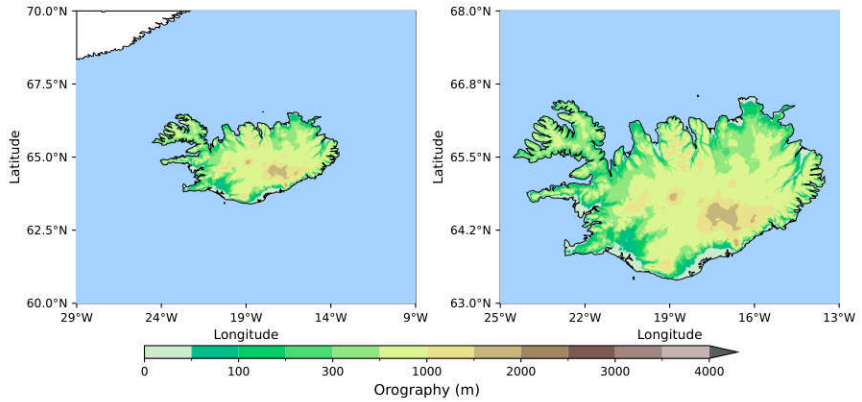

Figure 3.2: **(left)**:ICON model topography of the full sub-polar domain (island of Iceland and surrounding waters), **(right)**: topography of Iceland only.

Orography scaling

In ICON, orography is represented in the external parameter file. The external parameter file describes the properties of the earth's surface which can be assumed static during the simulation period (24 h) (Reinert et al., 2024). The external parameter file uses reference (or original) orography derived from the ASTER global digital elevation model. For this thesis, to investigate orographic effects on various processes, the reference orography is further scaled to maximum target heights of 1, 2, 3, and 4 km, as well set to completely flat. However, for the flat case, the scale is set to a constant 10 m wherever the original maximum height exceeds 10 m, while values below 10 m are left unchanged. For the rest of the maximum target heights, the orography is scaled according to the relation:

$$H_{\text{scaled}} = H_{\text{original}} \times \frac{H_{\text{target}}}{H_{\text{max}}}. \tag{3.1}$$

where H_{target} is the target maximum elevation and H_{max} is the maximum elevation in the reference orography. The orography scaling of the both islands are shown in the Figure **3.3**. For the Corsica domain, the orography becomes increasingly complex along the north–south mountain spine, especially in the central and northern part of the island, as the scaling height is raised from flat to 4 km. For the Iceland domain, the complexity concentrates along the central and southeastern regions. The statistical information of the orography scaling is shown in the Table **3.1**. The domain-mean elevation of Iceland (2000 m) is lower than Corsica (2396 m). Each scaled orography of Corsica is characterized by a systematically higher standard deviation than Iceland.

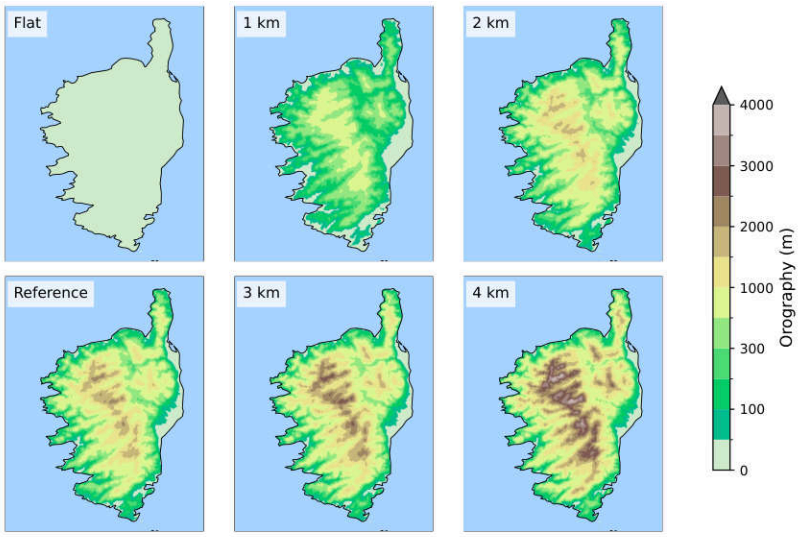

(a)

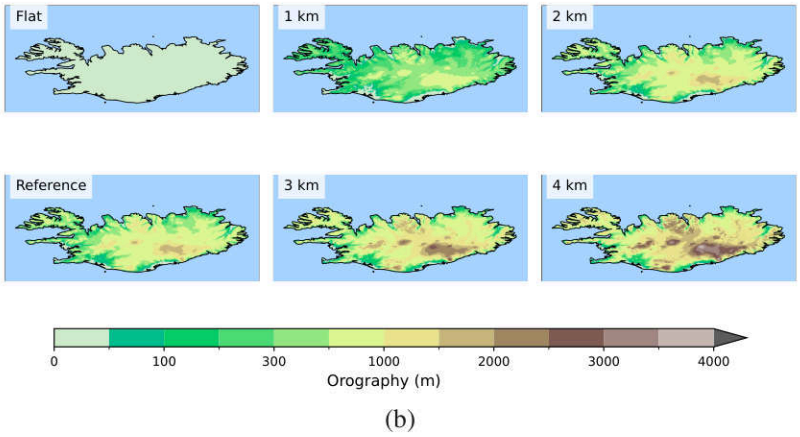

(b)

Figure 3.3: **(a)**: Spatial distribution of the orography scaling of the Corsica model domain, **(b)**: Similar to **(a)** for Iceland model domain.

Orography scale	$\overline{H}$ (m)		$H_{\max}$ (m)		σ (m)	
	Iceland	Corsica	Iceland	Corsica	Iceland	Corsica
Reference	499	540	2000	2396	376	487
Flat	9	9	10	10	1.4	1.5
1 km	249	226	1000	1000	188	203
2 km	499	451	2000	2000	376	407
3 km	748	676	3000	3000	564	610
4 km	997	901	4000	4000	752	814

Table 3.1: Domain-mean height $\overline{H}$, maximum height $H_{\max}$, and standard deviation σ of orography for Iceland and Corsica for different orography scaling cases.

CCN concentrations

To investigate aerosol-cloud interactions, the model employs a double-moment microphysics scheme by Seifert and Beheng (2006), which predicts both mass and number concentration for all hydrometeor categories. This enables the use of varying CCN concentrations assumptions. The detailed description of this scheme is provided separately in the Section **3.4.1**. In present thesis, four different CCN number concentrations are implemented. They are maritime (number concentration (N) = 100 cm^{-3}), intermediate (N= 500 cm^{-3}), continental (N = 1700 cm^{-3}), and continental polluted conditions (3200 cm^{-3}). For the analysis, they are labeled as CCN06 (maritime), CCN07 (intermediate), CCN08 (continental) and CCN09 (continental polluted). For some results, the maritime and intermediate CCN concentrations are aggregated to represent as "low CCN concentrations" and continental and continental polluted conditions are aggregated as "high CCN concentrations" to provide clear distinctions in the resulting microphysical and precipitation responses. The CCN information is summarized in Table **3.2**.

Label	Concentration	CCN Regime
CCN06	100 cm^{-3}	Maritime
CCN07	500 cm^{-3}	Intermediate
CCN08	1700 cm^{-3}	Continental
CCN09	3200 cm^{-3}	Continental Polluted

Table 3.2: Classification of cloud condensation nuclei (CCN) concentrations and their representation.

Secondary ice production mechanisms

To assess the impact of the SIP mechanisms described in Section **2.4.2**, model simulations are conducted with and without the inclusion of these mechanisms. In the present thesis, these scenarios are labeled as "**SIP-On**" and "**SIP-Off**" respectively. The **SIP-On** scenario represents activation of all SIP mechanisms (rime splintering, droplet shattering, and collision-breakup). **SIP-Off** refers to simulations where these mechanisms are deactivated. An overview of in which temperature range the SIPs are active is given in the Section **3.2** where simulations description is given. Also, the detailed description of the parameterization schemes for different SIP mechanisms is provided separately in the Section **3.4.2**. By default, the rime splintering process is always active in ICON with the double-moment microphysics scheme of Seifert and Beheng (2006). However, to completely disable all SIP mechanisms, the current operational version of ICON used in this thesis implements a modification which ensures that no SIP mechanism occurs in the "**SIP-Off**" scenario.

3.2 Simulations overview

In total, three real cases are investigated in this thesis. Two days (27 August 2024 and 04 August 2024) are dedicated to study deep convection over Corsica, and one day (07 May 2023)

is dedicated to analyzing shallow stratiform convection over Iceland. The selection criteria for choosing the days is discussed in the Section **3.3**.

Initially, the impact of orography on convective initiation and convection-related parameters is assessed by fixing the CCN concentration at intermediate conditions (CCN07) and keeping SIP off. Orography is then varied systematically from flat terrain to scaled heights of 1, 2, 3, and 4 km. Next, the role of varying CCN concentrations (CCN06–CCN09) is examined using only the 1 and 3 km scalings, which represent below and above the domain maximum orography for both islands. SIP mechanisms remain off in this step to isolate orography and aerosol–cloud interactions. Finally, SIP mechanisms are activated to assess how they modify the interactions between orography scaling and CCN concentrations. An overview of all numerical simulations is given in Table **3.3**.

Orography	**CCN concentrations**	**SIP**
Orography		
Flat 1 km 2 km Reference 3 km 4 km	CCN07	Off
Orography and CCN concentrations		
1 km	CCN06, CCN07, CCN08 and CCN09	Off
3 km	CCN06, CCN07, CCN08 and CCN09	
Orography, CCN concentrations and SIP		
1 km	CCN06, CCN07, CCN08 and CCN09	On
3 km	CCN06, CCN07, CCN08 and CCN09	

Table 3.3: Overview of simulation experiments combining orography scaling, CCN concentrations, and SIP activation.

3.3 Selection criteria for simulation days

For Corsica, the simulation days are selected based on the presence of deep convective clouds in satellite imagery (Figure **3.4**). On 27 August 2024, shallow clouds develop over the central and northwestern ridges during the early morning, and deep convection initiates over northwestern Corsica around 1100 UTC. By 1400 UTC, convection intensifies and propagates into the central and southern parts of the island, before dissipating around 1600–1700 UTC. Interestingly, convective clouds also develop over almost entire region of Italy, some parts of Sardinia and northern Africa. On 04 August 2024, deep convection similarly initiates in the late morning and intensifies through the afternoon, but with a different spatial distribution where the convective clouds are mainly concentrated over central and southeastern Corsica.

(a) 1100 UTC (b) 1400 UTC (c) 1600 UTC

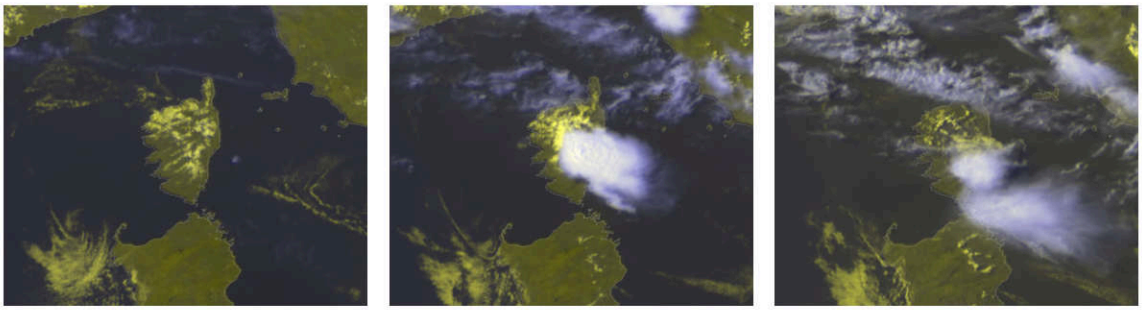

(d) 1100 UTC (e) 1400 UTC (f) 1600 UTC

Figure 3.4: Meteosat satellite pictures for Corsica from 1100 to 1600 UTC for: 27 August 2024 **(a-c)**, 04 August 2024 **(d-f)**. The EUMETSAT HRV clouds RGB color scheme is interpreted as follows: Bright white indicates high-altitude ice clouds. Bluish shades represent thin high-level clouds. Shades of yellow indicates fog, low and mid-level clouds or snow covered land (depending upon cloud-top temperature, cloud thickness and state of snow). Shades of grey with some bluish or yellowish tones depending upon the temperature or surface reflectivity represent snow-free land. Further detailed information regarding color schemes can be found here: https://user.eumetsat.int/resources/user-guides/hrv-clouds-rgb-quick-guide

For Iceland, local deep convection is rarely observed because net surface solar radiation is much lower than in the Mediterranean. Therefore, a shallow stratiform convective case that primarily depends on large-scale atmospheric forcing is selected. As shown in the Figure **3.5**, low- to mid-level cloud cover persists throughout the day. At 1100 UTC, most of the region is covered by stratocumulus/cumulus clouds with some mid-level clouds over central Iceland. There is a slight development of thin high-level clouds primarily in the northern parts and some in the central parts by 1400 UTC which persists till late afternoon (1600-1700 UTC). Also, for all the simulation days, the respective reference ICON runs are able to simulate the 24 h accumulated surface precipitation close to the observed 24 h accumulated precipitation.

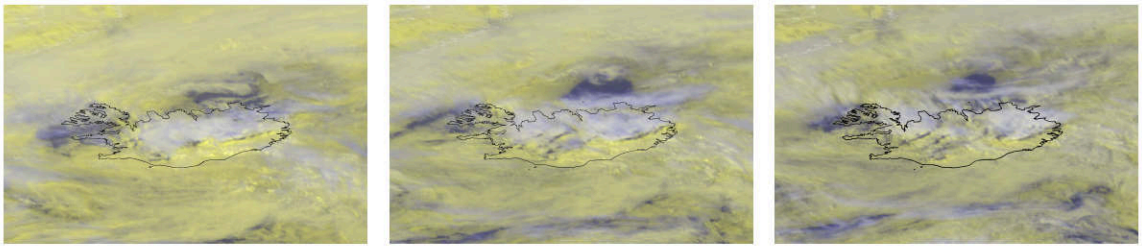

(a) 1100 UTC (b) 1400 UTC (c) 1600 UTC

Figure 3.5: Meteosat satellite pictures for Iceland from 1100 to 1600 UTC for: 07 May 2023. The color scheme reference is the same as described in the Figure **3.4**.

3.4 Parameterizations

Since cloud microphysics and SIP processes are central to the results of this thesis, an overview of their parameterization schemes is provided here. The rest of the important parameterizations are summarized in the Table **3.5**.

3.4.1 Microphysics

Microphysical schemes are commonly divided into bulk and bin schemes. Bulk schemes describe hydrometeor size distributions using semi-empirical particle size distributions (Rutledge and Hobbs, 1984). Whereas bin schemes explicitly solve microphysical equations for discretized size bins, requiring substantially higher computational resources (Khain et al., 2015; Onishi and Takahashi, 2012).

Bulk schemes are further classified into single-moment and double-moment approaches. Single-moment schemes predict only the hydrometeor mass mixing ratio, which is sufficient for representing the hydrological cycle (Reinert et al., 2024). Double-moment schemes additionally predict number concentration, enabling a more consistent diagnosis of particle size distributions from the mass and number moments (Reinert et al., 2024).

Here, the ICON model is set up with a double-moment bulk microphysics scheme by Seifert and Beheng (2006). The scheme predicts, for each hydrometeor category j, both the mass (q_j) and the number (n_j) concentrations. In the current configuration six hydrometeor classes are considered: cloud water, rain, cloud ice, snow, graupel and hail. Predicting both mass and number concentrations allows the scheme to more accurately represent aerosol–cloud interactions.

The scheme assumes that the particle mass distribution of each hydrometeor class j can be represented by a generalized gamma distribution in particle mass x,

$$f_j(x) = A_j x^{\nu_j} \exp\left(-\lambda_j x^{\mu_j}\right), \qquad x > 0, \tag{3.2}$$

where $f_j(x)\,\mathrm{d}x$ is the number concentration of particles with masses in $[x, x+\mathrm{d}x]$, ν_j and μ_j are hydrometeor-class specific fixed shape parameters, and A_j and λ_j are diagnosed from the prognostic mass and number of each species. The full gamma distribution equations and its individual components are explained further in Seifert and Beheng (2006).

The size distribution can also be represented as a function of diameter D. This is done by using the relation $x = \frac{\pi}{6}\rho D^3$ for spherical particles (Barthlott et al., 2022b; Khain et al., 2015). The diameter-space gamma distribution can then be defined as

$$f_j(D) = N'_{0,j} D^{\nu'_j} \exp\left(-\lambda'_j D^{\mu'_j}\right), \tag{3.3}$$

with $N_0' = 3N_0 \left(\frac{\pi}{6\rho}\right)^{\nu+1}$, $\nu' = 3\nu + 2$, $\lambda' = \lambda \left(\frac{\pi}{6\rho}\right)^{\mu}$, and $\mu' = 3\mu$, where N_0 is an intercept parameter and ρ the bulk density.

Generally, the class-specific mass–diameter relation is parameterized by a power law $D_j(x) = a_j x^{b_j}$, where a_j and b_j are the characteristic parameters of the respective hydrometeors.

The numerical integration of the microphysical processes follows a sequential approach. To ensure thermodynamic equilibrium, a saturation adjustment technique is applied. This procedure is executed both prior to and after the microphysical process calculations (Wallentin, 2025). This iterative adjustment ensures that any supersaturation or subsaturation remaining after the end of the microphysical call is resolved into condensation or evaporation. This provides an adjusted temperature and water vapor field for the subsequent dynamics call.

3.4.2 Secondary ice production

In this section, only an overview of the SIP parameterizations implemented in the model are presented. For more details with full set of equations, see Han et al. (2024)

Rime splintering

The ICON model by default parameterizes the rime splintering mechanism with the two-moment microphysics scheme of Seifert and Beheng (2006). This rate of change in the ice crystal number concentration (N_{ice}) depends upon rimed mixing ratio q_{rime}, temperature-dependent weighting function $w_{\text{RS}}(T)$ and a constant $\aleph_{\text{RS}}$. The temperature-dependent weighting function is the triangulation between the temperature ranges 256 and 270 K.

The ice crystals generated during each model timestep are added to the monitored ice number concentration, N_{ice}. Simultaneously, the riming particle freezes and is reclassified into a distinct hydrometeor category, while the number concentration of the rimed particle class remains unchanged (Kuntze, 2019). In the present thesis, rime splintering can be turned off within the ICON code.

Droplet shattering

This process is parameterized by the methodology described in Sullivan et al. (2018a). The rate of fragmentation depends on the heterogeneous freezing rate of the liquid droplet, a shattering probability function ($p_{\text{DS}}(T)$), and a constant factor ($\aleph_{\text{DS}}$) that represents the additional fragments generated per shattering event. The shattering probability function p_{DS} (with $p_{\max}$ as the maximum shattering probability) is given by a normal distribution $\mathcal{N}$ of the temperature T.

Model-generated fragments are partitioned into the ice crystal, graupel, or hail hydrometeor classes based on their size. Ultimately, a gamma-distribution is calculated for the fragments and split into three particle bins using pre-defined mass limits (Kuntze, 2019).

Collision breakup

For the current thesis, the collision breakup parameterization within the ICON model is based on the laboratory experiment work by Takahashi et al. (1995). The scheme is developed by Sullivan et al. (2018a). There is another scheme developed by Phillips et al. (2017). However, the discussion of this scheme is beyond the scope of this current thesis as it is currently not implemented in the current model setup.

The ice splinter number concentration produced from particle–particle collisions depends upon fragment number per collision(c_{BR}). The parameter c_{BR} itself depends upon the minimum temperature limit above which fragmentation occurs (T_{min}), decay rate (γ_{BR}), and a constant scaling factor (F_{BR}). The original Takahashi et al. (1995) experiment was conducted with large colliding graupel particles (around 1.8 cm diameter) (Wallentin, 2025). These are exceptionally larger than typical atmospheric ice particles. To reduce the dependency on original diameter used in the experiment formulation, linear and quadratic scaling factors have been implemented in many recent studies (Georgakaki et al., 2022; Han et al., 2024; Sotiropoulou et al., 2021b). For the current thesis, a linear diameter scaling factor based on the colliding particle diameter (D_1) and the original diameter of Takahashi et al. (1995) ($D_0 = 1.8\,\mathrm{cm}$) is applied as:

$$c_{\mathrm{BR}} = F_{\mathrm{BR}}\,(T - T_{\mathrm{min}})^{1.2} \exp\left\{-\frac{T - T_{\mathrm{min}}}{\gamma_{\mathrm{BR}}}\right\} \frac{D_1}{D_0}. \tag{3.4}$$

Table **3.4** summarizes the important parameters implemented in each SIP parameterization schemes mentioned in the above individual sections. Also, Figure **3.6** shows the temperature dependence of the three secondary ice production mechanisms implemented in the model (collisional breakup (BR), droplet shattering (DS), and rime splintering (RS)). Only the temperature-dependent parts of the SIP parameterizations are used here to obtain the curves. For RS, it is the weighting function $w_{\mathrm{RS}}(T)$, the shattering probability distribution $p_{\mathrm{DS}}(T)$ for DS, and the unscaled fragment generation function $c_{\mathrm{BR}}(T)$ for BR. However, each curve is normalized to its maximum value. This normalization removes differences in absolute magnitude and highlights the active temperature range of each mechanism. Thus, the plot emphasizes in which temperature range each SIP mechanism is most effective rather than their absolute contribution.

Rime splintering
$\aleph_{\mathrm{RS}} = 3.5 \times 10^8$ (based on the experiment by Hallett and Mossop (1974)), $w_{\mathrm{RS}}(T)$ triangular in T, $w_{\mathrm{RS}}(T) = 0$ for $T < 256\,\mathrm{K}$ or $T > 270\,\mathrm{K}$.
Droplet shattering
Values are based on the simulation study of Sullivan et al. (2018b).
$\aleph_{\mathrm{DS}} = 10$, $T_\mu = 258\,\mathrm{K}$, $\sigma = 3\,\mathrm{K}$, $p_{\mathrm{max}} = 0.2$.
Collisional breakup
$F_{\mathrm{BR}} = 50$, $T_{\mathrm{min}} = 252\,\mathrm{K}$, $\gamma_{\mathrm{BR}} = 5$, $D_0 = 1.8\,\mathrm{cm}$, diameter scaling: D_1/D_0.

Table 3.4: Overview of relevant SIP parameters implemented in this thesis.

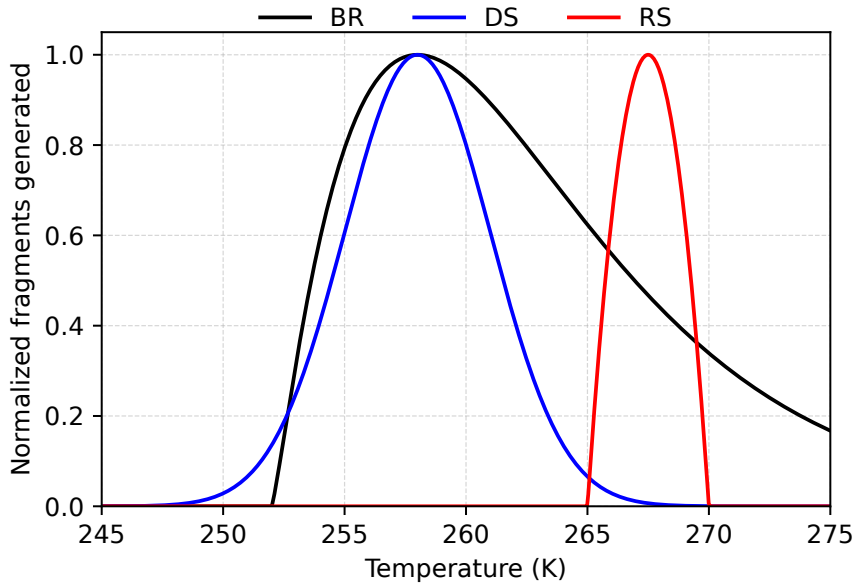

Figure 3.6: Normalized fragments generated by the three secondary ice production mechanisms: collisional breakup (BR, black), droplet shattering (DS, blue), and rime splintering (RS, red) as a function of temperature. Each curve is scaled by its own maximum.

3.4.3 Summary of other important parameterizations implemented

Model aspect	Setting
CCN activation	Based on the Segal and Khain (2006) scheme. Depends upon updraft velocity at the cloud-base.
Homogeneous ice nucleation	Limited by updraft velocity and temperature constraint (below −38 °C) (Kärcher et al., 2006; Kärcher and Lohmann, 2002)
Heterogeneous ice nucleation	Only temperature-dependent. Based on dust simulations over Europe using COSMO-MUSCAT (Hande et al., 2015)
Convection	Both deep and shallow convection are explicitly resolved; high-resolution model setup (1 km).
Turbulence	Single-column turbulence closure predicting turbulent kinetic energy via a prognostic budget equation (Raschendorfer, 2001)
Radiation	ecRad scheme using a "Monte Carlo Integration of the Independent Column Approximation (McICA)" two-stream solver for SW/LW fluxes (Hogan and Bozzo, 2018)

Table 3.5: Summary of important parameterizations used in the present thesis. In addition, some implementation details are taken from the literature: Barthlott et al. (2022a); Wallentin (2025)

3.5 Diagnostics

Some metrics are frequently used to quantify the microphysical and other outputs obtained. They are mentioned below:

Rain water budget

The concept of rain water budget is taken from Barthlott et al. (2022b) and is computed as below:

$$B = AC + ACC + MELT - EVAP - RIM - FR. \tag{3.5}$$

where 'AC' is autoconversion, 'ACC' is accretion, 'MELT' is melting, 'EVAP' is evaporation, 'RIM' is riming of rain drops, and 'FR' signifies rain freezing.

Melted-equivalent diameter

In Chapter **6**, to show the impact of SIP on particle size distributions, the concept of melted-equivalent diameter is implemented. The concept for this approach is taken from the studies by Grzegorczyk et al. (2025) and Mroz et al. (2024). The melted-equivalent diameter approach enables the direct comparison of mass distributions across different particle types. This standardization, though not reflecting the actual physical dimensions of individual species, provides a common reference frame for examining how SIP processes redistribute mass across the size spectrum.

First, the number concentration (N) in m^{-3} and the mass concentration (L) in $\mathrm{kg\ m}^{-3}$ for each hydrometeor at each vertical level is obtained. Then, using Equation **3.2** a generalized gamma distribution in mass space is fitted to these data to characterize the particle size distribution of each hydrometeor category. To enable direct comparison across species with different densities, all particles are converted to standardized melted-equivalent diameter by using the mass-diameter relationship below:

$$D = \left(\frac{6x}{\pi\rho_w}\right)^{1/3} \quad \text{and} \quad x(D) = \frac{\pi}{6}\rho_w D^3 \tag{3.6}$$

where $\rho_w = 1000\ \mathrm{kg\ m}^{-3}$ and $x(D)$ is mass per particle (kg). This allows for a standardized comparison of particle sizes across different phases. It ensures that particles of equal mass receive the same equivalent diameter, irrespective of their original phase or density, enabling an unambiguous comparison of mass redistribution. The particle size distribution is then evaluated at logarithmic diameter bins by transforming from mass space to diameter space using the Jacobian function:

$$\frac{dx}{dD} = \frac{\pi}{2}\rho_w D^2 \tag{3.7}$$

Ultimately, number density in diameter space at altitude z is obtained using the relationship below,

$$n(D_i, z) = n\big(x(D_i), z\big)\ \left.\frac{dx}{dD}\right|_{D=D_i}, \tag{3.8}$$

The total water content (TWC) in each diameter bin at altitude z is calculated as:

$$\mathrm{TWC}(D_i, z) = x(D_i) \cdot n(D_i, z) \cdot \Delta D_i \quad [\mathrm{kg\ m^{-3}}] \tag{3.9}$$

where:

- $x(D_i)$ = mass per particle (kg) at diameter bin center D_i
- $n(D_i, z)$ = number density ($\mathrm{m^{-3}m^{-1}}$) in diameter space at altitude z.
- ΔD_i = width of the diameter bin (m), with bin widths increasing logarithmically from smallest to largest diameters.

Finally the contributions from different hydrometeors are summed to obtain total TWC at each (diameter, altitude) point.

4 Orography scaling impact

This chapter explores how orography affects the convection in Corsica and Iceland. The intermediate CCN concentration (CCN07) is used for the analysis and SIP is inactive.

4.1 Case I (Corsica): 27 August 2024

4.1.1 Convective precipitation

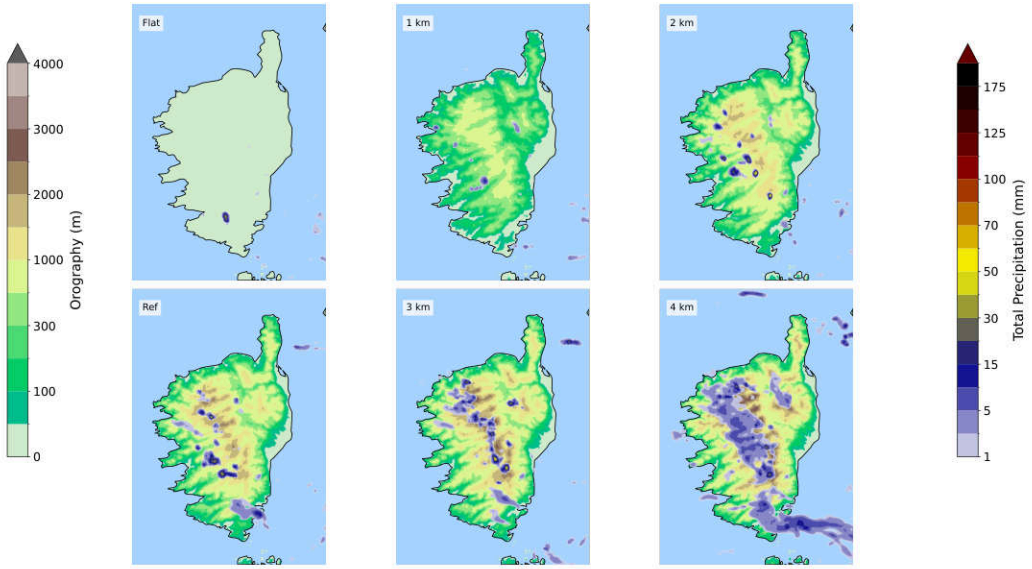

Figure 4.1: Spatial distribution of 24 h accumulated convective total precipitation.

Figure **4.1** illustrates how the spatial distribution of precipitation changes with orography scaling. In the Flat scenario, the near-absence of rainfall emphasizes the role of terrain elevation in initiating precipitation. The 1 km scenario produces moderate precipitation mainly over the central mountains and northwestern slopes, indicating initial orographic lift causing rain over windward regions. In the 2 km scenario, precipitation intensifies, particularly along western and central ridges, indicating stronger orographic influence, with increased rainfall near peaks and adjacent leeward slopes. The Reference scenario, representing actual landscape features, displays precipitation mainly over the mountainous areas across the central-northern range and western slopes. The 3 km scenario shows more intense and widespread rainfall along the central ridges and western slopes, with maxima near the highest elevations in central Corsica. The 4 km scenario shows peak precipitation totals coinciding with the tallest mountain peaks and steepest slopes, demonstrating the effects of strong orographic forcing. Rain intensity and its temporal evolution depend strongly on orography scaling

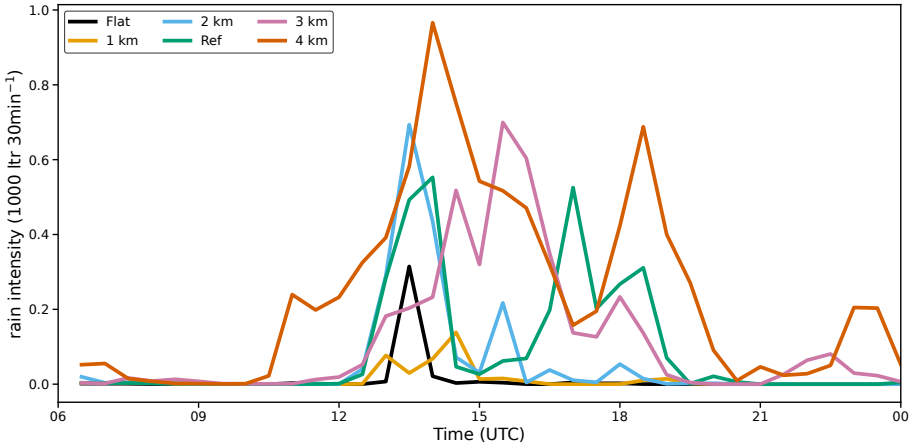

Figure 4.2: Time-series of spatially integrated rain intensities.

as well (Figure **4.2**). In the flat and 1 km cases, rainfall remains weak and short-lived, with onset delayed to around 1330 UTC, indicating limited convective triggering. The flat orography produces the lowest rain intensity. With increasing terrain height, precipitation initiates earlier, intensifies, and persists longer. Rain onset occurs between 1130–1230 UTC for the 2 km and 3 km scalings, and around 1030 UTC for the 4 km scaling. This highlights the role of terrain height in enhancing and organizing convection. Thus, a systematic positive correlation exists between precipitation onset and orography scaling.

4.1.2 Convection related parameters

Pre-convective conditions

Orography scaling substantially modifies near-surface meteorological variables, including specific humidity (q), relative humidity (rh), and 2–m temperature. To compare the pre-convective environment, domain-mean values at 0900 UTC are summarized in Table **4.1**. The 2–m temperature decreases with increasing scaled orography. Specific humidity also decreases with increasing orography scaling.

Orography	**qv$_{2m}$ (g/kg)**	**rh$_{2m}$ (%)**	**t$_{2m}$ (K)**
Flat	17.2	71.49	301.64
1 km	16.5	72.27	300.39
2 km	15.5	71.25	299.16
Ref	15.2	70.97	298.70
3 km	14.8	71.47	297.94
4 km	14.2	72.25	296.61

Table 4.1: Domain-averaged specific humidity, relative humidity and 2–m temperature over Corsica at 0900 UTC.

CAPE and CIN

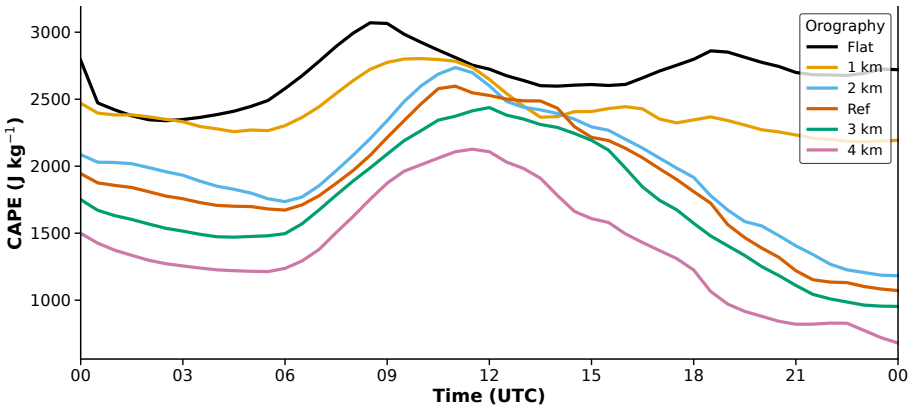

(a)

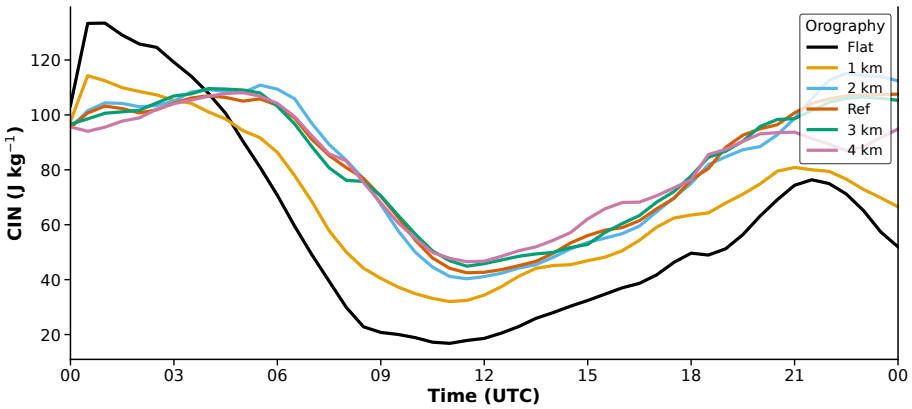

(b)

Figure 4.3: **(a)**: Time-series of spatially averaged CAPE, **(b)**: Same as **(a)**, but for CIN.

With increasing orography scaling, CAPE decreases and CIN increases, indicating a systematic relation between CAPE, CIN, and terrain elevation. This is linked with a reduced low-level moisture supply (Table **4.1**), which limits parcel buoyancy through weaker latent-heat release. In addition, peak CAPE occurs earlier in the flat and 1 km runs (0900 UTC) than in the higher orography scalings, where the maximum is reached later (1200 UTC).

Low-level wind convergence and boundary layer updraft

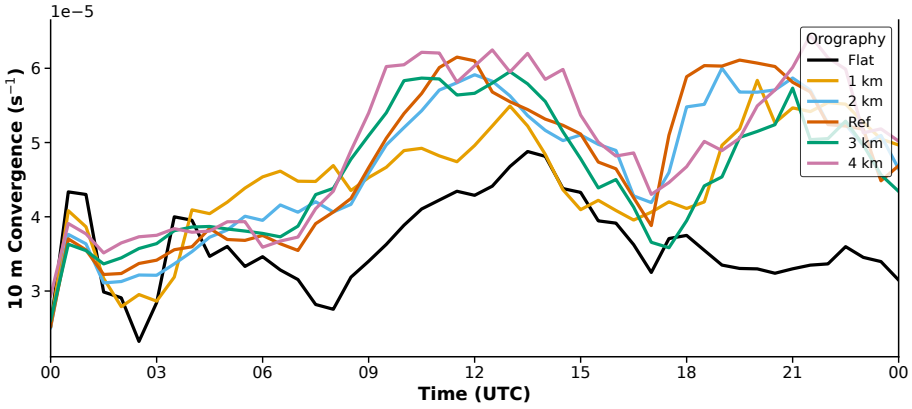

(a)

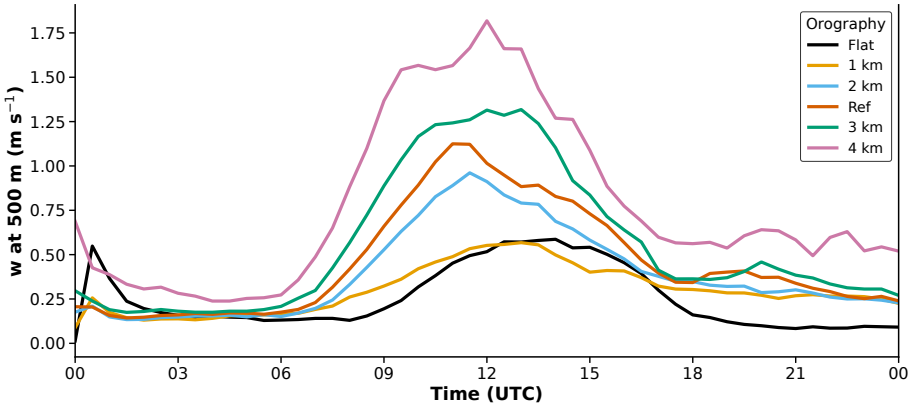

(b)

Figure 4.4: **(a)**: Time-series of spatially 10-m convergence, **(b)**: Same as **(a)**, but for upward velocity at 500-m.

Low-level wind convergence provides dynamical lifting that is crucial for convective initiation. Here, it is diagnosed by computing the divergence of the 10 m wind field and retaining only convergent contributions. Figure **4.4a** shows that accumulated convergence strengthens during the morning as thermally driven secondary circulations develop, with larger values in simulations with higher orography. This likely reflects stronger flow channeling in deeper valleys and more intense upslope winds associated with enhanced heating and steeper sensible heat-flux gradients. The strongest convergence also coincides with the period of peak rainfall intensity. Furthermore, this low-level convergence is associated with stronger vertical motion in the boundary layer. Figure **4.4b** shows that updraft velocities at 500-m increase with orography scaling. Also, the lower orography scalings (flat and 1 km) reach the maximum updraft later (around 1400 UTC) than the higher orography scalings (2 km, ref, 3 km and 4 km reach maximum updraft around 1130–1200 UTC).

However, vertical ascent can still be limited by divergence near the top of the boundary layer. The ability of the boundary layer to trigger moist convection and release CAPE is therefore evaluated using Equation **2.5**. The analysis is restricted to grid points with w_{diff}>0 and CAPE exceeding 2000 J kg^{-1}(Figure **4.5a**). The temporal evolution of the w_{diff}>0 grid-point fraction is similar across simulations, with maxima in the late morning (0900–1200 UTC), when CIN is lowest and even moderate updrafts can more readily overcome convective inhibition

Figure **4.5a** shows an unexpected result. Although higher orography produces stronger low-level convergence and boundary-layer updrafts, the fraction of grid points meeting the convection-trigger criterion decreases systematically with orography scaling. Moreover, despite the larger trigger fraction, rain intensity is lowest for the flat-orography case. This likely reflects persistent conditional stability over the flat-orography case. Figure **4.5b** indicates a persistent stable layer between 1000 and 1500 m for much of the time period, so the environment remains conditionally stable despite more grid points satisfying the trigger condition. In addition, without orographic lifting to erode CIN and reduce the LCL–LFC barrier, many parcels only marginally exceed the initiation threshold.

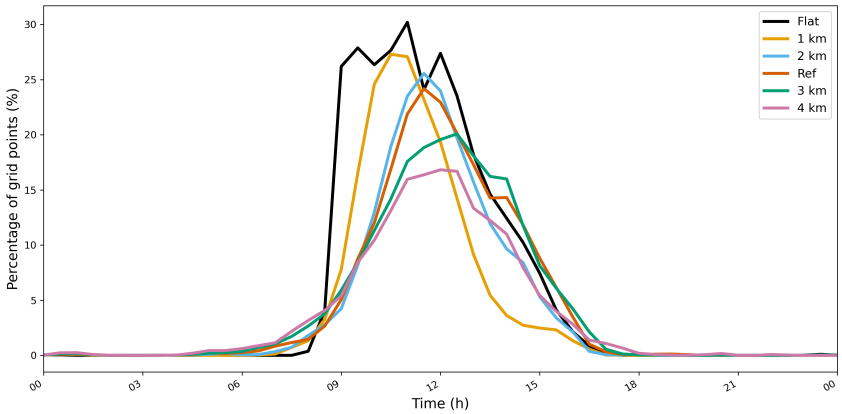

(a)

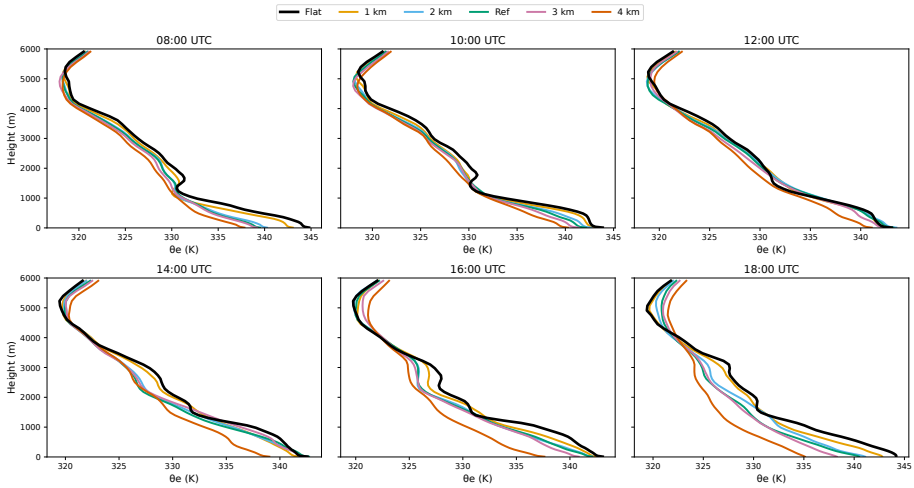

(b)

Figure 4.5: **(a)**: Percentage of grid points with CAPE > 2000 J kg^{-1} and $w_{\text{diff}} > 0$, **(b)**: Time series of vertical profiles of θ_e.

4.1.3 Convection initiating mechanism

This section analyses how the main convective cells initiate across the different orography scalings and highlights differences in convective triggering. Building on the CAPE, CIN, and low-level convergence time series in Section **4.1.2**, the focus here is on spatial maps of these fields together with low-level winds and precipitation (Figure **4.6**). This spatial examination shows how orography modulates convection initiation and the subsequent development of convective cells.

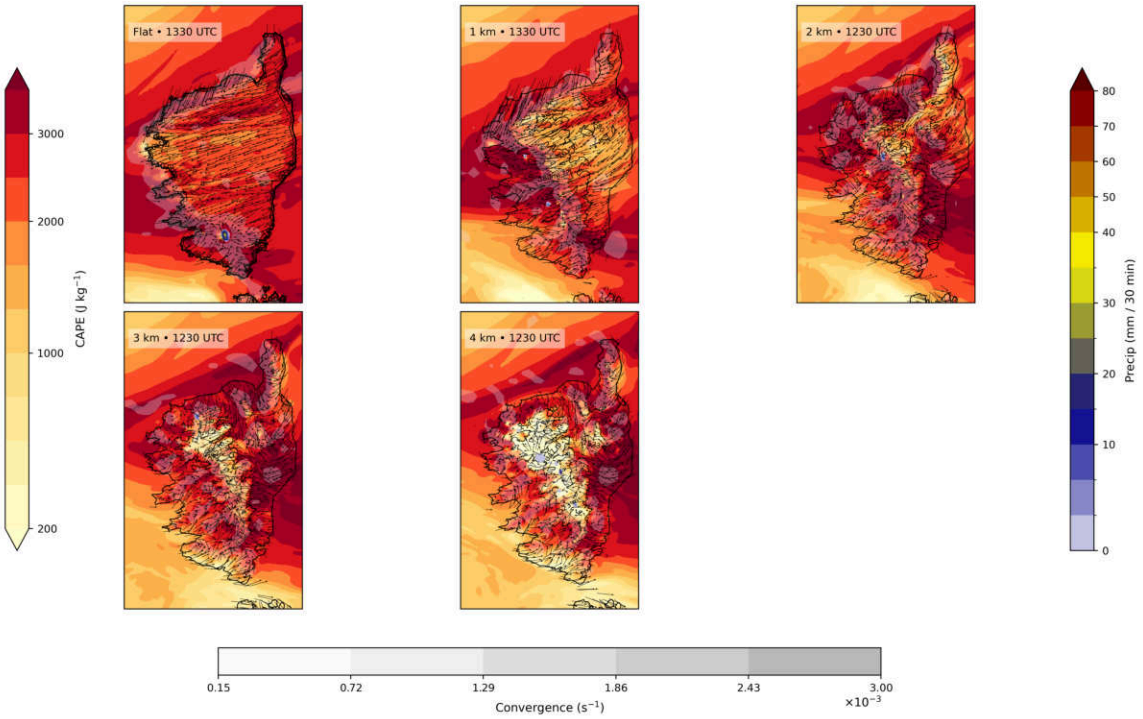

Figure 4.6: Mean-level CAPE, 30-min precipitation rates, 10-m wind arrows (low-level convergence), CIN hatched ($< 1\,\mathrm{J\,kg^{-1}}$) for different orography scalings. Surface elevation above sea level (m) is represented by black contour lines.

For the flat scaled orography, most of the domain shows mean CAPE $> 2500\,\mathrm{J\,kg^{-1}}$. However, the lack of terrain limits low-level wind convergence, delaying the first precipitation until 1330 UTC in the southern region. At 1 km scaled orography, stronger wind convergence develops along the west-central and southeastern parts earlier than the flat scaled orography, and the first precipitation forms around 1330 UTC on the western foothills. At 2 km scaled orography, convergence intensifies along a central–northwestern band and precipitation initiates earlier (1230 UTC) than the flat and 1 km scaled orography on the northwestern side, strengthening along the central band and collocating with convergence maxima. For 3 km scaled orography, terrain forcing sustains convergence from the western slopes into the central band, producing intense convective cells and early precipitation onset (around 1200–1230 UTC) that propagates along these convergence zones. The 4 km scaled orography generates the strongest and earliest low-level convergence on the west, north-central, and southwestern regions, and similarly these convective cells develop early precipitation (around 1230 UTC) along these pronounced zones of strong convergence.

Overall, CAPE is broadly available across all orography scalings, but increasing terrain height sharpens low-level convergence. As a result, convection initiates earlier and becomes more tightly tied to convergence bands, explaining the earlier and more organized precipitation in the higher-terrain simulations.

4.2 Case II (Corsica): 04 August 2024

4.2.1 Convective precipitation

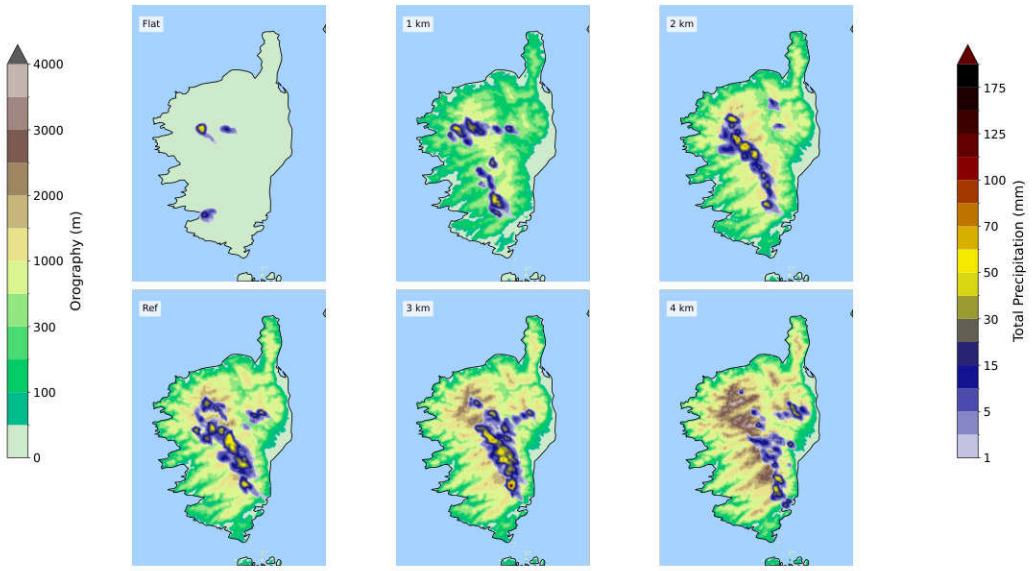

Figure 4.7: Spatial distribution of 24 h accumulated convective total precipitation.

In flat terrain, precipitation is minimal and appears as isolated cells (Figure **4.7**). Scaling the orography to 1 km produces moderate, localized precipitation, indicating orographic lifting. At 2 km and for the reference orography, precipitation becomes more organized and intense along the central ridge and northwestern slopes, where orographic forcing is strongest. At 3 km, intensification weakens over the northwestern ridges and shifts toward the eastern slopes. At 4 km, precipitation over the central and northwestern ridges decreases relative to 3 km and becomes largely confined to the southeastern slopes. The temporal evolution shows delayed onset and gradual intensification for the flat and 1 km cases (Figure **4.8**), with the lowest rain intensity in the flat-orography run. In contrast, the 2 km, reference, and 3 km cases initiate earlier and intensify more rapidly, indicating stronger convective triggering. Notably, the 4 km case exhibits a delayed onset relative to 2–3 km, indicating that the precipitation-onset response to orography scaling is not strictly linear.

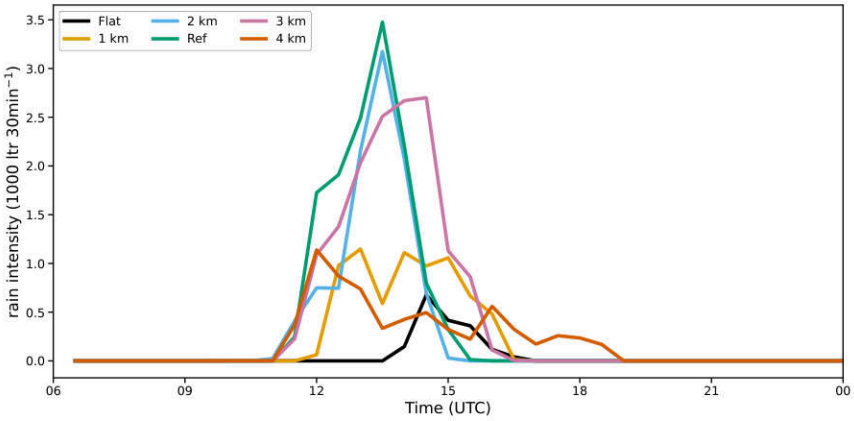

Figure 4.8: Time-series of spatially integrated rain intensities at different orography scalings.

4.2.2 Convection related parameters

Pre-convective conditions

Similar to 27 August 2024, 2–m temperature decreases with increasing orography scaling (Table **4.2**), and specific humidity also declines. However, the absolute specific-humidity values are consistently higher in this case across all scalings.

Orography	qv_{2m} (g/kg)	rh_{2m} (%)	t_{2m} (K)
Flat	18.0	69.13	302.96
1 km	17.4	70.22	301.66
2 km	16.6	71.17	300.28
Ref	16.2	70.90	299.73
3 km	15.6	70.35	298.93
4 km	14.8	70.22	297.63

Table 4.2: Domain-averaged specific humidity, relative humidity and 2–m temperature over Corsica at 0900 UTC.

CAPE and CIN

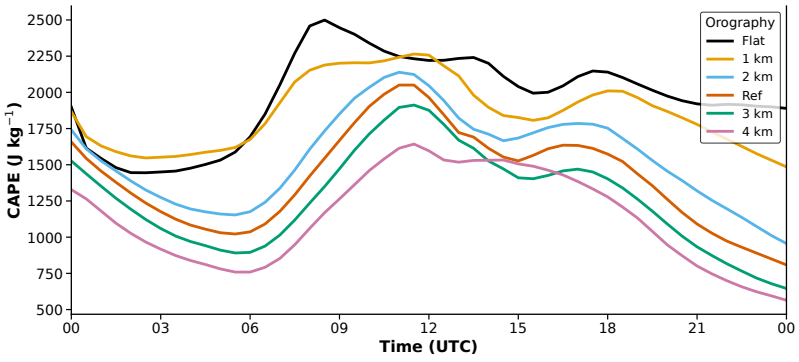

(a)

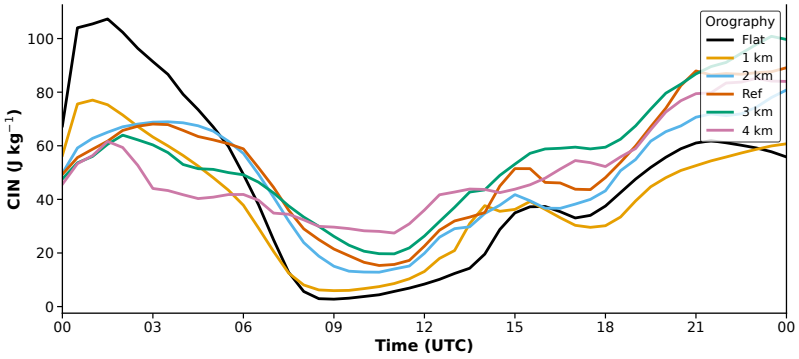

(b)

Figure 4.9: **(a)**: Time-series of spatially averaged CAPE, **(b)**: Same as **(a)**, but for CIN

There also exists a systematic connection between CAPE and CIN and the elevation of terrain, similar to the case of 27th August 2024, where CAPE decreases, while CIN increases with increasing orographic scales (Figure **4.9**). However, the maximum values of CAPE are smaller in this case by around 20% at each scaled orography.

Low-level wind convergence and boundary layer updraft

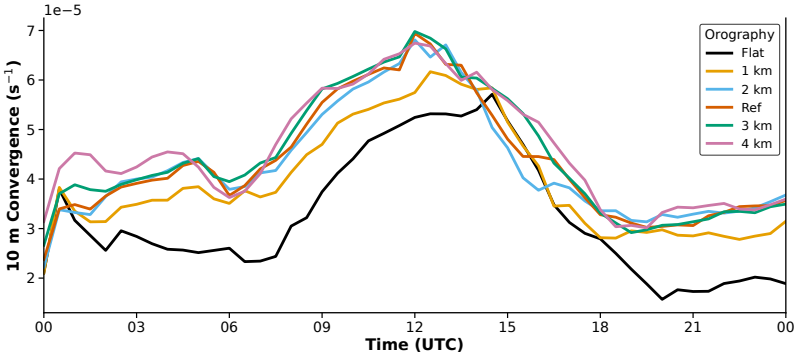

(a)

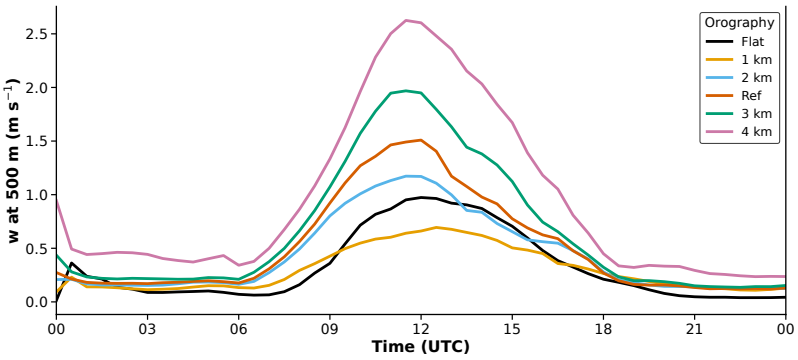

(b)

Figure 4.10: **(a)**: Time-series of spatially 10-m convergence, **(b)**: Same as **(a)**, but for upward velocity at 500-m.

The relationship between low-level convergence and orography is mostly systematic for this simulation, with the values for 2 km, reference, 3 km, and 4 km scaled orography exhibiting closely clustered convergence (Figure **4.10a**). Similarly, the relationship between updraft winds at 500–m and orography is also predominantly systematic, with only exception is that flat orography shows slightly higher boundary layer updrafts than the 1 km orography (Figure **4.10b**).

The parameter w_{diff} for this simulation day has the same type of results as for the 27th August 2024 where there is a systematic inverse correlation between the orography and the percentage of grid points where convection is triggered (w_{diff}>0 and CAPE > 2000 J kg^{-1}) (Figure **4.11a**). However, for this simulation day, for each scaled orography, the percentage of grid points where convection is triggered are much greater than for the 27 August 2024 day. The rain intensity is lowest for the flat orography as well. This is again attributed to the fact that environment remains conditionally stable for much of the period for the flat orography. It can be seen from Figure **4.11b** that there is a stable layer between 2000 and 2500 m that persists for most of the time period and in the absence of orographic lift, it is difficult to overcome this stability.

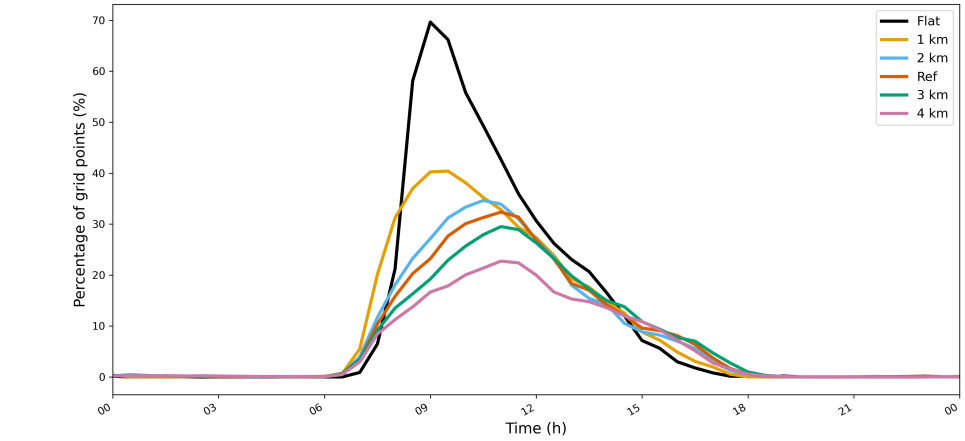

(a)

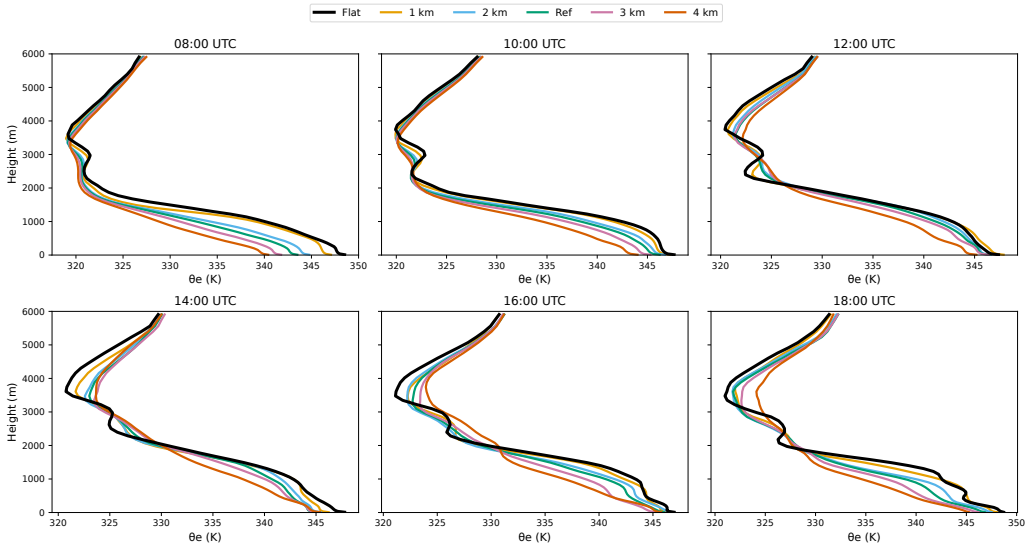

(b)

Figure 4.11: **(a)**: Percentage of grid points with CAPE $> 2000\ \mathrm{J\,kg^{-1}}$ and $w_{\mathrm{diff}} > 0$, **(b)**: Time series of vertical profiles of θ_e.

4.2.3 Convection initiating mechanism

Consistent with the case of 27 August 2024, convection on 04 August 2024 initiates where orography focuses the low-level flow into convergence bands (Figure **4.12**). The difference is the timing. By 1100 UTC, for higher scalings (1, 2, 3 and 4 km), the western coastal slopes and the central northwest-southeastern ridge already show sharp coherent convergence, and precipitating cells appear by 1200 UTC collocated with those bands. On 27 August 2024, the same precipitating cells strengthen later (1230–1430 UTC) because morning convergence is weaker and more fragmented and convective inhibition erodes more slowly. Thus, rainfall is delayed until after midday. CAPE is ample on both days. So the earlier onset on 04 August is primarily dynamical where earlier, and stronger low-level convergence is coupled with faster CIN removal, both enabled by the orographic flow.

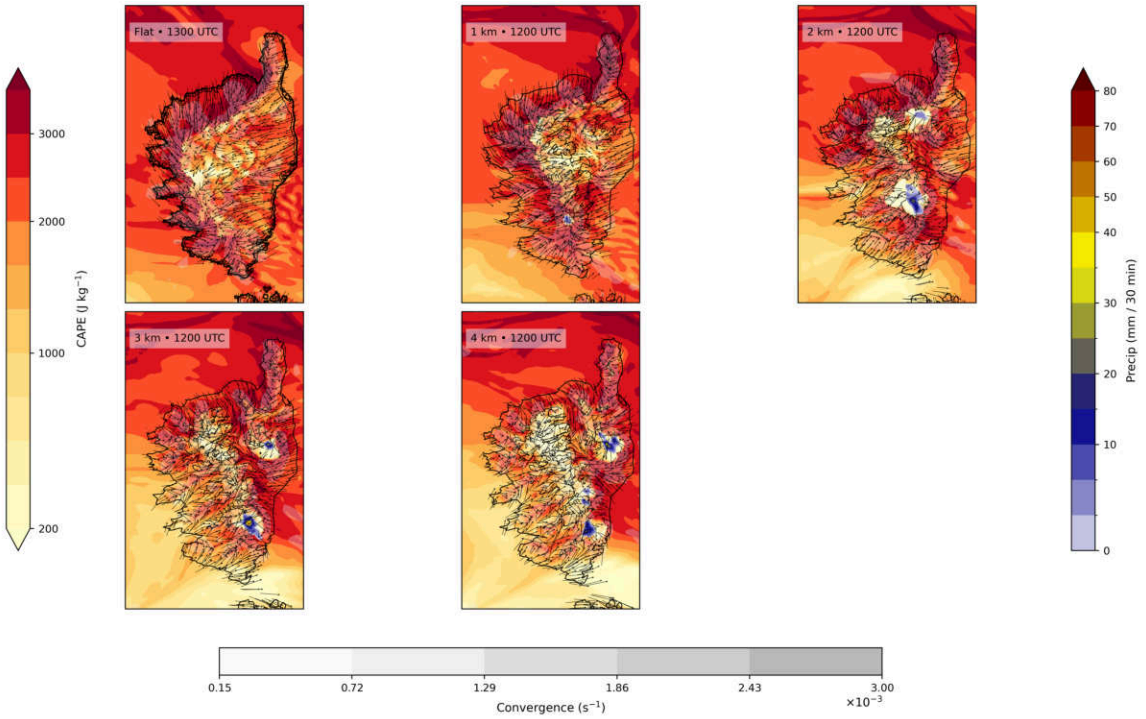

Figure 4.12: Mean-level CAPE, 30-min precipitation rates, 10-m wind arrows (low-level convergence), CIN hatched ($< 1\,\mathrm{J\,kg^{-1}}$) for different orography scalings. Surface elevation above sea level (m) is represented by black contour lines.

4.3 Case III (Iceland): 07 May 2023

4.3.1 Convective precipitation

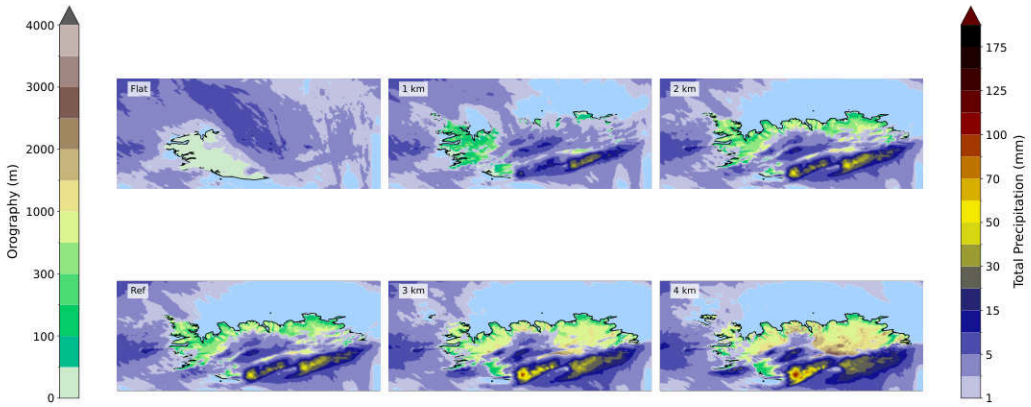

Figure 4.13: Spatial distribution of 24 h accumulated convective total precipitation.

Because the Iceland case is driven by a frontal passage, the flat-orography run already produces widespread precipitation over the central and coastal regions. Increasing terrain complexity (1, 2, 3, and 4 km scalings) enhances precipitation along the southern and central slopes, confirming a strong orographic modulation of the frontal precipitation (Figure **4.13**). Figure **4.14a** shows a

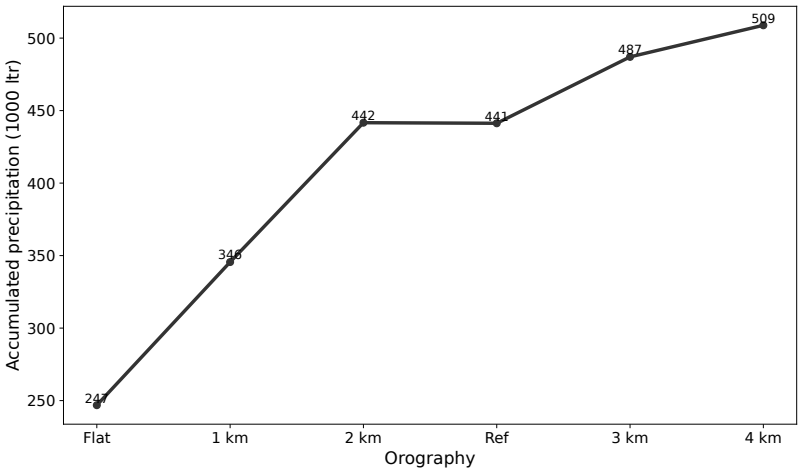

(a)

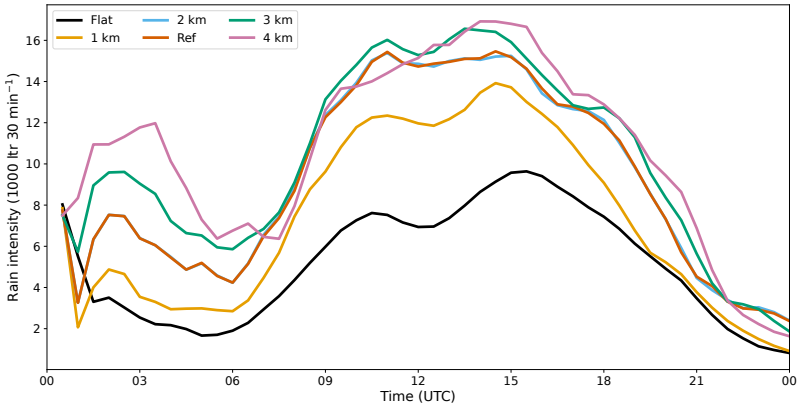

(b)

Figure 4.14: **(a)**: Total accumulated 24 h precipitation across the domain, **(b)**: Time-series of spatially integrated rain intensities

linear increase in accumulated rain with orography scaling, and **4.14b** shows a corresponding linear increase in rain intensity. Across all scalings, peak rainfall occurs between 1000 and 1500 UTC.

4.3.2 Convection related parameters

In the Corsica simulations, strong net surface solar radiation drives active thermally forced circulations, promoting buoyant ascent and, together with the preconditioning (discussed in Section **2.2.3**), supporting deep convection. Since, in Iceland, net surface solar radiation is much weaker than Corsica, convection initiation and precipitation evolution rely more on synoptic-scale dynamics. This can be seen in Figure **4.15** which shows that CAPE and 10 m wind convergence are consistently lower over Iceland than over Corsica for all orography scalings, emphasizing the different thermodynamic environments. These differences suggests that synoptic-scale forcing mechanisms, such as frontal systems, dominates precipitation over Iceland, in contrast to the thermally driven convection in Corsica.

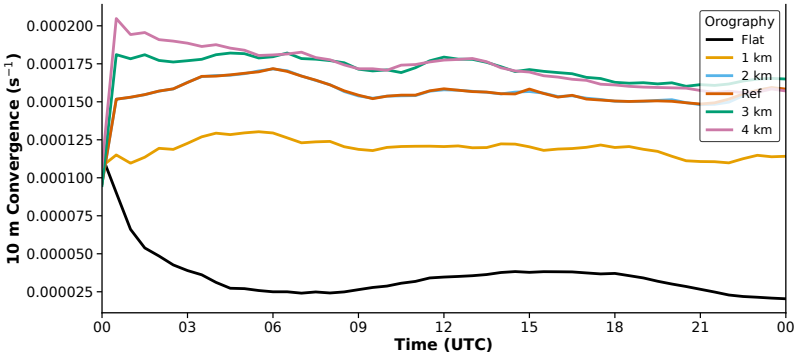

(a)

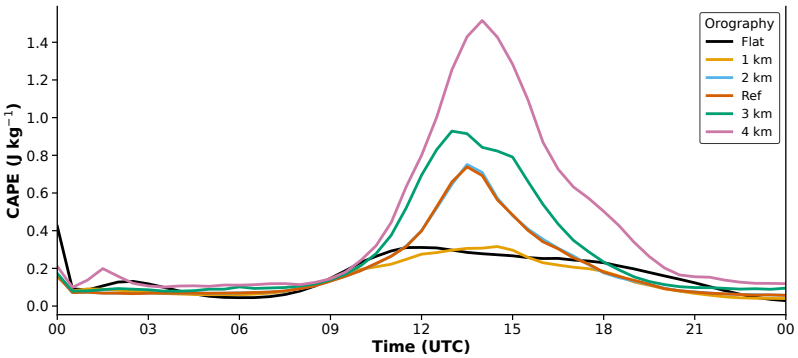

(b)

Figure 4.15: Time series of domain averaged: **(a)** 10-m wind convergence, **(b)** CAPE

4.4 General Conclusions

The two real-case Corsica simulations show a complex and subtle influence of orography on deep convection. With increasing orography scaling, the following parameters showed a systematic response on both days: **(a)** specific humidity; **(b)** 2-m temperature; **(c)** CAPE and CIN; **(d)** 10 m wind convergence and; **(e)** 500-m wind speed. These results are consistent with the earlier study by Barthlott and Kirshbaum (2013). Enhanced orography scaling is not necessary to develop deep convection over Corsica, but it modulates the timing, location, and intensity of precipitation. On 27 August 2024, precipitation onset advances systematically with increasing orography scaling, whereas on 04 August 2024 the onset is less sensitive at the higher scalings. For both days, convection developed systematically earlier as orography increases. On 27 August 2024, convection initiated approximately 2.5 hours earlier in the reference orography compared to the flat terrain. A similar trend holds on 04 August 2024, although convection develops earlier overall. This is primarily linked to the earlier establishment of organized low-level convergence facilitated by the strengthened upslope and valley flows over enhanced terrains.

The ability of the boundary layer to generate deep moist convection is measured by the parameter w_{diff}>0 coupled with CAPE > 2000 J kg^{-1}. For both the simulation days, there is a systematic negative correlation of the number of grid points showing a potential to generate deep convection with the increasing orographic scaling. However, on both days, the rain intensity is lowest for the

flat terrain, despite the higher number of grid points indicating convective potential. This is linked to the higher stability of the atmosphere for the flat terrain simulations, signifying that while potential existed, the lack of sufficient lifting mechanisms prevented effective convective development. This highlights the crucial link between thermodynamic potential and dynamic forcing, where strong orographic uplift acts as a critical catalyst for realizing convective precipitation even with reduced grid-points indicating deep convection potential.

For the Iceland simulation case, due to the lack of strong surface solar radiation, convection is primarily forced by synoptic systems, leading to widespread precipitation that is further enhanced by increasing orographic complexity. This indicates a fundamental difference in the dominant precipitation mechanisms between the two regions, with Iceland's precipitation patterns being more controlled by large-scale atmospheric dynamics and orographic forcing rather than local convective instability.

5 CCN concentrations impact

This chapter explores how the introduction of varying CCN concentrations influences cloud microphysics, and ultimately, surface precipitation in the absence of SIP mechanisms at different orographic scalings. For simplicity, the scaled heights of 1 km and 3 km are chosen as they capture the below reference and slightly above reference orographic scaling.

5.1 Case I (Corsica): 27 August 2024

5.1.1 24-h total accumulated precipitation

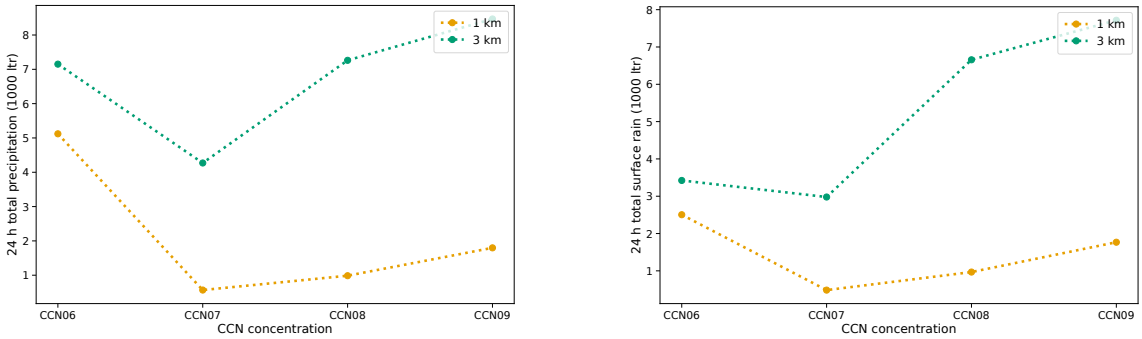

(a) (b)

Figure 5.1: **(a)**: Variation of 24 h total accumulated surface precipitation (including rain, snow, graupel and hail) and with different CCN concentrations at 1 km and 3 km scaled orography; **(b)**: Same as **(a)**, but for total accumulated surface rain only

Total surface precipitation and surface rain show similar, but non-linear, responses to increasing CCN concentration (Figure **5.1**). For 1 km scaled orography, both peak at CCN06, decrease at CCN07, and then increase from CCN07 to CCN09. The same pattern occurs for 3 km scaled orography, with higher values than 1 km at each CCN level. Since only few grid cells are simulated at 1 km, it explains the low surface precipitation observed, especially at CCN07 to CCN09. At low CCN concentrations (CCN06 and CCN07), total surface precipitation exceeds total rain, indicating contributions from other hydrometeor types (snow, graupel and hail). The composition of surface precipitation is discussed later.

5.1.2 Total column integrated hydrometeor content and microphysical processes

1 km scaled orography

The column-integrated cloud water increases systematically with CCN concentration (Figure **5.2**). This is linked to higher cloud nucleation rates (Figure **5.3a**), which produce more, smaller droplets. Smaller droplets suppress autoconversion and delay the formation of precipitation-sized drops. As a result, total rain content generally decreases with increasing CCN because accretion becomes less efficient (Barthlott et al., 2022b; Horak et al., 2021). The same trend is largely observed here as well, with an exception of slight increase when CCN concentration transitions from CCN08 to CCN09 (Figure **5.2**). This is primarily linked to the slight increase in the accretion efficiency when transitioning from CCN08 to CCN09 (Figure **5.3a**).

For cloud ice, total content shows an overall increase with increasing CCN concentrations. In deep convection, higher aerosol loading produces more small droplets that are more easily lofted into colder regions, enhancing homogeneous freezing and ice crystal formation. This is also observed in this simulation, where homogeneous freezing increases linearly with increasing CCN concentrations. It is shown further in the Figure **5.11a** in Subsection **4.2** where the homogeneous freezing of the two cases is compared. The reason for comparison is discussed separately in the respective section. Ice can further grow through the vapor deposition process. The total column integrated snow increases when ice-ice collisions happen and mechanical interlocking takes place. The systematic increase of ice with increasing CCN concentration leads to more ice-ice collisions and hence explains the increased content of snow with increasing CCN concentrations.

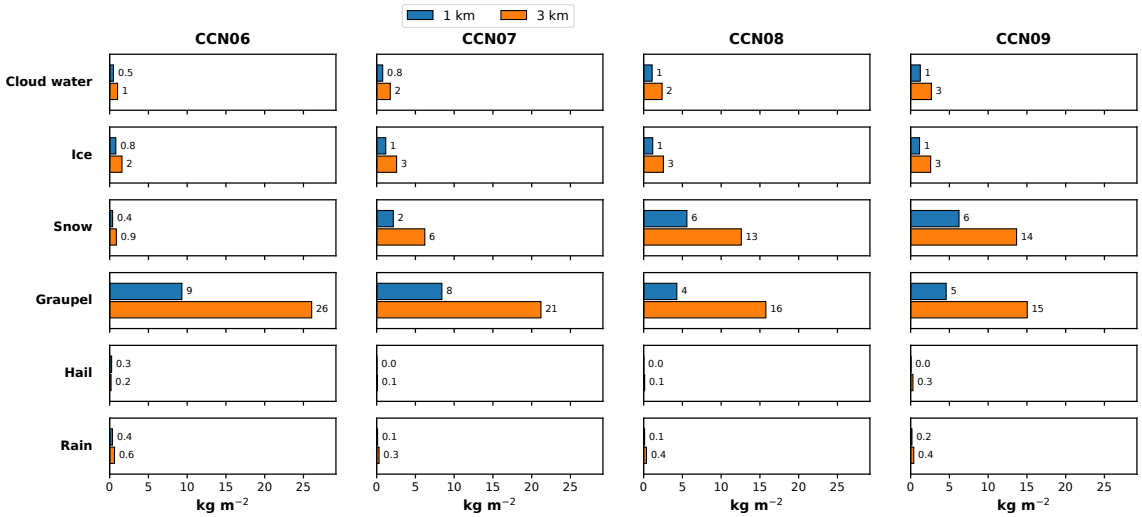

Figure 5.2: Spatially averaged and time-accumulated values of total column-integrated variables (cloud water, rain, ice, snow, graupel, hail) for 1 km and 3 km scaled orography.

For larger hydrometeors such as graupel and hail, total content is controlled by riming rates and collection. Total riming decreases with increasing CCN concentration (Figure **5.3a**). This mainly occurs because higher CCN concentration produces more small cloud droplets, which reduces the

graupel–droplet collision kernel and lowers riming efficiency (Cui et al., 2011). Figure **5.3b** shows that at low CCN concentration, riming of graupel with cloud droplets and raindrops contributes most to the rimed mass. As CCN concentration increases, smaller droplet sizes strongly reduce both graupel–cloud droplet and graupel–raindrop riming, limiting graupel growth by riming. This reduction is partly offset by stronger collection (Figure **5.3b**), especially enhanced collection of snow by graupel at high CCN concentration due to increased snow abundance. Therefore, although graupel riming decreases sharply with increasing CCN concentration, total graupel content decreases less steep because snow collection by graupel becomes more enhanced. Hail riming and collection remain much weaker than graupel processes, so hail content stays low (Figure **5.2**). Since ICON attributes riming of graupel with cloud droplets and raindrops to graupel growth rather than hail embryo formation, it is difficult to assess the exact reason for the low hail formation.

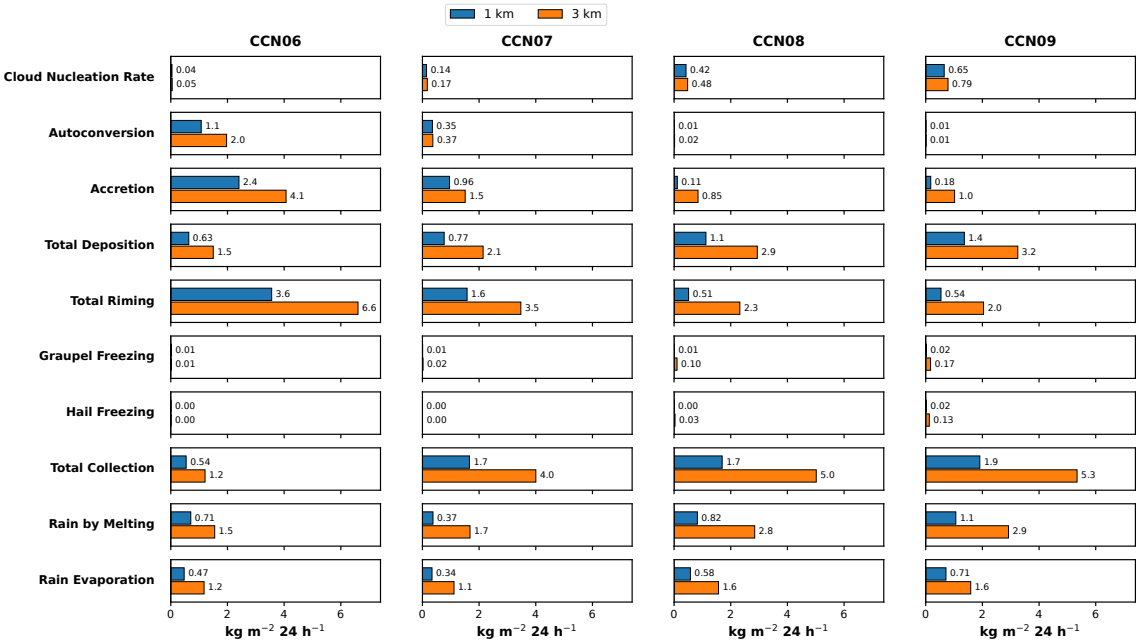

(a)

Figure 5.3: **(a)**: Vertically integrated and time-accumulated mass by microphysical processes rates for all major processes.

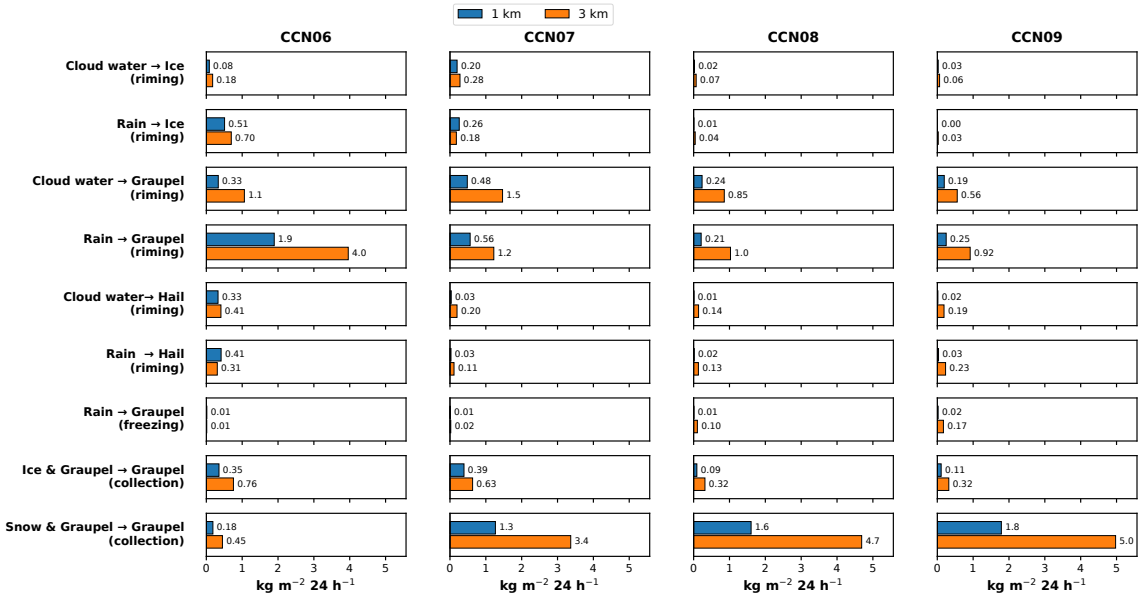

(b)

Figure 5.3: **(b)**: Same as **(a)** above, but for significant sub-processes that happen under major processes in **(a)**.

While the formation and growth of precipitation-sized hydrometeors set the initial rain and ice content in the supercooled layers, surface precipitation is also strongly modulated by melting and evaporation as hydrometeors descend through the warm layers. The relative contributions of these processes to precipitation attenuation can vary significantly with the microphysical pathways governing initial hydrometeor formation, influencing the final precipitation and its phase at the surface (Phillips, 2024). To quantify the net effect of the main source and sink terms across varying CCN concentrations, the rain water budget is calculated (Figure **5.4a**)

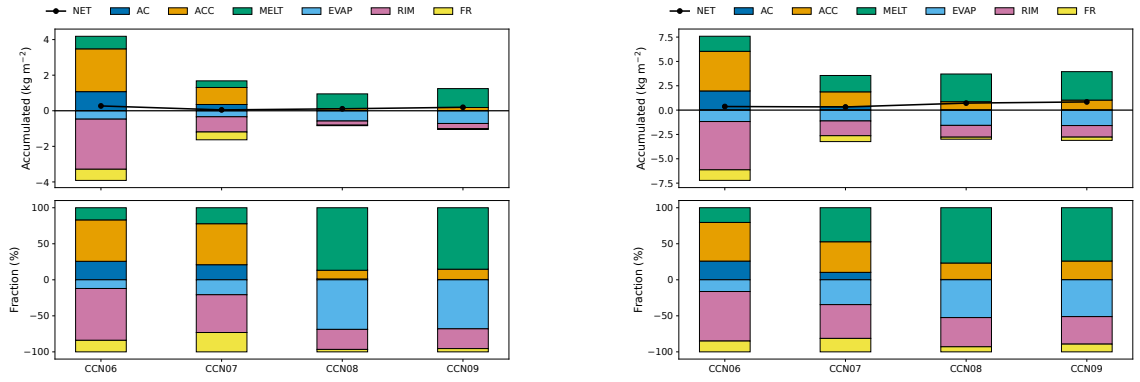

(a) (b)

Figure 5.4: **(a)**: Vertically integrated and time-accumulated (24 h) rain water budget for 1 km; **(b)**: Similar to **(a)** for 3 km scaled orography

At low CCN concentrations (CCN06 and CCN07), accretion provides the largest rain source (about 70%). Melting contributes about 10% at CCN06 and 15% at CCN07, while autoconversion contributes about 20% at CCN06 and 15% at CCN07. At high CCN concentrations (CCN08 and

CCN09), warm-rain processes are strongly suppressed and melting dominates the rain source term (around 85%). For sinks, riming dominates at low CCN concentrations, contributing about 65% at CCN06 and 50% at CCN07. Evaporation and rain freezing each contribute about 15% at CCN06 and 20% at CCN07. At high CCN concentrations, evaporation becomes the main sink (about 60%), followed by riming (about 35%).

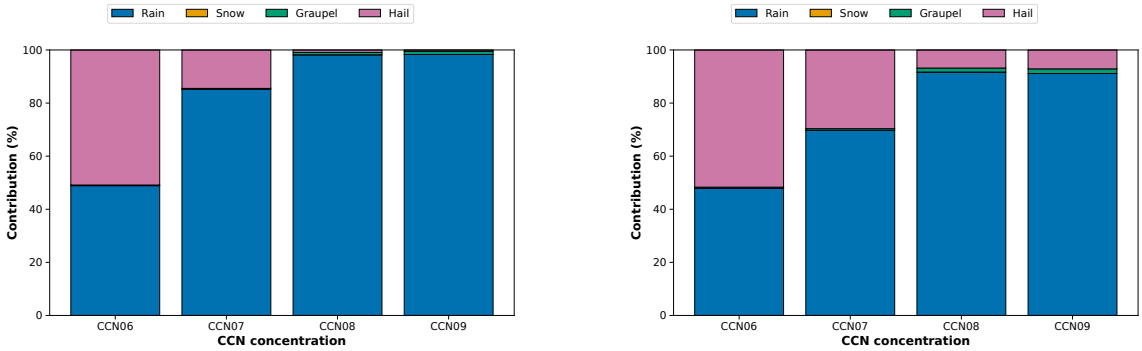

(a) (b)

Figure 5.5: **(a)**: Contribution of rain, snow, graupel and hail to the total surface precipitation at different CCN concentrations at 1 km; **(b)**: Similar to **(a)** for 3 km scaled orography.

Despite mixed-phase deep convective clouds where cold-rain processes dominate at low CCN concentration (Figure **5.3**), the rainwater budget shows that accretion contributes more to rain formation than melting. This contrasts with Barthlott et al. (2022b), where melting is the dominant rain formation source at all CCN concentrations. Here, the high surface precipitation contribution from hail at low CCN concentration (about 50% at CCN06 and 15% at CCN07; Figure **5.5**a) suggests a reduced role for melting, as a larger fraction of precipitation reaches the surface in solid form. This implies that, at low CCN concentrations, precipitation partly bypasses a substantial melting phase, increasing the relative importance of accretion in the rain budget. ICON outputs do not separate melting contributions by hydrometeor type, so the respective contributions of hail and graupel melting to the total rainwater cannot be isolated. At higher CCN concentration, smaller hail and graupel are more likely to melt completely before reaching the surface, so ice-phase precipitation converts more efficiently to rain during descent. Consistent with this, melting increases by about 120% from CCN07 to CCN08 and by about 34% from CCN08 to CCN09 (Figure **5.3a**).

Regarding evaporation, it is generally observed that higher CCN concentrations generally lead to reduced evaporative losses of raindrops, as the increased number of smaller droplets coalesce into larger raindrops that are less susceptible to evaporation (Altaratz et al., 2008; Barthlott et al., 2017). This phenomenon is attributed to the reduced surface area-to-volume ratio of larger drops, which diminishes the rate of mass transfer to the surrounding environment, thereby enhancing precipitation efficiency (Miltenberger et al., 2018). Also, the larger evaporation rates of rain at lower CCN concentrations are produced due to the enhanced availability of rain water (Barthlott et al., 2022b). In this case, however, rain evaporation tends to increase (mostly) with CCN concentration because it is controlled by the mass introduced by the melting layer into the evaporation layer. Figure **5.6b** therefore shows that evaporation profile mirrors the melting profile in Figure **5.6a**, with higher evaporation at CCN08 and CCN09 than at CCN06 and CCN07. A shallow warm-layer depth

and substantial surface hail precipitation (Figure **5.5**a) further indicate that a significant portion of hail escapes warm-layer transit, limiting both melting and evaporation at low CCN concentrations. Melting peaks within the 2-3 km vertical layers and evaporation increase in tandem and peaks below 2 km.

Thus, this co-variation of melting and evaporation arises because evaporation is supply-limited from melting layer. Because of this complex interaction of melting (source) and evaporation (sink) terms, the surface rain response is non-linear.

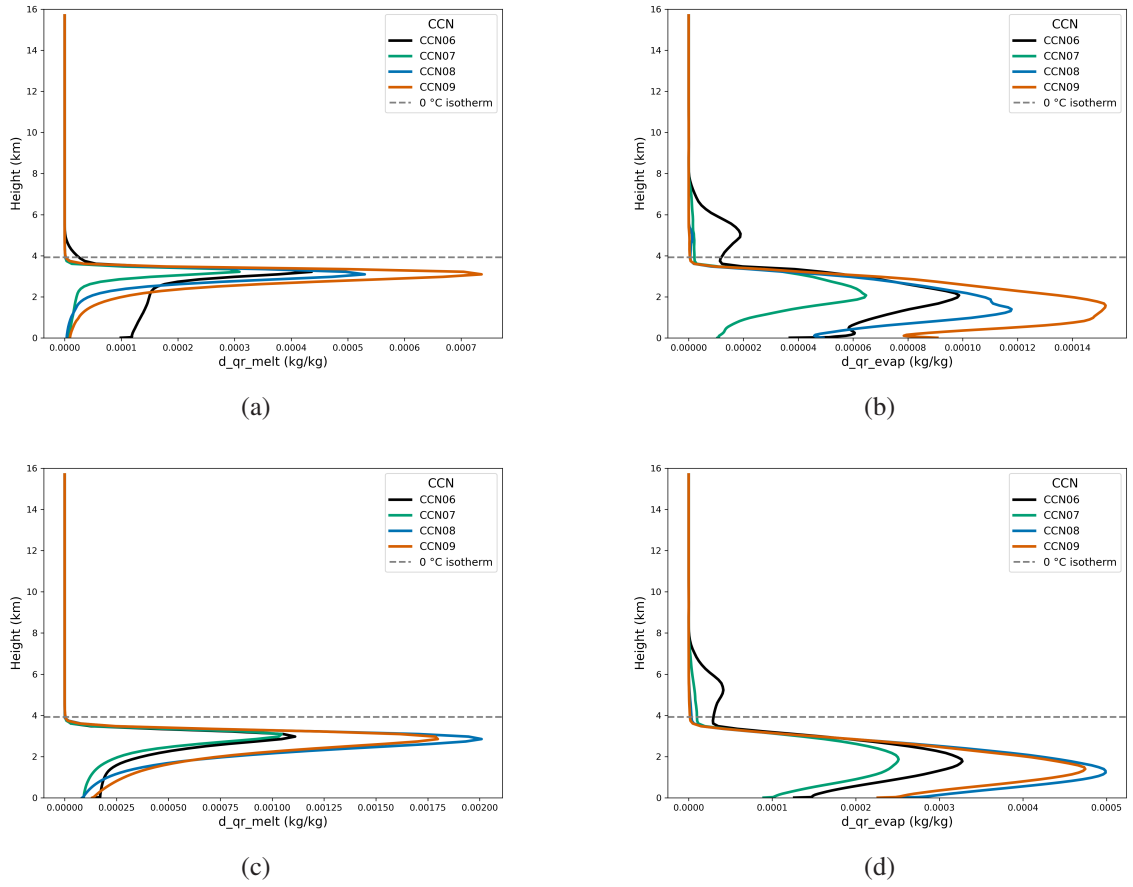

Figure 5.6: Spatiotemporal averages over the Corsica island domain (1100 UTC - 1700 UTC) for the vertical profiles of **(a)**:melting of all frozen hydrometeors to rainwater production and **(b)**: evaporation of rainwater at 1 km scaled orography; **(c,d)**: Similar profiles at 3 km scaled orography

3 km scaled orography

At 3 km scaled orography, total surface rain shows the same CCN concentration dependence as in the 1 km case, but with higher magnitudes at each CCN concentration. The key difference is that at 3 km, stronger orographic lifting, enhanced adiabatic cooling, and increased condensation systematically increases the column-integrated cloud water (Figure **5.2**). Beyond this condensate increase, the microphysical pathways scale similarly. Warm-rain and cold-rain process rates and accumulated mass are amplified at 3 km across all CCN concentrations (Figure **5.3a**, Figure **5.3b**), and the rainwater budget reflects higher absolute melting contributions while maintaining similar relative contributions (Figure **5.4b**). Surface precipitation contributions from frozen hy-

drometeors are slightly enhanced as compared to the 1 km scaled orography at CCN07–CCN09 (Figure **5.5b**). Evaporation continues to follow the melting trend (Figure **5.6c**, Figure **5.6d**). So the same melting–evaporation coupling drives a non-linear surface rain response, now shifted to higher precipitation totals due to enhanced condensate availability.

5.2 Case II (Corsica): 04 August 2024

5.2.1 24-h total accumulated precipitation

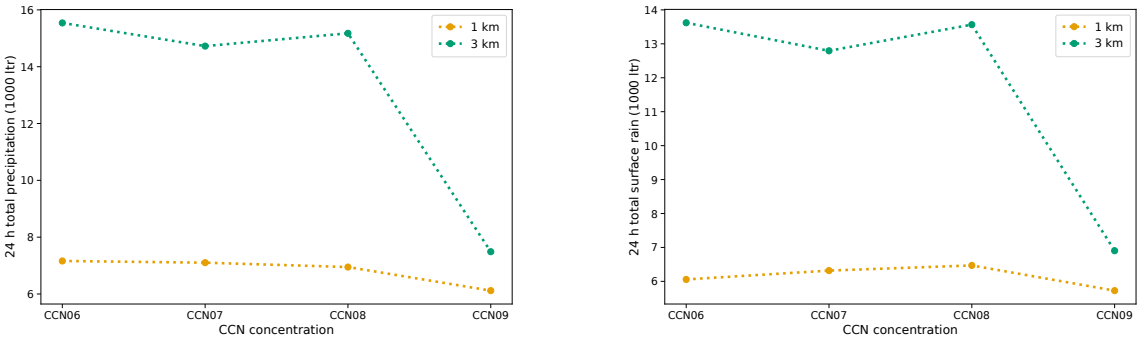

(a) (b)

Figure 5.7: **(a)**: Variation of 24 h total accumulated surface precipitation (including rain, snow, graupel and hail) and with different CCN concentrations at 1 km and 3 km scaled orography; **(b)**: Same as **(a)**, but for total accumulated surface rain only

During 04 August 2024 simulation case, total surface precipitation and surface rain again show similar, but non-linear, responses to increasing CCN concentration, as in the 27 August 2024 case. For both 1 km and 3 km scaled orography, total surface precipitation and rain are highest at the lowest CCN concentration (CCN06). However, the variation with CCN concentration differs from 27 August 2024. At 1 km scaled orography, total surface precipitation decrease by about 15% from CCN06 to CCN09. At 3 km scaled orography, CCN06 to CCN08 show small non-linear deviations, followed by a strong drop from CCN08 to CCN09 (about -55%). Total surface precipitation and rain remain higher at 3 km than at 1 km for each CCN concentration, but the relative increase differs from 27 August 2024. On 27 August 2024, the total precipitation for 3 km case increases by about 40% at CCN06, 800% at CCN07, 600% at CCN08 and 43% at CCN09 relative to 1 km, whereas on 04 August 2024 the increase is just over 100% for CCN06 to CCN08 and about 33% going from CCN08 to CCN09.

Unlike the case of 27 August 2024 where the absolute amount of total precipitation exceeds total rain considerably at low CCN concentrations, for this case, the difference is not substantial. Figure **5.8** indicates that contributions from other hydrometeor types are significantly lower compared to the case of 27 August 2024, particularly at low CCN concentrations (CCN06 and CCN07) (around 50% hail at CCN06 for 27 August 2024 vs around 15% for 04 August 2024).

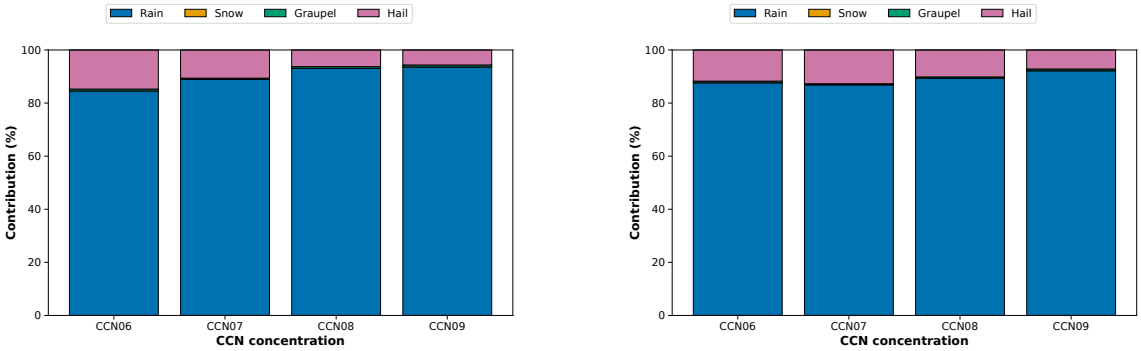

(a) (b)

Figure 5.8: **(a)**: Contribution of rain, snow, graupel and hail to the total surface precipitation at different CCN concentrations at 1 km; **(b)**: Similar to **(a)** for 3 km scaled orography.

5.2.2 Rain water budget and microphysical processes

1 km scaled orography

In the rainwater budget (Figure **5.9a**), accretion, a warm-rain process, is the dominant rainwater formation source across all CCN concentrations (around 70%). Melting, a cold-rain process, contributes a relatively constant 15%, while autoconversion is smallest. Its contribution peaks near 15% at CCN06 and decreases to negligible values by CCN09, consistent with reduced collision efficiency at higher CCN concentrations. For sink terms, evaporation and riming are strongest at CCN06, but evaporation contribution declines as rain riming and rain freezing increase. Despite a gradual increase in its share with rising CCN concentrations, rain-freezing remains the least significant process throughout all CCN concentrations.

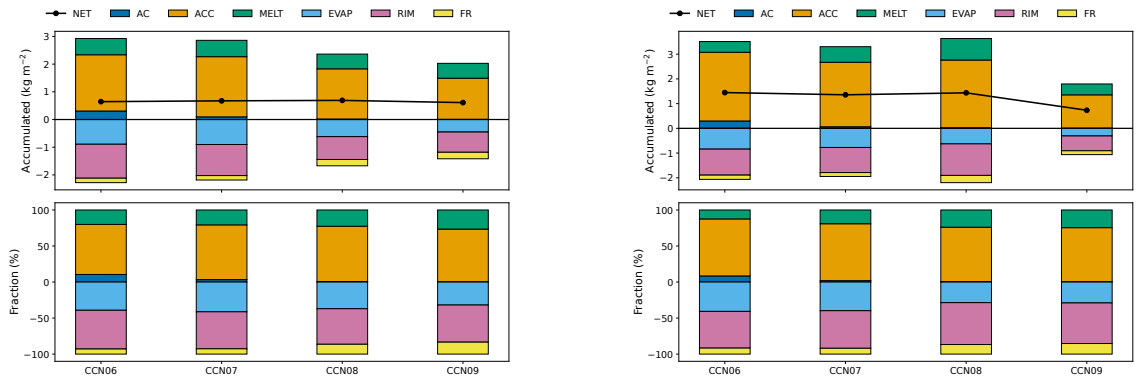

(a) (b)

Figure 5.9: **(a)**: Vertically integrated and time-accumulated (24 h) rain water budget for 1 km; **(b)**: Similar to **(a)** for 3 km scaled orography

Despite deep convection, cold-rain processes are weaker when compared to the simulation case of 27 August 2024. This indicates a stronger dominance of warm-rain pathways, even under conditions conducive to frozen hydrometeor growth. Vertical profiles of accretion and liquid water content (LWC) (Figure **5.10b**, **5.10a**) show that peak accretion rates and maximum LWC occur

at similar altitudes for each CCN concentration and are mostly confined to warm-phase layers below the 0°C isotherm. This contrasts with 27 August 2024 case, where LWC and the maximum accretion are concentrated in mixed-phase layers (not shown). Furthermore, the warm-phase layer is notably deeper (more than 5 km) than in the 27 August 2024 simulation (slightly less than 4 km). This extended warm-phase layer provides more opportunity for LWC to participate in accretion in the warm-phase layers, thereby limiting the cloud water availability for homogeneous freezing process and rain water availability for rain-freezing process at higher levels. Thus, the homogeneous freezing process is substantially more active in the 27 August 2024 case than in the current simulation (Figure **5.11**). Since homogeneous freezing is also limited by the vertical velocity, it is also observed that vertical velocity profiles for both cases are almost similar with no significant differences (not shown).

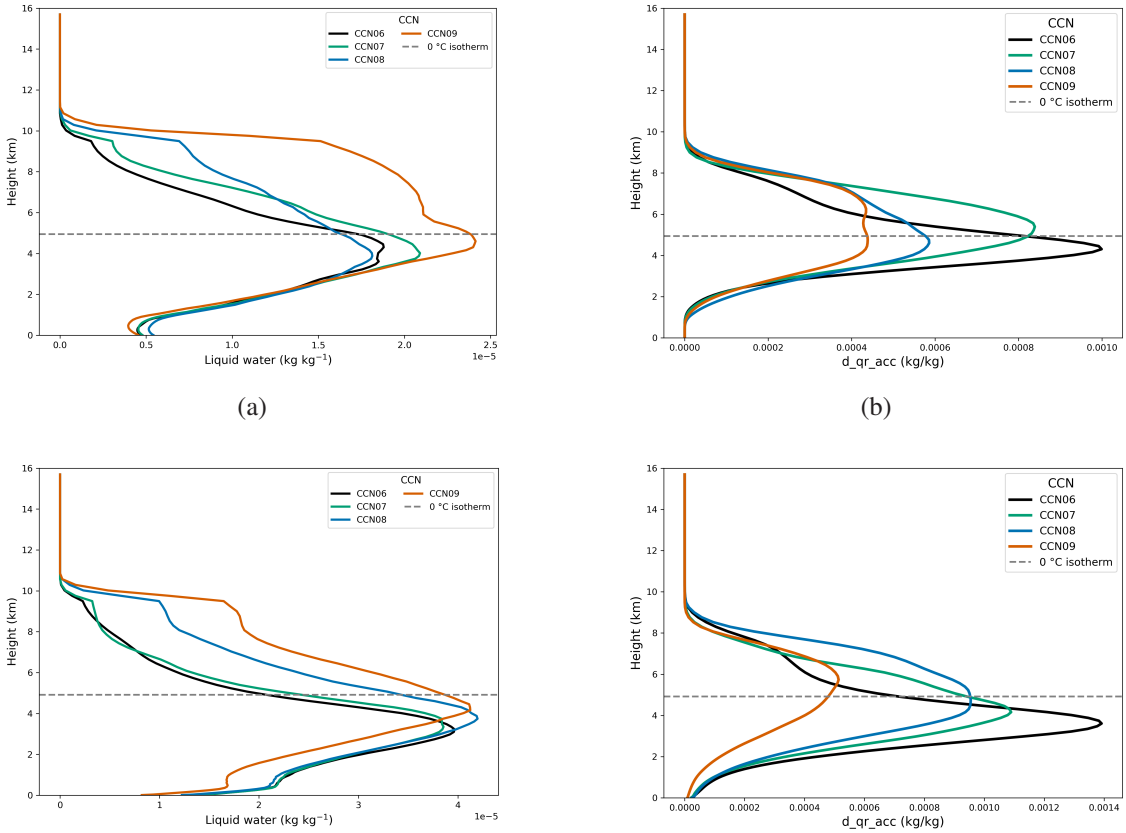

Figure 5.10: Spatiotemporal averages over the Corsica island domain (1100 UTC - 1700 UTC) for the vertical profiles of **(a)**:liquid water content (LWC) - combined rain and cloud water and **(b)**: accretion process at 1 km scaled orography; **(c,d)**: Similar profiles at 3 km scaled orography

As most LWC is consumed by accretion, warm-rain pathways dominate and cold-rain processes contribute less to hydrometeor mass formation. Riming, a key cold-rain process at low CCN concentration, is also reduced because cloud and rain particles in the supercooled layer are likely too small to rime efficiently. Figure **5.12** shows that cold-rain processes contributions to hydrometeor mass growth is suppressed relative to the simulation case of 27 August 2024. Across all CCN concentrations, accretion remains the primary hydrometeor mass conversion pathway (Figure

5.12a), followed by the riming of rain with graupel and hail (Figure **5.12b**). This suggests that initial temperature profiles can change the microphysical processes, even in environments typically conducive to ice formation.

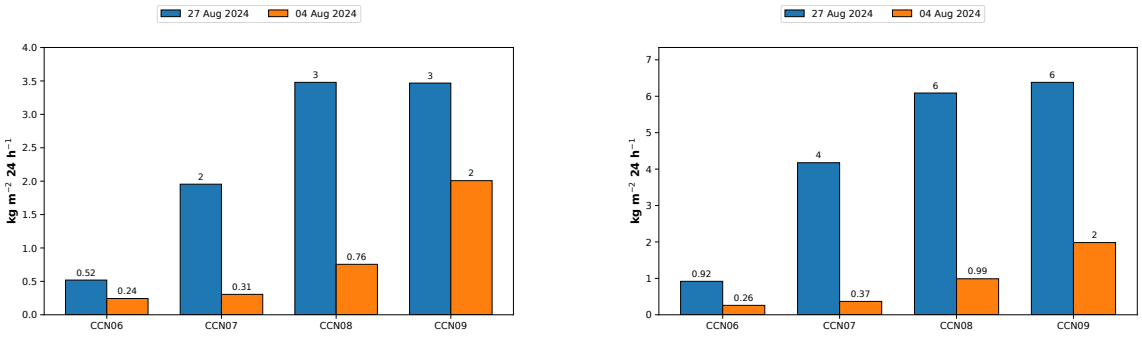

(a) (b)

Figure 5.11: Vertically integrated and time-accumulated homogeneous freezing process comparison between 27 August 2024 and 04 August 2024 for **(a)**: 1 km scaled orography; **(b)**: 3 km scaled orography

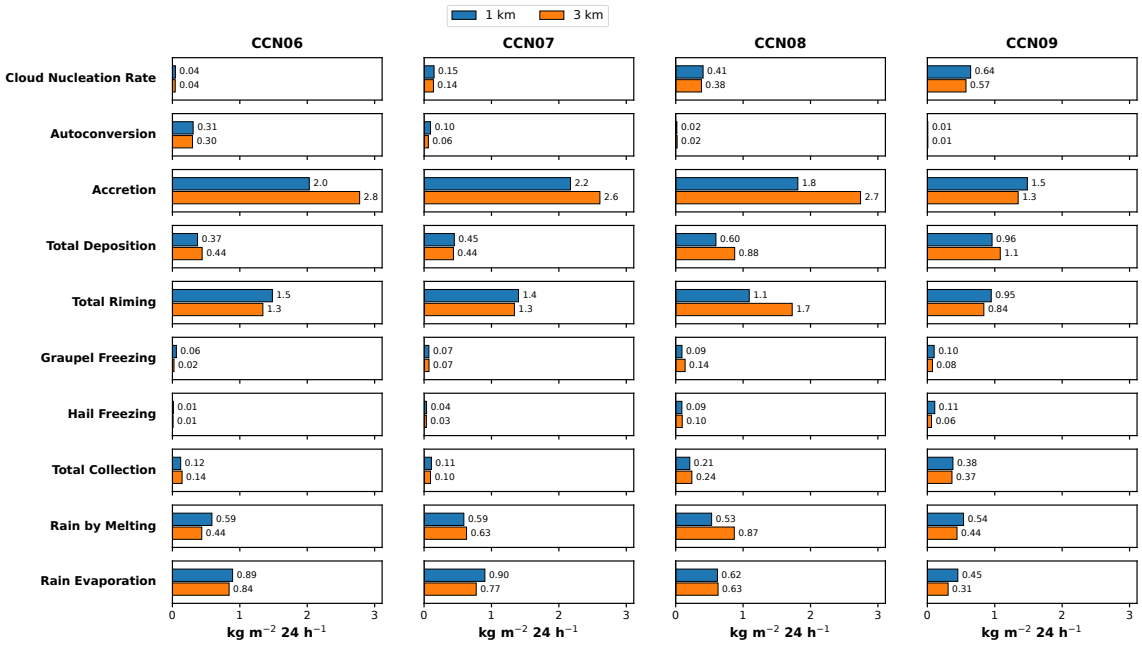

(a)

Figure 5.12: **(a)**: Vertically integrated and time-accumulated mass by microphysical processes rates for all major processes.

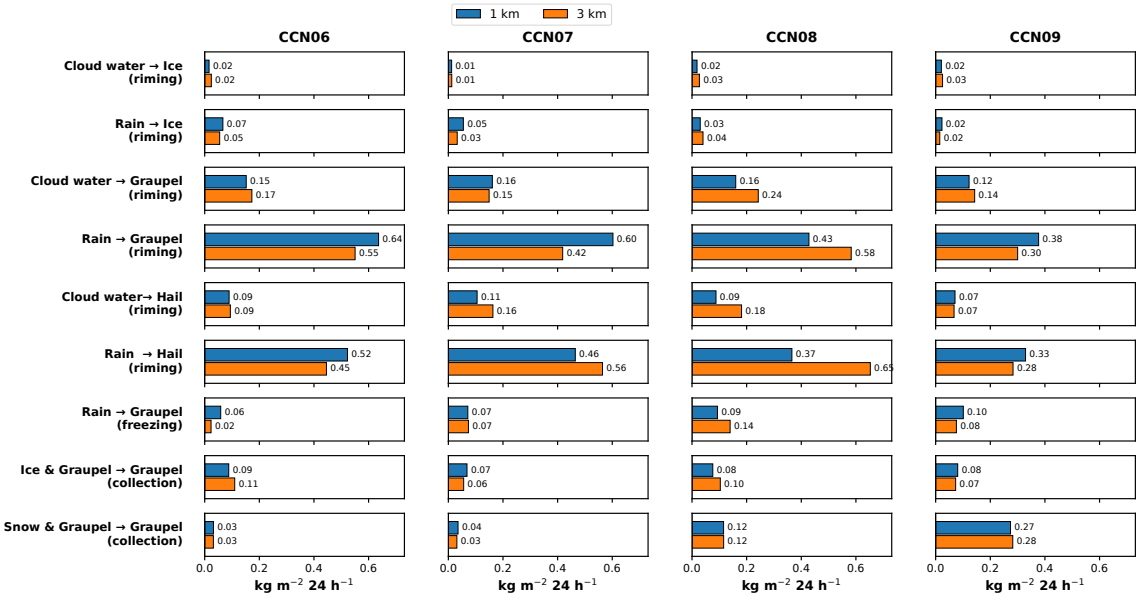

(b)

Figure 5.12: **(b)**: Same as **(a)** above, but for significant sub-processes that happen under major processes in **(a)**.

Accretion below the 0°C isotherm might be attributed to the mass introduced by melting. To ascertain whether most of the accretion occurs as an isolated warm-rain process, vertical profiles of melting are examined. In Figure **5.13a**, melting initiates just below the 0-degree isotherm and maximizes below the peak accretion zones for each CCN concentration (seen in Figure **5.10b**). This further supports the interpretation that most accretion happens as an isolated warm-rain process, rather than dependent on the mass introduced by melting. Column-integrated values indicate that melting stays relatively constant across CCN concentrations (Figure **5.12a**), consistent with the relatively constant mass accumulated by ice-phase processes (Figure **5.12**).

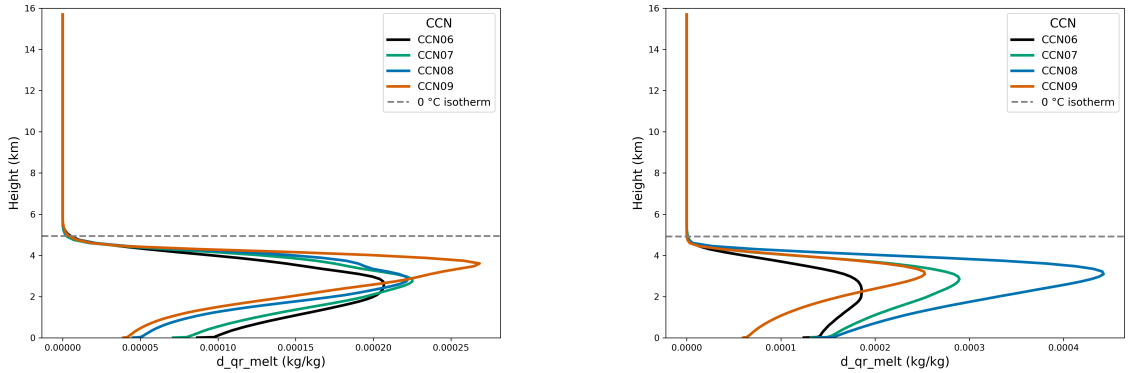

(a) (b)

Figure 5.13: **(a)**: Spatiotemporal averages over the Corsica island domain (1100 UTC - 1700 UTC) for the vertical profiles of melting process at 1 km scaled orography; **(b)**: Similar profile as **(a)** at 3 km scaled orography.

Column-integrated evaporation rates are highest at CCN06 and CCN07 and decrease at CCN08 and CCN09 (Figure **5.12a**). In contrast to 27 August 2024, where evaporation depends on melting

because cold-rain processes dominate, evaporation here is mainly controlled by the amount of rainwater supplied by accretion. Consequently, a parallel analysis of rain water and evaporation profiles is crucial. The rainwater profiles show that the lowest CCN concentration yields the largest rainwater content (Figure **5.14a**), consistent with previous work (Barthlott and Hoose, 2018). While stronger evaporation at lower CCN concentrations might be attributed to a higher number of smaller droplets, this evaporation is insufficient to eliminate the overall sensitivity in surface precipitation (Figure **5.14a**). At the levels of peak rainwater, the differences in total rainwater across CCN concentration are large, but the profiles converge towards the surface. This shows a comparatively minor deviation. In an inverse relationship to rainwater content, evaporation strengthens downward until the lower boundary layer, where rainwater becomes largely unresponsive to evaporation. This indicates that lower-level relative humidity strongly constrains evaporative losses and shapes the non-linear relationship between evaporation and rainwater (Barthlott et al., 2022b). As a result, large mid-level differences in rainwater do not translate into proportional changes in surface precipitation.

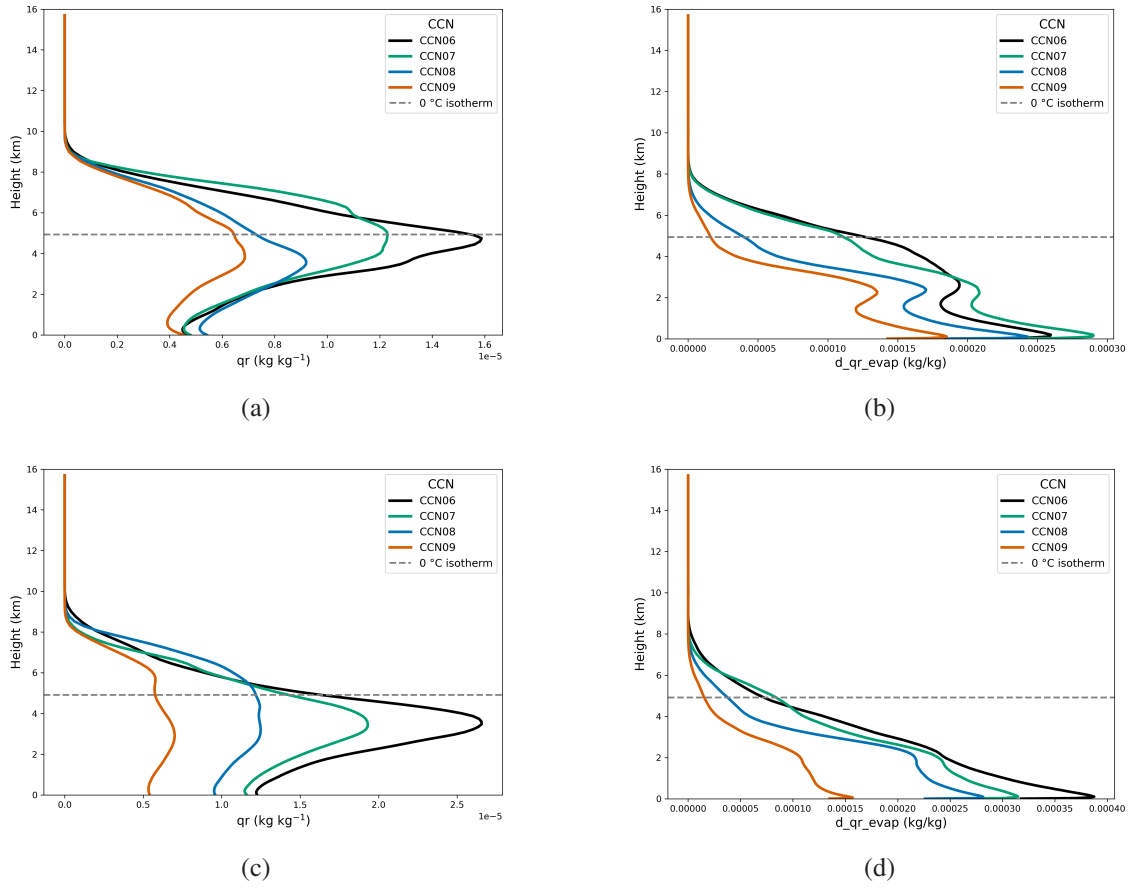

Figure 5.14: Spatiotemporal averages over the Corsica island domain (1100 UTC - 1700 UTC) for the vertical profiles of **(a)**:rain water content and **(b)**: evaporation at 1 km scaled orography; **(c,d)**: Similar profiles at 3 km scaled orography

3 km scaled orography

Similar to the 27 August 2024 case, the 3 km scaled orography yields higher surface rain than the 1 km case at each CCN concentration. However, since warm-rain processes are more dominant, enhanced orographic lifting only systematically enhances the accretion process across CCN concentrations (except CCN09) and shows non-linear response in the cold-rain processes (Figure **5.12**). Consistent with this, the rainwater budget shows substantially larger net rainwater at 3 km, primarily due to stronger accretion and weaker evaporative losses (Figure **5.9b**, Figure **5.12a**). The pronounced drop in surface precipitation at CCN09 is linked to reduced accretion (Figure **5.12a**), while the relative source–sink partitioning remains similar between the two orography scalings (Figure **5.9b**). Vertical profiles confirm that rainwater differences aloft converge towards the surface, however less sharply as compared to 1 km, and evaporation strengthens downward (Figure **5.14c**, Figure **5.14d**), with a more systematic separation than in the 1 km case, particularly at CCN09.

5.3 Case III (Iceland): 07 May 2023

5.3.1 24-h total accumulated precipitation

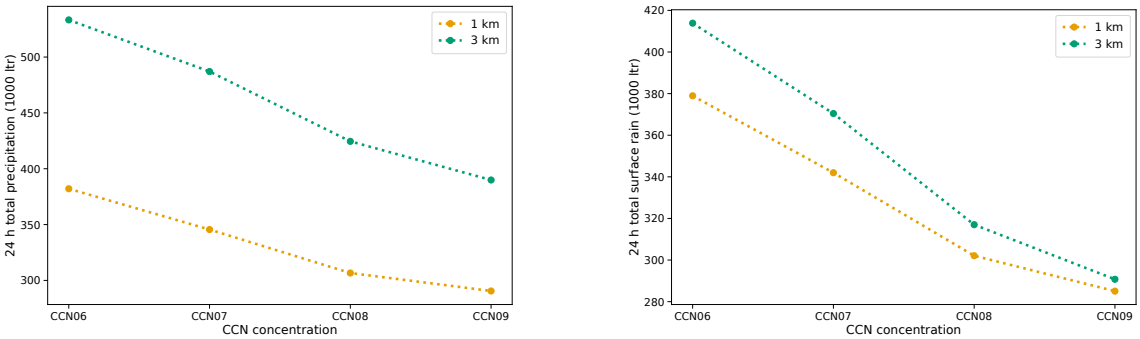

(a) (b)

Figure 5.15: **(a)**: Variation of 24 h total accumulated surface precipitation (including rain, snow, graupel and hail) and with different CCN concentrations at 1 km and 3 km scaled orography; **(b)**: Same as **(a)**, but for total accumulated surface rain only

For stratiform orographic precipitation, total surface precipitation and surface rain show a similar, systematic decrease with increasing CCN concentration. At 1 km scaled orography, both total surface precipitation and rain are highest at the lowest CCN concentration and then decline steadily as CCN concentration increases, and the same trend holds for 3 km scaled orography. Absolute values of total surface precipitation and rain are consistently higher at 3 km than at 1 km for each CCN concentration. However, at 3 km, total surface precipitation exceeds surface rain by a larger margin, indicating substantial contributions from other hydrometeor types. Figure **5.16** shows increased contributions from graupel, hail, and snow with graupel as the largest contributor after rain across all CCN concentrations. In contrast to the Corsica cases, frozen hydrometeors' contributions remain nearly constant with CCN concentration in the Iceland stratiform case.

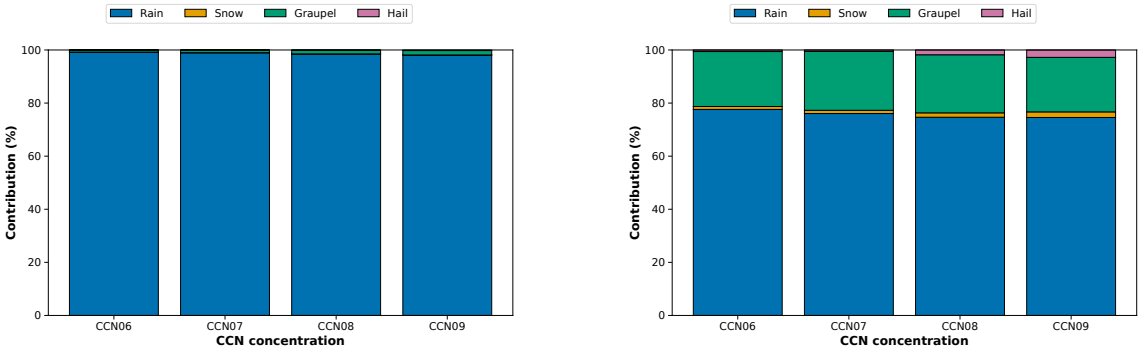

(a) (b)

Figure 5.16: **(a)**: Contribution of rain, snow, graupel and hail to the total surface precipitation at different CCN concentrations at 1 km; **(b)**: Similar to **(a)** for 3 km scaled orography.

5.3.2 Total column integrated hydrometeor content and microphysical processes

1 km scaled orography

Cloud water increases systematically with increasing CCN concentration (Figure **5.17**). This is linked to the increased cloud nucleation rate (Figure **5.19a**). However, ice formation is nearly insensitive to changing CCN concentrations, unlike in the Corsica deep convection. This reflects different cloud structures. In deep convective mixed-phase, the strong updrafts promote homogeneous nucleation of ice, whereas in this shallow mixed-phase case, updrafts are too weak to reach homogeneous-freezing temperatures. Primary ice formation therefore happens mainly through immersion freezing (Figure **5.19a**), indicating that ice nucleating particles (INPs), rather than CCN concentration, contribute to the initial ice formation in this simulation.

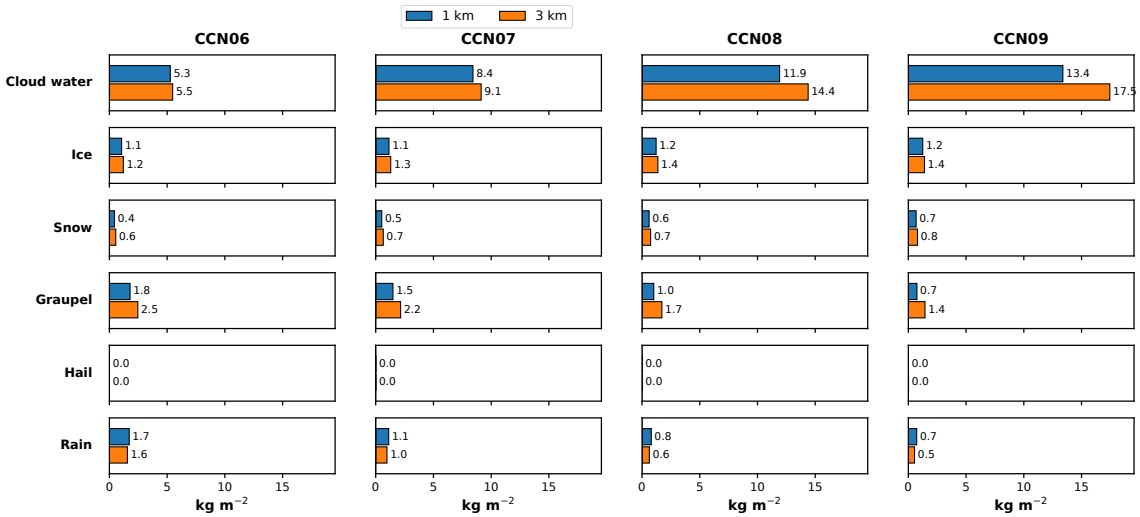

Figure 5.17: Spatiotemporal averages of total column-integrated variables (cloud water, rain, ice, snow, graupel, hail) along with total surface rain.

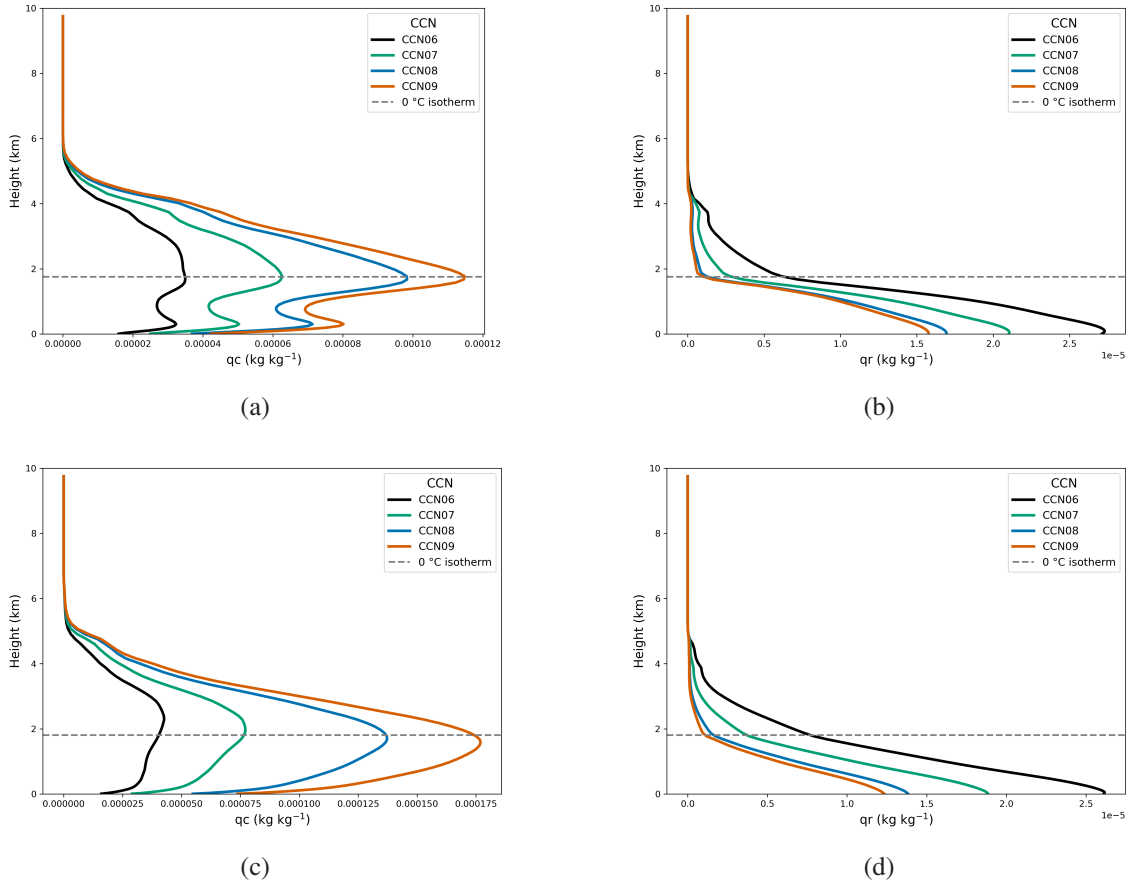

Figure 5.18: Spatiotemporal averages over the Iceland island domain (1100 UTC - 1700 UTC) for the vertical profiles of **(a)**:cloud water content and **(b)**: rain water content at 1 km scaled orography; **(c,d)**: Similar profiles at 3 km scaled orography

Since the ice content is relatively constant across all CCN concentrations, vapor deposition on ice also stays largely constant. This is shown in Figure **5.19a**, where total deposition is largely invariant with increasing CCN concentration. In contrast, total snow content is more sensitive to varying CCN concentrations (+75% from CCN06 to CCN09 vs +9% in case of ice). This is largely driven by enhanced ice–ice aggregation and ice–snow aggregation with increasing CCN concentrations (Figure **5.19b**).

For larger size hydrometeors, graupel mass decreases with increasing CCN concentration. This can be attributed to diminished riming processes. Unlike the Corsica deep-convective cases, where graupel riming with rainwater is more pronounced than with cloud water by a factor of at least five, this stratiform scenario reverses this trend, showing significantly greater riming of graupel with cloud droplets compared to rainwater. This is linked to the increased availability of cloud water in the supercooled layers than the rain water as shown in Figures **5.18a**, **5.18b**. Also, there is clear positive corelation between the CCN concentration and cloud water where the curves are distinct and separate from each other. The rain water is mostly confined to the lowest warm-phase layers. However, it is interesting to note that the collection processes accumulate systematically more mass than the riming processes across all CCN concentrations (Figure **5.19a**). At low CCN concentrations of CCN06 and CCN07 where riming is more active because of the larger cloud

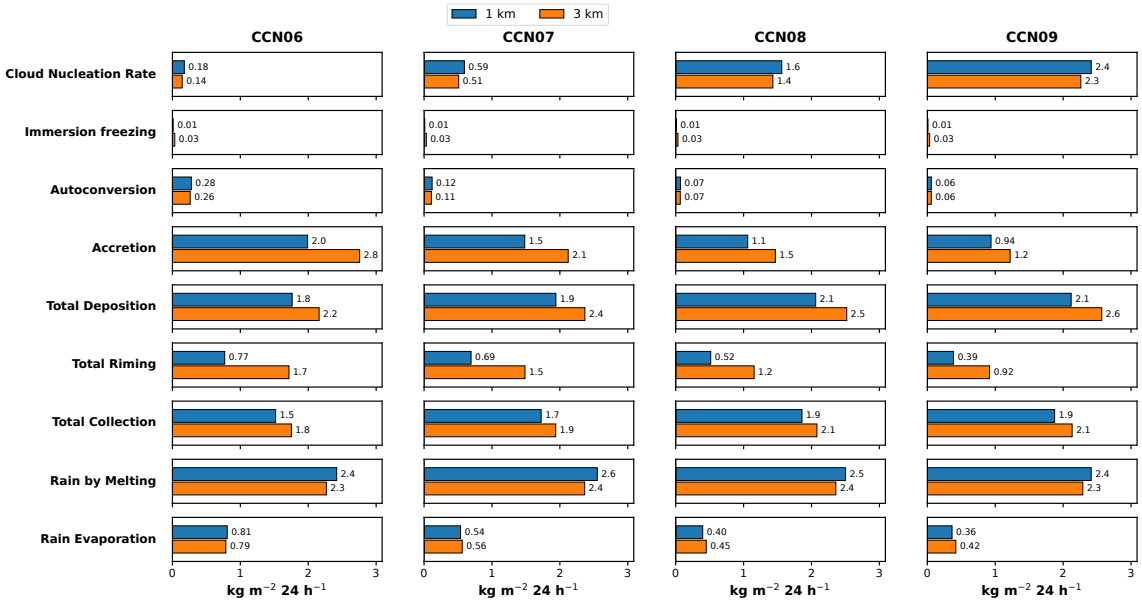

(a)

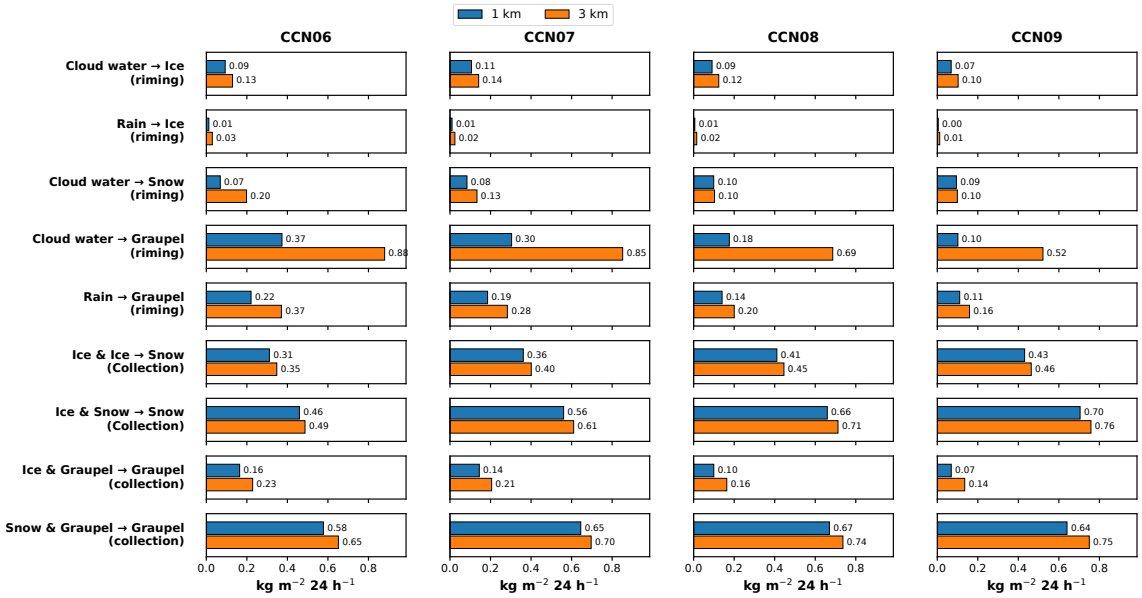

(b)

Figure 5.19: Vertically integrated and time-accumulated microphysical processes' rates for **(a)**: all major processes, **(b)**: significant sub-processes that happen under major processes in **(a)**.

droplet sizes, the overall mass accumulation through collection surpasses that from riming at least by a factor of two (or 100%). This finding contrasts with the finding of the 27 August 2024 Corsica deep convective case where mass accumulated by riming exceeded by a factor of at least seven (or around 600%) at CCN06 and by around 20% at CCN07, highlighting different dominant pathways between the cloud regimes. Although the increase of graupel by collection processes is relatively constant with the CCN concentrations (just -6% from CCN06 to CCN09) due to the sufficient availability of snow, the riming processes of graupel decreases more strongly (-71% from CCN06 to CCN09). This leads to a net reduction in the graupel content with the increasing CCN concentrations. There is no significant hail formation. This is primarily due to the absence of strong

updrafts necessary to suspend larger hydrometeors for extended growth periods through riming and collection processes.

Since the pathways involved in this simulation case are the mixed-phase pathways, it is important to consider the role of melting and evaporation in the overall surface precipitation. Figure **5.19a** shows that mass accumulated by melting shows low and non-linear deviation where melting first increases by 8% moving from CCN06 to CCN07, then decreases by 8% when moving from CCN07 to CCN09. However, the melted mass reaching the surface as precipitation varies significantly and linearly with the CCN concentration (-25% from CCN06 to CCN09). This suggests that while the total melted mass is consistent, the subsequent microphysical processes, such as accretion and evaporation, significantly alter the amount of rain reaching the ground. Since accretion is highly sensitive to the size of the cloud droplet, the melted rain undergoes differential accretion processes, where the lowest CCN concentrations, characterized by larger droplet sizes, lead to more efficient accretion, while larger CCN concentrations result in smaller droplets and consequently reduced accretion. This can be seen from Figure **5.20a** where the melting starts below the 0°C isotherm and maximizes around 1 km. The difference among the CCN concentrations is minimal. However, the accretion peaking below the melting layer demonstrates considerable variability (-54% from CCN06 to CCN09), with lower CCN concentrations exhibiting enhanced accretion (Figure **5.20b**). The evaporation is maximizing just below the accretion layer in the lowest layers (Figure **5.20e**). The evaporation is strongest at CCN06 and decreases systematically with CCN concentration (-55% from CCN06 to CCN09). This intensified evaporation at lower CCN concentrations is a direct consequence of increased rainwater content reaching these layers. However, as opposed to the Corsica deep convective cases where the evaporation profiles converged to the surface, in the present case, they show a clear difference, indicating a key difference in the evaporative sink dynamics between shallow stratiform and deep convective systems. Thus, this interplay of melting, accretion and evaporation dictates the final surface precipitation rates observed in the Iceland stratiform case.

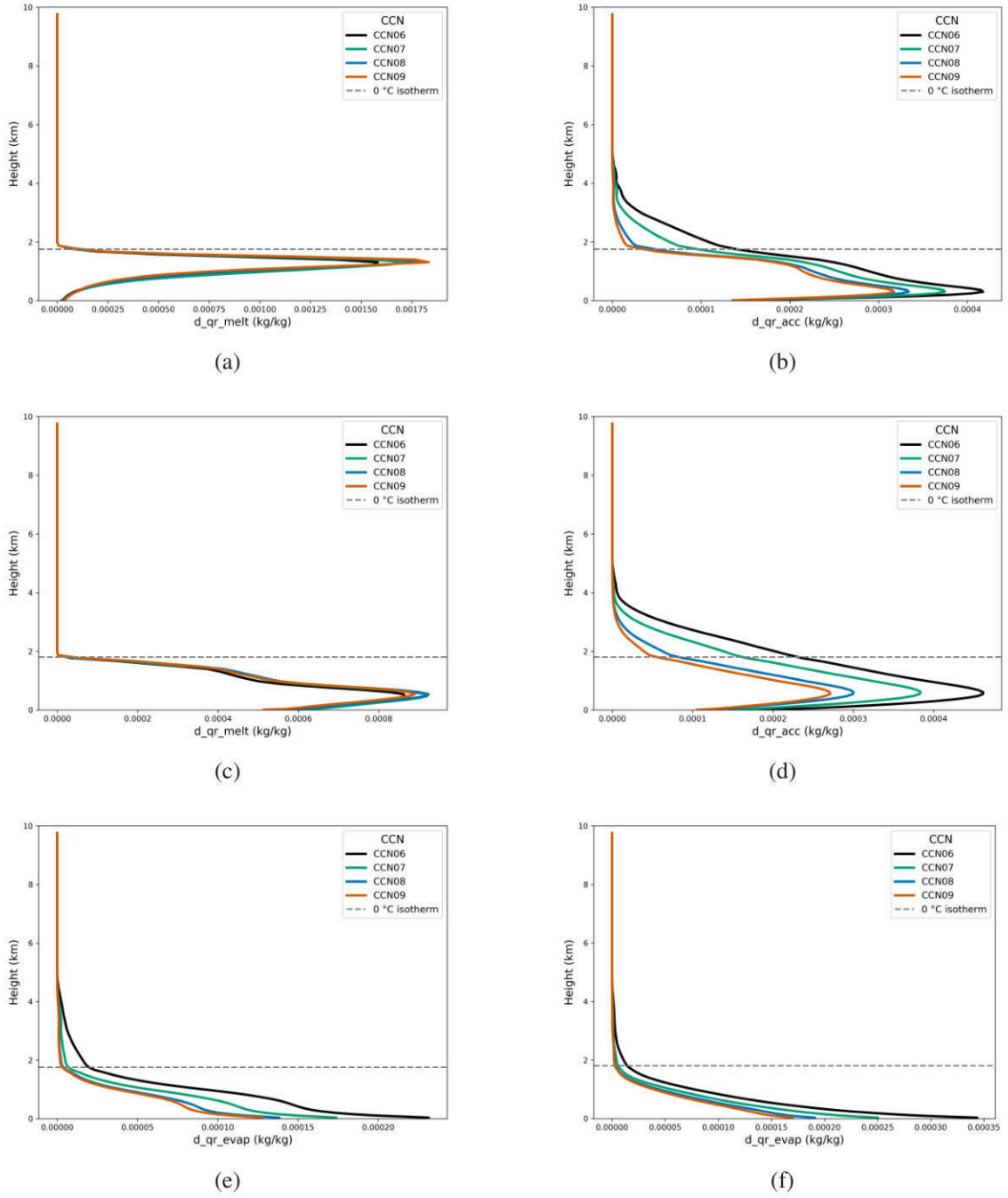

Figure 5.20: Spatiotemporal averages over the Iceland island domain (1100 UTC - 1700 UTC) for the vertical profiles of **(a)**:melting and **(b)**: accretion; at 1 km scaled orography; **(c,d)**: Similar profiles as in **(a,b)** at 3 km scaled orography; **(e)**: Spatiotemporal averages over the Iceland island domain (1100 UTC - 1700 UTC) for the vertical profile of evaporation at 1 km; **(f)**: Similar to **(e)** for 3 km scaled orography.

3 km scaled orography

At 3 km scaled orography, surface rain is higher at all CCN concentrations, while still decreasing systematically with increasing CCN concentration, consistent with the 1 km trend (Figure **5.15b**). The stronger orographic forcing increases cloud water content (Figure **5.17**), but ice increases only marginally because heterogeneous nucleation remains the dominant ice source (ranging from +9%

at CCN06 to +16% at CCN09). Snow therefore also increases slightly (Figure **5.17**). In contrast, graupel increases substantially (ranging from +38% at CCN06 to +50% at CCN09), driven by enhanced riming with cloud droplets (Figure **5.19b**). Higher supercooled cloud droplet availability at 3 km (Figure **5.18c**) for each CCN concentration amplifies graupel–cloud droplet riming (ranging from +133% at CCN 06 to +500% at CCN 09).Due to a modest increase in snow content, frozen hydrometeor growth by collection increases only weakly (ranging from +6% at CCN06 to +12% at CCN09).

Despite higher frozen hydrometeor mass at 3 km scaled orography, especially graupel, the accumulated melting mass does not increase (Figure **5.17**). Melting remains nearly identical to the 1 km case at each CCN concentration (Figure **5.19a**) . This is likely attributed to larger graupel particles, which have a greater sedimentation velocity, spending less time in the warm-phase layers before reaching the surface as precipitation. Hence, they do not contribute to the mass accumulated by the melting process. Consistent with this, graupel contributes a larger fraction to surface precipitation at 3 km (Figure **5.16b**), so the 1 km versus 3 km difference is smaller for surface rain than for total surface precipitation (Figures **5.15a**, **5.15b**). Furthermore, the peak melting levels are lower than those observed with the 1 km scaled orography and align with the peak accretion levels (Figures **5.20c**, **5.20d**). Due to the inconsistent melting variation at the 3 km scaled orography, evaporation varies less systematically relative to 1 km (Figure **5.19a**), but it decreases with increasing CCN concentration and peaks in the lowest layers below accretion (Figure **5.20f**).

5.4 General Conclusions

Two days of real-days simulations of deep convection over Corsica demonstrate a complex coupling between orography scaling, CCN concentrations and surface precipitation. When orography is scaled at constant CCN concentration, total surface precipitation and surface rain increase systematically on both days, although the magnitude of the response differs between cases. The precipitation enhancement with increasing orography scaling is attributed to stronger lifting over higher scaled terrain, which intensifies adiabatic cooling and condensation. This produces more cloud water content at higher scaled orography. This initial condensate difference then propagates further through the precipitation-forming microphysical pathways. The dominant pathways, however, diverge significantly between the two case studies, leading to distinct and non-linear sensitivities in surface precipitation when varying the CCN concentrations. On 27 August 2024, cold-rain pathways contribute a larger fraction of the rainwater production budget at each CCN concentration, and the mass accumulated by cold-rain processes increases systematically with orographic scaling. Precipitation formation is therefore closely linked to cold-phase microphysics. However, on 04 August 2024, warm-rain processes dominate the rainwater production budget. This could be due to the deeper warm-phase layer than on 27 August 2024. This promotes efficient accretion, a warm-rain process, below the freezing level for the rain formation. These fundamental differences in the microphysical pathways between two case studies lead to contrasting surface precipitation response to different CCN concentrations at each orography scaling. Also, the surface precipitation contributions from different hydrometeors vary substantially. For the 27 August 2024

case, hail contributes significantly at both orography scalings at low CCN concentrations (around 50% at CCN06 and around 20% at CCN07). For the 04 August 2024 case, rain is the primary contributor to surface precipitation across all CCN concentrations (more than 90%). Thus, although surface precipitation increases with orographic scaling in both cases, the specific microphysical mechanisms driving the sensitivity of surface precipitation to CCN concentrations are distinct from one another.

For the Iceland simulation case, the effect of modifying orography on total surface precipitation is qualitatively similar to the Corsica cases with higher scaled orography systematically increasing the total surface precipitation and surface rain. However, because of the different cloud structure, the variation of surface precipitation with increasing CCN concentration shows a different response compared to the Corsica cases. The precipitation decreases linearly and systematically with increasing CCN concentrations. This is opposite to the behavior observed in Corsica, where the relationship is non-linear and more complex. The cold-rain processes consistently dominate the precipitation formation, where at low CCN concentrations (CCN06 and CCN07), the riming and collection accumulate the mass in the mixed-phase layers, which is then melted in the warm-layers and undergoes further accretion in the lowest levels and produce the higher surface precipitation. Accretion is sensitive to the size of the cloud droplets and at high CCN concentrations (CCN08 and CCN09), the cloud droplets are smaller. This reduces the efficiency of accretion, thereby reducing the overall precipitation. In comparison to the Corsica case studies where the precipitation contributions from different hydrometeors is not changing significantly with orography at each respective CCN concentration, in the Iceland case, an increase in graupel contribution to surface precipitation is observed with higher scaled orography across all CCN concentrations. Also, the sensitivity of the contributions to the CCN concentration is substantially less pronounced than in the Corsica cases.

6 SIP impact

In the previous chapter, it was shown how the introduction of different CCN concentrations affect the cloud microphysics and ultimately surface precipitation in the absence of SIP mechanisms. This chapter explores how the activation of SIP processes alters the precipitation characteristics previously observed, with a focus on the changes in the microphysical pathways and their subsequent impact on surface precipitation.

6.1 Case I (Corsica): 27 August 2024

6.1.1 24-h total accumulated precipitation

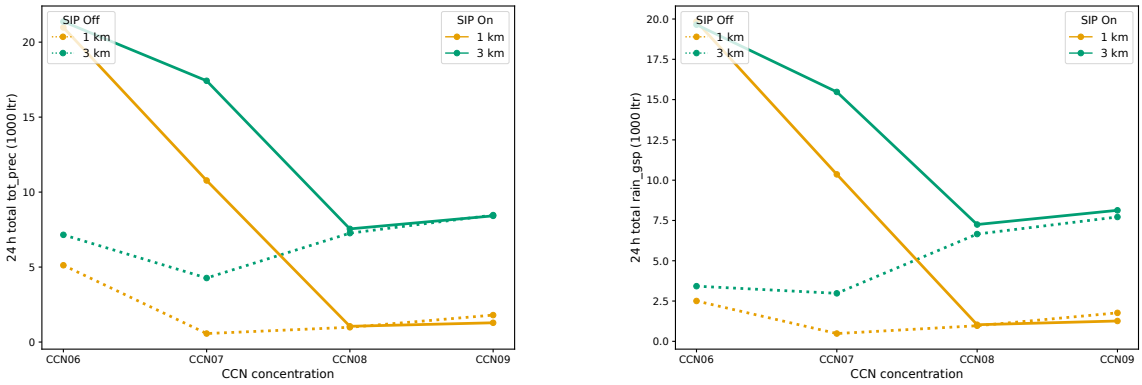

(a) (b)

Figure 6.1: **(a)**: Variation of 24 h total accumulated surface precipitation (including rain, snow, graupel and hail) with different CCN concentrations at 1 km and 3 km scaled orography for SIP On and SIP Off scenarios; **(b)**: Same as **(a)**, but for total accumulated surface rain only

Figure **6.1** shows that introducing SIP mechanisms leads to greater total surface precipitation and surface rain at low CCN concentrations (CCN06 and CCN07) for both orography scalings. Conversely, at higher CCN concentrations (CCN08 and CCN09), the difference in total surface precipitation and rain between the SIP scenarios diminishes. Furthermore, within the SIP-On scenario, surface rain is dominant and contributions from other hydrometeor types are insignificant. This can be seen from Figure **6.2a**, where at 1 km scaled orography the hail contribution to the surface precipitation is around 5% at CCN06 and less than 5% at CCN07. This contrasts with the findings in Figure **5.5** of Subsection **5.1.2**, in the SIP-Off simulation, where hail and graupel contributed significantly more to total surface precipitation. This discrepancy is further discussed below.

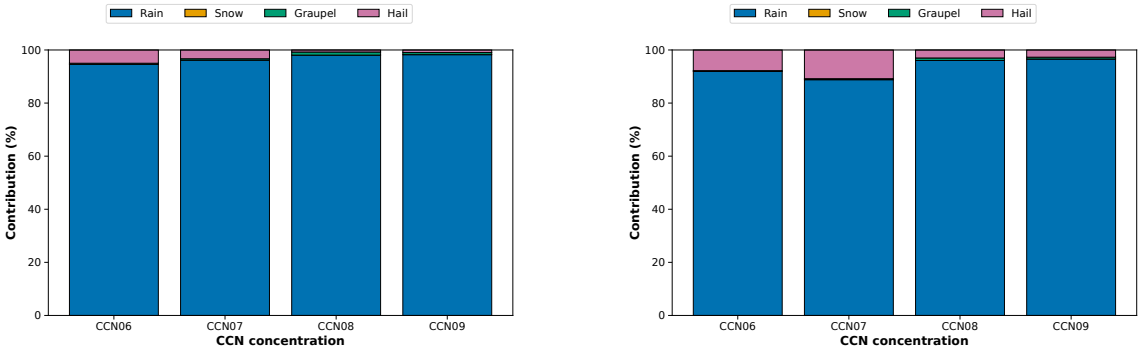

Figure 6.2: **(a)**: Contribution of rain, snow, graupel and hail to the total surface precipitation at different CCN concentrations for SIP-On scenario at 1 km; **(b)**: Similar to **(a)** for 3 km scaled orography.

6.1.2 SIP impact on cloud-ice number concentration

To assess how SIP mechanisms affect ice crystal number concentration, vertical profiles of ice number concentration across CCN concentrations are analyzed in Figure **6.3**. The 1 km and 3 km orographic scalings show similar behavior, so the discussion focuses on the 1 km case.

SIP activation increases ice crystal number concentration, but this depends on temperature because SIP processes are active only within specific temperature regimes (Han et al., 2024). To isolate the direct impact of SIP on ice number concentration, Figure **6.3a** considers the ice number concentration only up to the height at which SIP processes are active (Figure **6.3b**). Figure **6.3a** shows that for higher CCN concentrations (CCN08 and CCN09), the largest differences in the number concentration of ice occur in the height range between 6 to 8.5 km. The SIP-On scenario shows up to 80% more ice than the SIP-Off scenario. Meanwhile, above the 8.5 km, the curves converge because ice is mainly formed through homogeneous nucleation at these temperatures. This behavior is not seen for lower CCN concentrations (CCN06 and CCN07), suggesting additional ice formation pathways contribute above 8.5 km in the SIP-On scenario.

Figure **6.3b** shows rime splintering process is most active between approximately 4 and 6 km altitude. However, the production rate by rime splintering is significantly lower compared to the total secondary ice production. This is because the ice-ice collision breakup process exerts the dominant influence on overall secondary ice production, particularly between 6.5 and 10 km vertical layers. Droplet shattering becomes active around 6 km vertical height, but its contribution to total SIP remains negligible compared to ice-ice collision breakup, especially at higher altitudes where temperature ranges favor the collision breakup process (Grzegorczyk et al., 2024).

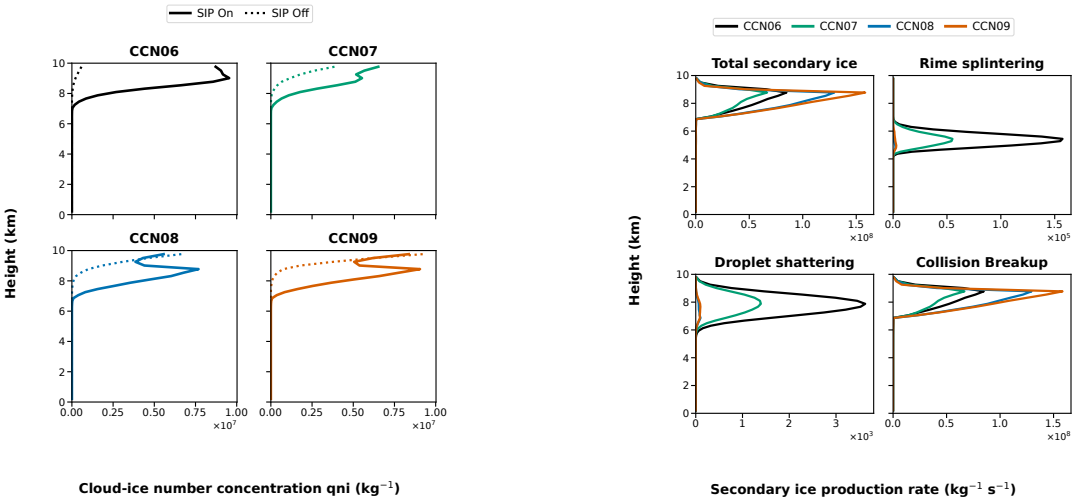

(a) (b)

Figure 6.3: **(a)**: Spatially averaged vertical profiles of cloud-ice number concentration at different CCN concentrations at 1400 UTC; **(b)**: Spatially averaged vertical profiles of cloud-ice number concentration produced from different secondary ice processes at different CCN concentrations at 1400 UTC.

6.1.3 Changes in the rainwater budget and microphysical processes

1 km scaled orography

Figure **6.4** shows that melting is the dominant source of rainwater formation across all CCN concentrations. Its contribution increases systematically with CCN concentration, ranging from about 60% at CCN06 to roughly 85% at CCN09. Accretion is the second largest source, but its contribution varies less systematically with increasing CCN concentrations. It is about 25% at CCN06, increases slightly to 30% at CCN07, then decreases to around 10% at CCN08 and 15% at CCN09. For sink processes, riming dominates at low CCN concentrations (CCN06 and CCN07), contributing about 70%, followed by evaporation at roughly 25%. Conversely, at high CCN concentrations (CCN08 and CCN09), this pattern is inverted, with evaporation becoming the dominant sink process at about 70%, while riming contributes around 25%. Rain freezing remains the smallest sink process across all CCN concentrations.

Comparing the rainwater budget of the SIP-On scenario (Figure **6.4**) with the SIP-Off scenario (Figure **5.4a**) shows that the total budget in the SIP-On scenario is substantially larger, especially at low CCN concentrations (both source and sink processes). The budget increases by about 300% at both CCN06 and CCN07, indicating enhanced rainwater production when SIP processes are active. In addition, the fractional contribution from melting increases strongly. At CCN06, it rises from about 15% in the SIP-Off scenario to about 60% in the SIP-On scenario. At CCN07, it increases from about 20% to about 50%. This shift reduces the accretion contribution from about 70% to about 30% at CCN06 and CCN07, while autoconversion remains the smallest source. For sink terms, riming increases in absolute magnitude in the SIP-On scenario at CCN06 and CCN07, but its fractional contribution stays near 60% for both CCN concentrations. Evaporation increases

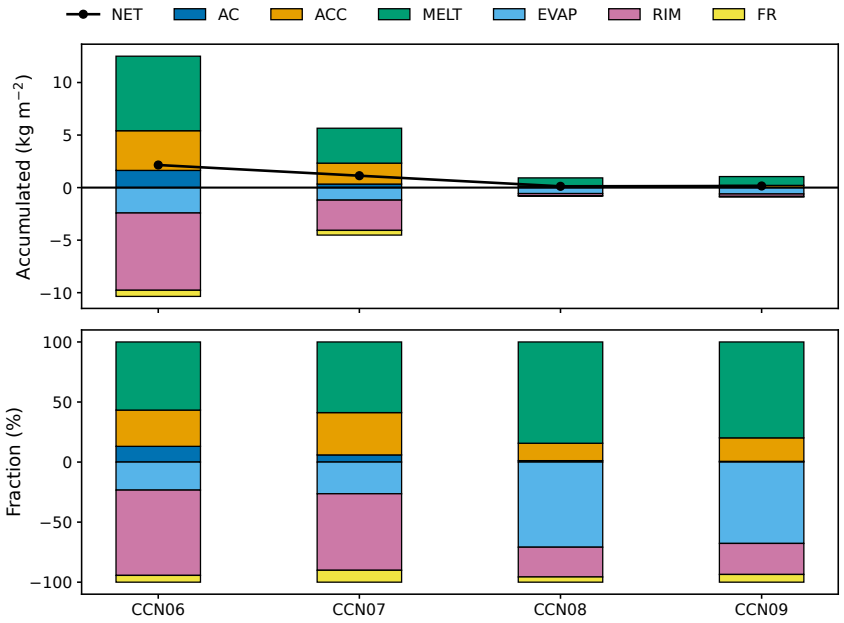

Figure 6.4: Vertically integrated and time-accumulated (24 h) rain water budget for 1 km scaled orography for SIP-On scenario.

slightly by about 10% at both CCN06 and CCN07. Rain freezing contribution decreases from 20% to 10% at CCN06 and from 25% to around 15% at CCN07. At high CCN concentration (CCN08 and CCN09), neither the absolute budget nor the fractional partitioning shows substantial changes between the SIP-On scenario and the SIP-Off scenario.

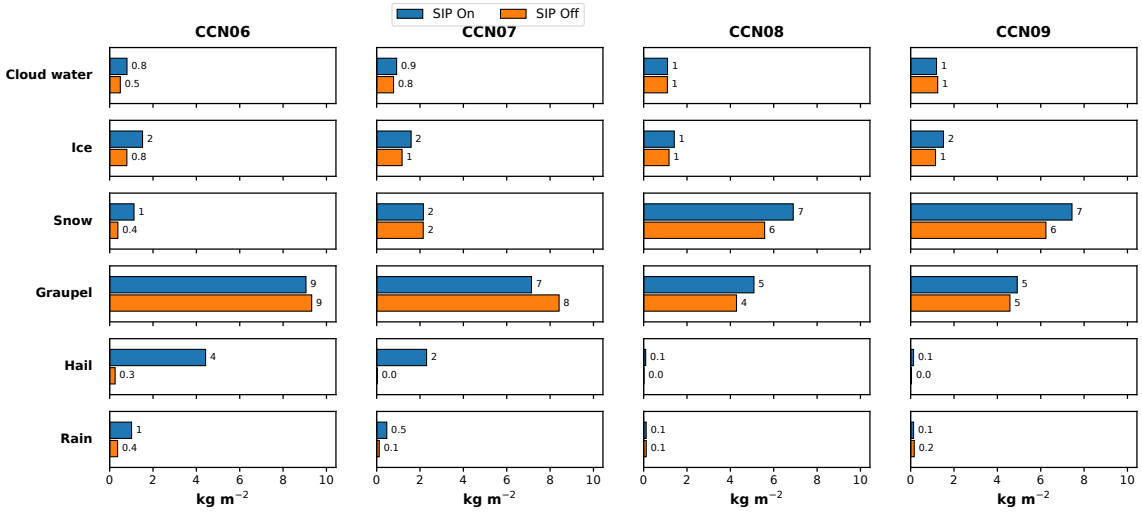

Figure 6.5: Comparing the spatially averaged and time accumulated values of total column-integrated variables (cloud water, rain, ice, snow, graupel, hail) for 1 km scaled orography between SIP-On and SIP-Off scenarios.

Figure **6.5** show the change in the total column integrated hydrometeor content for the SIP-On scenario relative to the SIP-Off scenario. For frozen hydrometeors, ice, snow and hail increase systematically in the SIP-On scenario across all CCN concentrations, whereas graupel remains relatively constant. Ice content increases by about 100% across all CCN concentrations, except for

CCN08, where it increases marginally. Snow increases by about 100% at CCN06, but the increase is smaller at CCN07 to CCN09 (ranging from 10% to 15%). Hail shows the strongest relative change, increasing by roughly a factor of 15 at CCN06 and CCN07 and by about a factor of 10 at CCN08 and CCN09. However, the absolute magnitudes of hail remain much smaller at CCN08 and CCN09 than at CCN06 and CCN07. To explain these column-integrated changes under SIP activation, the microphysical process rates are analysed next.

Figure **6.6a** shows that at low CCN concentrations (CCN06 and CCN07), cold-rain processes increase significantly in the SIP-On scenario relative to the SIP-Off scenario. Total riming increases by about a factor of 3.5, while rain production by melting increases by roughly a factor of 10. Accretion and autoconversion also increase in the SIP-On scenario, but their changes are small compared to the riming process. This indicates that the SIP-On scenario accumulates more frozen mass in the supercooled layers through riming, which is subsequently fed to the melting layer. Consequently, this leads to an increase in surface precipitation, even when accounting for evaporation. At higher CCN concentrations, total riming decreases considerably, and the differences between the SIP-On and SIP-Off scenarios largely vanish. Although collection processes strengthen at high CCN concentrations, the frozen mass produced is similar in both scenarios. This results in almost equal mass reaching the melting layer and subsequently the evaporation layers. This suggests that the enhancement of cold-rain processes by SIP processes is more pronounced under conditions of low CCN concentrations.

Further investigation into the microphysical processes, shown in Figure **6.6b**, shows that the riming increase at low CCN concentration (CCN06 and CCN07) mainly arises from enhanced riming of cloud droplets and raindrops with hail. Both terms increase by at least a factor of 10 in the SIP-On scenario, producing much larger hail content than in the SIP-Off scenario (Figure **6.5**). At high CCN concentrations, where cloud droplets are small and rain content is low, riming becomes inefficient. Additionally, the collection of other hydrometeors by hail remains weak (not shown in Figure **6.6b**). Consequently, the hail content does not show significant values at high CCN concentrations. In contrast, graupel riming with cloud droplets and raindrops shows no clear enhancement trend in the SIP-On scenario at CCN06 and CCN07 and is, in fact, slightly higher in the SIP-Off scenario. Thus, there is no significant difference in the graupel content between the SIP-On and Off scenarios at lower CCN concentrations. This implies that hail significantly contributes to the overall riming process under SIP-On conditions at lower CCN concentrations, thereby influencing the subsequent melting and surface precipitation rates. At high CCN concentration (CCN08 and CCN09), frozen mass growth is dominated by collection of snow by graupel. Because this process is snow-limited, the SIP-On enhancement of snow (Figure **6.5**) via increased ice-ice aggregation is proportionally reflected in the increase of snow collection by the graupel. However, the resulting SIP-On versus SIP-Off difference in total collection remains small compared with the low CCN concentrations (CCN06 and CCN07) riming differences.

Hail embryos can form directly from freezing rain or through riming on graupel particles (Barrett and Hoose, 2023). In ICON, riming on graupel particles contributes to graupel growth rather than forming hail embryos, making it an inaccurate measure of hail formation through this pathway. In contrast, rain freezing into hail increases by more than a factor of 10 in the SIP-On scenario

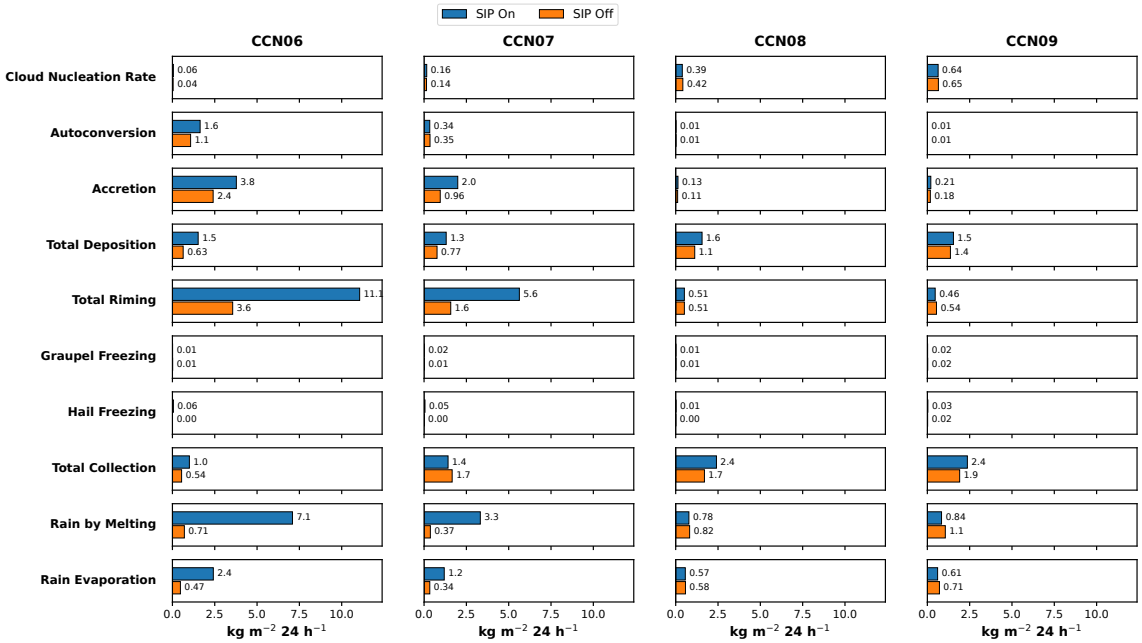

(a)

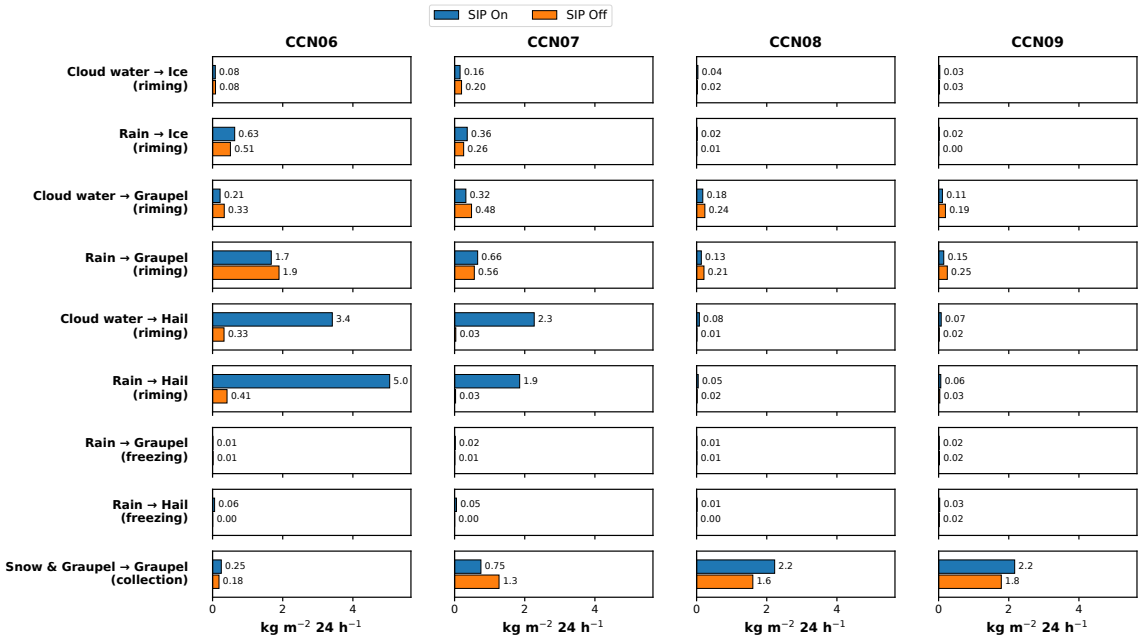

(b)

Figure 6.6: Vertically integrated and time-accumulated microphysical processes' rates comparison between SIP-On and SIP-Off scenario at 1 km scaled orography for **(a)**: all major processes, **(b)**: significant sub-processes that are parts of the major processes shown in **(a)**.

relative to the SIP-Off scenario (Figure **6.6b**), producing more initial hail embryo mass at low CCN concentration in the SIP-On scenario.

Since hail is larger in size than graupel, it exhibits greater collection efficiency. Thus supercooled liquid is collected more efficiently by hail than by graupel. Since riming is also limited by the availability of supercooled liquid water, enhanced hail riming can deplete supercooled liquid water and reduce its availability for graupel. This is evident in the vertical profiles of hail and graupel

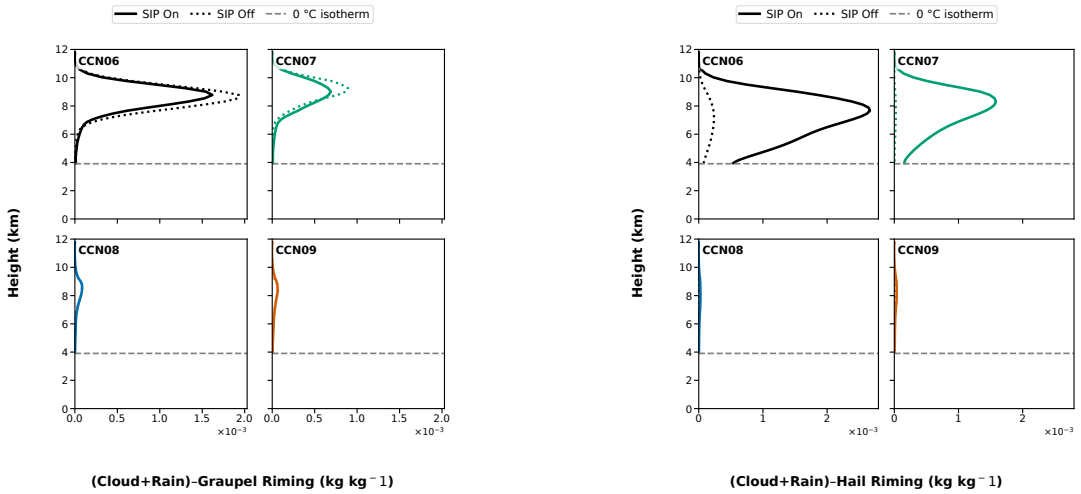

(a) (b)

Figure 6.7: Spatially averaged and time accumulated (1100 UTC - 1700 UTC) vertical profiles for SIP-On and SIP-Off scenarios at 1 km scaled orography for **(a)**: Graupel riming with supercooled liquid water (cloud + rain); **(b)**: Hail riming with supercooled liquid water

riming with supercooled liquid water (Figures **6.7a** and **6.7b**). For CCN06 and CCN07, hail riming increases substantially in the SIP-On scenario within the same mixed-phase layers (6–8 km) where graupel riming is active. This indicates preferential collection of supercooled liquid water by hail in the SIP-On scenario, which effectively reduces the amount available for graupel. This competition for supercooled liquid water suggests a complex interaction where enhanced hail formation in SIP-On scenario at low CCN concentrations directly impacts the growth efficiency of other frozen hydrometeors like graupel.

Riming of ice with raindrops also increases in the SIP-On scenario at CCN06 and CCN07 (Figure **6.6b**). This directly results from the increased ice number concentration due to secondary ice production (seen in Section **6.1.2**), which further grows via deposition and collects more supercooled liquid water. At high CCN concentrations (CCN08 and CCN09), where riming is inefficient, differences in ice content between the SIP-On scenario and SIP-Off scenario are mainly driven by deposition. As a result, ice content remains higher in the SIP-On scenario across all CCN concentrations (Figure **6.5**). Higher snow content in the SIP-On scenario at all CCN concentrations (Figure **6.5**) is primarily due to enhanced ice–ice aggregation and depositional growth.

3 km scaled orography

At 3 km scaled orography, the SIP–CCN concentration interaction follows the same pattern as at 1 km (although with higher magnitude). At low CCN concentration, the SIP-On scenario strongly enhances total surface precipitation and surface rain, whereas at high CCN concentration this enhancement becomes weak. This behaviour is shown in Figure **6.1**. As in the 1 km case, the enhancement at low CCN concentration is linked to stronger hail riming with cloud droplets and raindrops in the SIP-On scenario (Figure **1** in Appendix **A**), which more efficiently scavenges supercooled liquid water, increases frozen mass, and raises surface precipitation.

6.1.4 Effect of SIP on particle size distributions

Figures **5.5b** and **6.2b** show that SIP activation substantially modifies the surface precipitation contributions. At 3 km scaled orography, hail contributes up to 50% of total precipitation at low CCN concentration (CCN06) in the SIP-Off scenario (vs around 6% in the SIP-On scenario) and about 25% at CCN07 (vs around 10% for SIP-On scenario). A similar trend occurs at higher CCN concentration as well, but the differences between the SIP-Off scenario and SIP-On scenario are smaller than at low CCN concentration. This indicates that in the SIP-Off scenario, average hail and graupel particle size distributions are larger and do not melt completely during descent, particularly at low CCN concentration.

These findings suggest that the SIP processes fundamentally alter the particle size distribution of the hydrometeors. The activation of SIP leads to an increased concentration of smaller ice crystals. These crystals grow by riming and vapour deposition, increasing mass at smaller diameters (Grzegorczyk et al., 2025). Thus, this higher number concentrations of smaller ice hydrometeors are more prone to melting before reaching the surface, thereby shifting the precipitation contribution towards rain for the SIP-On scenario.

To quantify this relationship, the mean vertical profiles of total water content (TWC) for the SIP-On scenario and SIP-Off scenario are compared in melted-equivalent diameter mass bins. The methodology is mentioned in Section **3.5**. TWC is converted from $\mathrm{kg\,m^{-3}}$ to $\mathrm{g\,m^{-3}}$. For the current simulation day, the analysis includes only cloud-ice, graupel and hail, as these species represent the full growth pathway from ice crystals to precipitation-sized graupel and hail particles through several microphysical processes. For brevity, only the 3 km scaled orography is shown, since the 1 km scaled orography yields similar results. The results are presented in Figure **6.8**.

At low CCN concentrations (CCN06 and CCN07), the SIP-Off scenario shows maximum mass concentrated at medium diameters (0.3–1.5 mm) in the mixed-phase layers (4.5–10 km) where SIP processes are active. TWC reaches in the range of 0.010 - 0.015 $\mathrm{g\,m^{-3}}$ at these diameter ranges. A secondary maximum occurs at larger diameters (4–8 mm) at altitudes 5–6 km, indicating accumulation of mass in the form of larger particles. However, for the SIP-On scenario, the TWC peaks at smaller diameters (0.2–0.8 mm) in the range of 0.005 - 0.008 $\mathrm{g\,m^{-3}}$. This shift from large-particle TWC concentration in SIP-Off to small-particle TWC concentration can explain the observed surface precipitation contribution differences at low CCN concentrations, since comparatively smaller particles have lower sedimentation velocities and are more prone to melting before reaching the surface.

At CCN07 and CCN08, both SIP-On and SIP-Off scenarios produce almost similar TWC distributions. Medium diameters (0.3–1.5 mm) show TWC in the range of 0.001 - 0.005 $\mathrm{g\,m^{-3}}$ in the mixed-phase layers. There is slightly higher TWC (0.00010 - 0.00020 $\mathrm{g\,m^{-3}}$) for SIP-Off at higher diameter ranges of 3–4 mm in the mixed-phase layers and slightly lower altitudes, which is less significant compared to the differences at lower CCN concentrations. This indicates that at high CCN concentrations, the SIP influence on the hydrometeor size distribution is reduced.

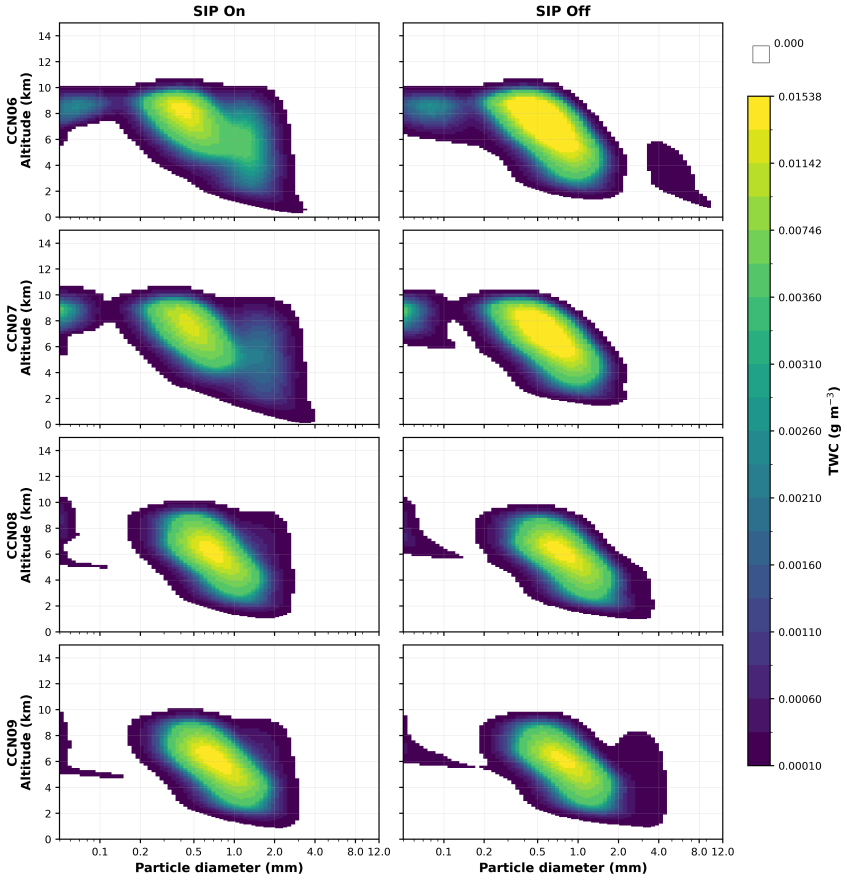

Figure 6.8: Comparison of mean total water content (TWC) as a function of altitude and melted-equivalent diameter (ice, graupel and hail only) for 3 km scaled orography.

6.2 Case II (Corsica): 04 August 2024

6.2.1 24-h total accumulated precipitation

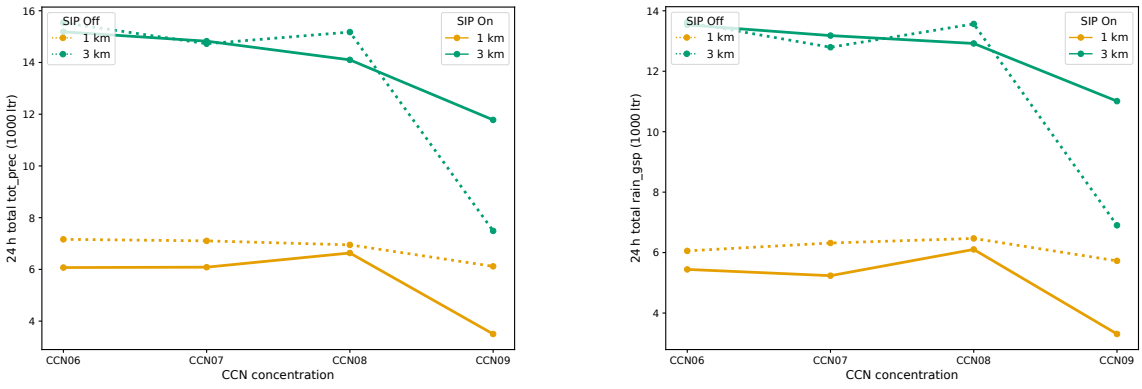

(a) (b)

Figure 6.9: **(a)**: Variation of 24 h total accumulated surface precipitation (including rain, snow, graupel and hail) and with different CCN concentrations at 1 km and 3 km scaled orography for SIP On and SIP Off scenarios; **(b)**: Same as **(a)**, but for total accumulated surface rain only

Unlike 27 August 2024, when SIP activation strongly modulates precipitation at low CCN concentration (CCN06 and CCN07), the 04 August 2024 case shows a different response. Figure **6.9** shows that total surface precipitation and surface rain respond non-linearly to SIP activation across CCN concentrations and orography scaling. At 1 km scaled orography, total surface precipitation and surface rain are lower in the SIP-On scenario than in the SIP-Off scenario at all CCN concentrations. At 3 km scaled orography, the pattern is more complex and non-linear, with almost no or very low difference at low CCN concentrations (CCN06 and CCN07). At CCN08, SIP-Off exhibits a slightly higher total surface precipitation and rain (around 7%) and at CCN09, SIP-On exhibits substantially higher total surface precipitation and rain compared to SIP-Off (around 50%). This indicates that, for 04 August 2024, SIP activation modifies precipitation formation through different microphysical pathways than in the 27 August 2024 case.

6.2.2 SIP impact on cloud-ice number concentration

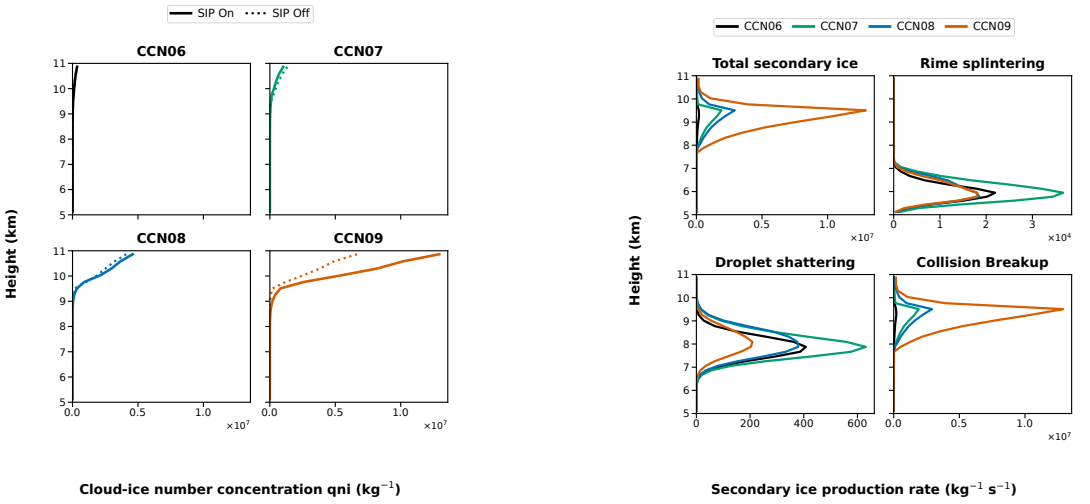

(a) (b)

Figure 6.10: **(a)**: Spatially averaged vertical profile of cloud-ice number concentration at different CCN concentrations at 1400 UTC; **(b)**: Spatially averaged vertical profiles of cloud-ice production rates from different secondary ice processes at different CCN concentrations at 1400 UTC.

Figure **6.10** shows how secondary ice processes (Figure **6.10b**) affect ice crystal number concentration across CCN concentrations (Figure **6.10a**). Only 5–11 km is shown because neither ice nor SIP processes occur below 5 km. Similar to the case of 27 August 2024, only 1 km scaled orography is presented because the 3 km scaling shows the same trends.

A key difference from 27 August 2024 case is the magnitude of the SIP-induced enhancement. Here, the increase in cloud-ice number concentration is negligible for CCN06 to CCN08, in contrast to the upto 80% differences previously observed for 27 August 2024 case. Only CCN09 shows a clear effect, with the SIP-On scenario reaching up to 100% higher ice number concentration than the SIP-Off scenario. Consistent with this, cloud-ice production rates are up to an order of magnitude lower than in the 27 August 2024 case for the SIP-On scenario for CCN06 to CCN08.

The same difference is observed for the SIP-Off scenario as well. This indicates a fundamental difference in the microphysical pathways dominating the two case studies.

The relative behavior of SIP mechanisms is similar to the previous case where rime splintering peaks between 5 and 6.5 km. Ice-Ice collision breakup is the most dominant SIP mechanism and is active at higher altitudes (8–11 km). Droplet shattering activates near 6 km, but its contribution to total SIP remains negligible compared to ice-ice collision breakup, especially at colder temperatures.

6.2.3 Changes in the rainwater budget and microphysical processes

1 km scaled orography

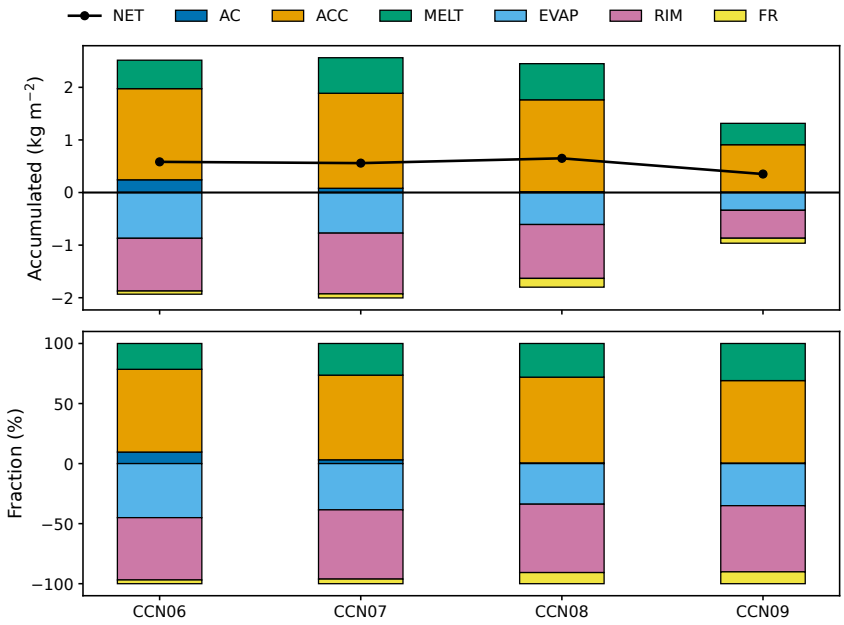

Figure 6.11: Vertically integrated and time-accumulated (24 h) rain water budget for 1 km scaled orography for SIP-On scenario.

For this simulation case, SIP activation does not substantially modify the rainwater budget. Figure **6.11** shows the 1 km rainwater budget for the SIP-On scenario. Similar to the SIP-Off scenario (Figure **5.9a**), accretion dominates the rainwater production across all CCN concentrations (around 70%). Melting increases only slightly with CCN concentrations (25% at CCN06 to 30% at CCN09), while autoconversion remains a minor contributor. For the sink processes, evaporation and riming contribute almost equally at CCN06 and CCN07 (around 45%). At CCN08 and CCN09, riming (around 40%) is marginally higher than evaporation (around 35%). Rain freezing increases from 5% at CCN06 to about 10% at CCN09, but remains the lowest contributor.

To further explain this, a more detailed analysis of the microphysical processes is performed. Figure **6.12** indicates that cold-rain processes of riming, collection and melting are weaker than on 27 August 2024 and show no clear systematic SIP-On scenario versus SIP-Off scenario differences across CCN concentrations. Accretion remains dominant, but the accumulated accretion mass is

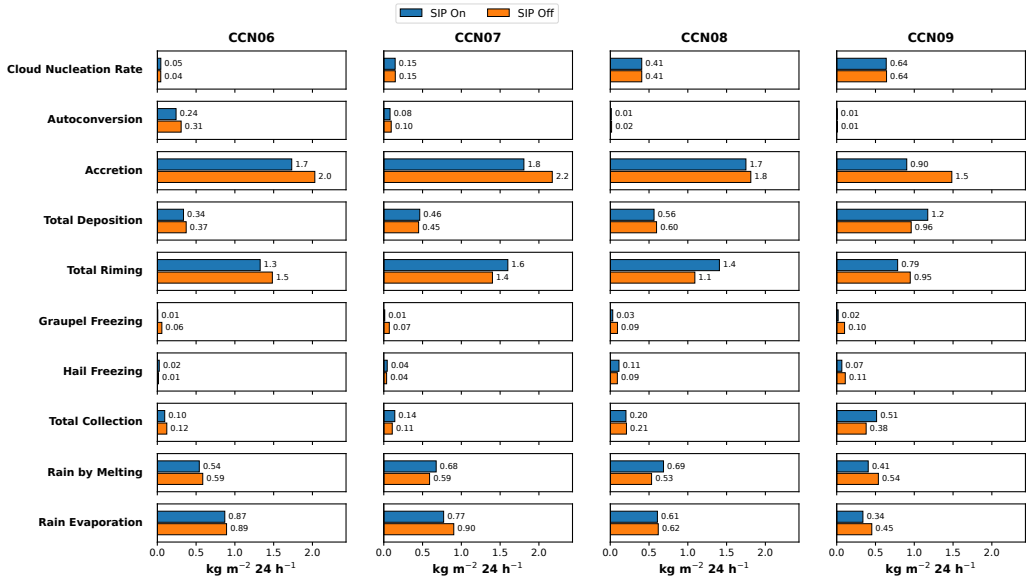

Figure 6.12: Vertically integrated and time-accumulated microphysical processes' rates comparison between SIP-On and SIP-Off scenarios at 1 km scaled orography for all major processes.

systematically lower in the SIP-On scenario than in the SIP-Off scenario at each CCN concentration. This is linked to a reduced liquid water content (LWC) in the layers where accretion is active. Figure **6.13** shows that the vertically integrated LWC for the SIP-On scenario is systematically lower than the SIP-Off scenario. At CCN06, it is lower by around 6%, followed by 17% at CCN07, 8% at CCN08 and by around 12% at CCN09. These LWC reductions for the SIP-On scenario at respective CCN concentrations are proportionately reflected in the total accretion rates (Figure **6.12**). Thus, this reduction in accretion, when accounted for evaporation, yields lower surface precipitation for the SIP-On scenario, across all CCN concentrations (Figure **6.9a**).

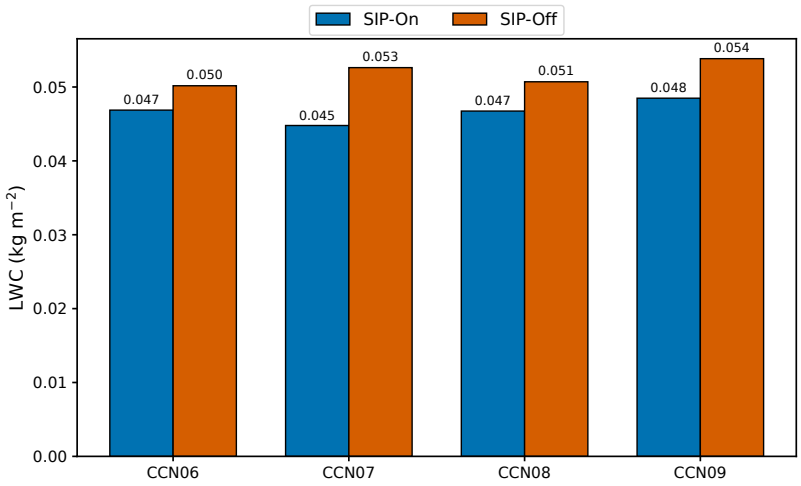

Figure 6.13: Spatially averaged, vertically integrated and time-accumulated (1100 UTC - 1700 UTC) liquid water content (LWC) comparsion between the SIP-Off and SIP-On scenarios at 1 km scaled orography.

3 km scaled orography

The 3 km scaled orography exhibits similar microphysical behavior to the 1 km case, with activation of SIPs producing no substantial change in the dominant precipitation formation pathways. Accretion remains the primary rainwater production mechanism (Figure **2** in Appendix **A**) in the lower warm-phase layers, again suppressing cold-rain process intensification due to limited SLWC availability. However, the difference in the accretion rate between SIP-on and SIP-off scenarios for 3 km scaled orography is less systematic compared to the 1 km case across all CCN concentrations. Due to this, the ultimate impact on surface precipitation also exhibits a less consistent pattern as shown in Figure **6.9**.

6.3 Comparison between the Corsica deep convective cases

The contrasting behaviors observed between the two Corsica deep convective cases indicate that activating SIP mechanisms does not necessarily enhance cold-rain microphysical processes and increase surface precipitation, highlighting the critical role of other factors. This section therefore examines why SIP activation does not amplify cold-rain processes on 04 August 2024, in contrast to 27 August 2024. Since both 1 and 3 km show similar trends, only the 1 km scaled orography is discussed.

Relative to 27 August 2024 case, the weaker impact of SIP activation on cold-rain processes for 04 August 2024 case could be attributed to the deeper warm-phase layer (around 5 km) which allows more LWC to be consumed by accretion in the warm-phase layers. The vertical profiles of LWC and accretion process for the case of 04 August 2024 for SIP-On scenario are shown in Figure **6.14**. The peak accretion rates in Figure **6.14b** and maximum LWC in Figure **6.14a** occur at similar altitudes in the warm-phase layers for each CCN concentration for the SIP-On scenario as well. This is in contrast with the situation observed in the 27 August 2024 case, where the warm phase layers are comparatively shallower (slightly below 4 km) and the peak accretion rates occur vertically higher in the mixed-phase region (Figure **6.14c**, **6.14d**).

Thus, this efficient conversion of cloud water to rain through accretion in lower warm-phase layers for the simulation case of 04 August 2024 leaves minimal SLWC available in the mixed-phase layers (6-10 km) where SIP mechanisms are active. Consequently, the reduced availability of SLWC significantly limits the efficiency of the riming process which is relatively more active at lower CCN concentrations. This can be seen from Figure **6.15**, where the vertically integrated SLWC in the mixed-phase layers for the 04 August 2024 simulation day is lower by at least a factor of two at lower CCN concentrations (CCN06 and CCN07), compared to the simulation case of 27 August 2024. At higher CCN concentrations, while SLWC becomes slightly less deficient (CCN08) or even exceed (CCN09) than the case of 27 August 2024, the efficiency for riming declines substantially due to the smaller size of cloud droplets. This reduces the collision kernel.

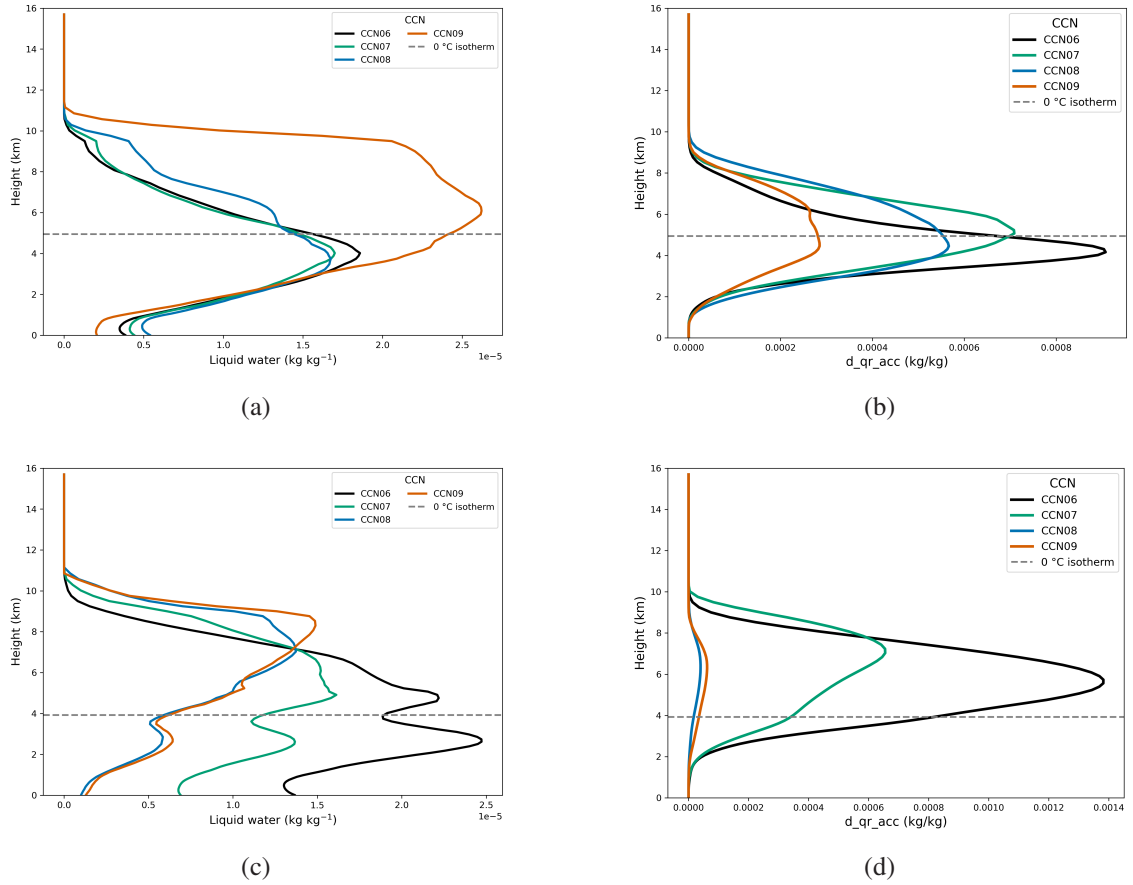

Figure 6.14: Spatiotemporal averages over the Corsica island domain (1100 UTC - 1700 UTC) for the SIP-On scenario for 04 August 2024 simulation case for the vertical profiles of: **(a)**: LWC - combined rain and cloud water, **(b)**: accretion process, **(c)**: similar to **(a)**, but for 27 August 2024, **(d)**: similar to **(b)**, but for 27 August 2024

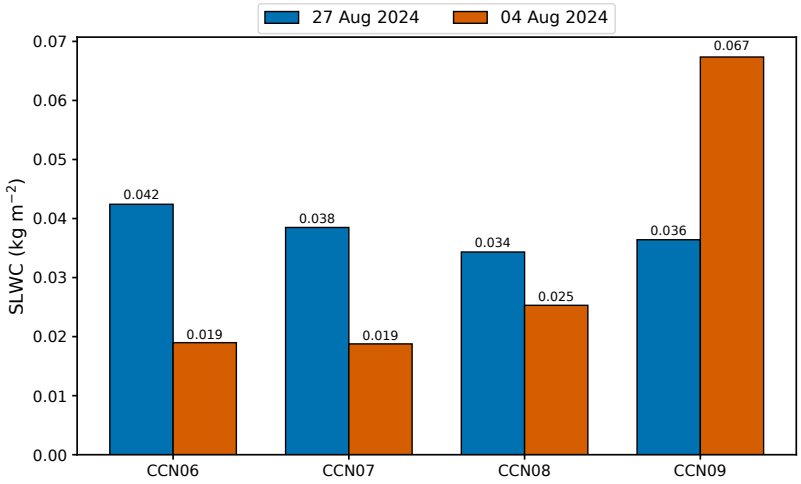

Figure 6.15: Spatially averaged, vertically integrated and time-accumulated (1100 UTC - 1700 UTC) supercooled liquid water content (SLWC) comparsion between the simulation cases of 27 August 2024 and 04 August 2024 at 1 km scaled orography for the SIP-On scenario.

Detailed microphysical processes diagnostics for 04 August 2024 (Figure **2** in Appendix **A**) indicate minor enhancements in some cold-rain processes such as riming of rain with ice and riming

of cloud water with hail for the SIP-On scenario as compared to the SIP-Off scenario across all CCN concentrations. However, this enhancement does not translate into a significant increase in surface precipitation because the further growth is constrained by the limited availability of SLWC. For example, cloud water-to-hail riming increased from 0.09 kg m^{-2} 24 h^{-1} (SIP-Off) to 0.22 kg m^{-2} 24 h^{-1} (SIP-On) at CCN06. The same process increased from 0.33 kg m^{-2} 24 h^{-1} to 3.4 kg m^{-2} 24 h^{-1} for 27 August 2024 (Figure **6.6b**). Consequently, even though the SIP mechanisms enhance some of the riming processes in the case of 04 August 2024 by efficiently collecting the limited available SLWC, the absolute mass accumulated through riming remains insufficient to substantially impact surface precipitation. This is particularly valid at low CCN concentrations, where riming processes can be directly augmented by an increased presence of SLWC within the mixed-phase regions.

This suggests that the overall impact of the SIP activation on surface precipitation critically depends upon the dominant microphysical pathways (warm-rain or cold-rain) responsible for the precipitation formation.

6.4 Case III (Iceland): 07 May 2023

6.4.1 24-h total accumulated precipitation

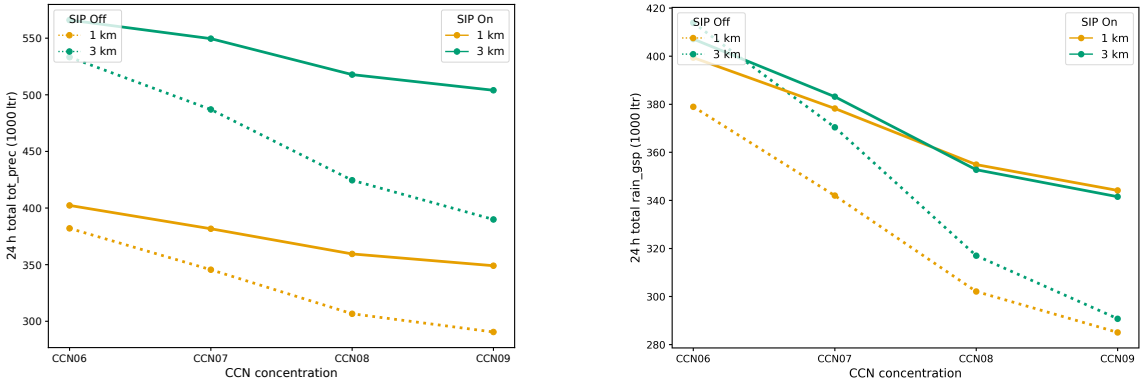

(a) (b)

Figure 6.16: **(a)**: Variation of 24 h total accumulated surface precipitation (including rain, snow, graupel and hail) and with different CCN concentrations at 1 km and 3 km scaled orography for SIP On and SIP Off scenarios; **(b)**: Same as **(a)**, but for total accumulated surface rain only

SIP activation in the Iceland stratiform environment case produces a systematic increase in total accumulated surface precipitation for both 1 km and 3 km scaled orography across all CCN concentrations (Figure **6.16a**). For 1 km scaled orography, total surface precipitation increases by around 5% at CCN06, 12% at CCN07, 16% at CCN08 and 25% at CCN09 for the SIP-On scenario relative to SIP-Off. For 3 km scaled orography, the enhancement is slightly more pronounced, ranging from around 10% at CCN06 to 30% at CCN09, indicating that SIP-On versus SIP-Off total surface precipitation differences strengthen with increasing CCN concentration and orographic scaling.

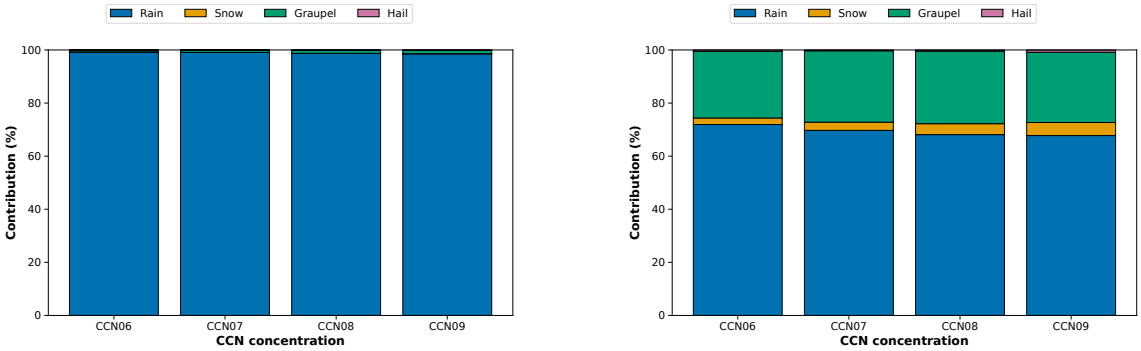

Figure 6.17: **(a)**: Contribution of rain, snow, graupel and hail to the total surface precipitation at different CCN concentrations for SIP-On scenario at 1 km; **(b)**: Similar to **(a)** for 3 km scaled orography.

The same systematic behavior is not seen for total accumulated surface rain (Figure **6.16b**). At 1 km scaled orography, surface rain remains similar to total surface precipitation for both the SIP-On scenario and SIP-Off scenario across all CCN concentrations. However, for the 3 km scaled orography, a noticeable divergence emerges at all CCN concentrations for both SIP-On and SIP-Off scenarios, indicating larger contributions from snow, graupel and hail. As already observed in Figure **5.15b** of Section **5.3.1** where SIP mechanisms are inactive, snow and graupel contribute more significantly to the surface precipitation in the 3 km scaled orography case than in the 1 km scaled orography case. A similar trend is also observed in the current SIP-On scenario, where the contributions of the other frozen hydrometeors (snow, graupel and hail) to total precipitation increases when the orography is scaled to 3 km (Figure **6.17**). At 1 km, total surface precipitation is dominated by rain (Figure **6.17a**), whereas at 3 km, snow and graupel contributions increase across all CCN concentrations (Figure **6.17b**). Graupel contributes around 20% across all CCN concentrations, while the snow increases systematically from 2% at CCN06 to around 7% at CCN09. This shows that large size hydrometeros are reaching the surface under the enhanced orographic forcing. Unlike Corsica deep convective case of 27 August 2024 where the precipitation contributions show more sensitivity with the change of the SIP scenario and CCN concentrations, the Iceland stratiform case is primarily controlled by orographic scaling. This indicates that the size distribution in Iceland stratiform environment is more influenced by orographic scaling than by the activation of SIP or CCN concentration.

6.4.2 SIP impact on cloud-ice number concentration

Figure **6.18** shows the effect of different SIP processes (Figure **6.18b**) on the ice crystals number concentrations at different CCN concentrations (Figure **6.18a**). Similar to the Corsica deep convective simulation case of 27 August 2024, the SIP activation significantly elevate the ice crystal number concentrations across all CCN concentrations at height levels where dominant SIP mechanism (collision breakup) is active. However, the quantitative effect of SIP activation on ice-crystal number concentration is multiple orders of magnitude higher in the present case than in the Corsica case. Ice-crystal number concentration is enhanced up to by factor of 10 by SIP

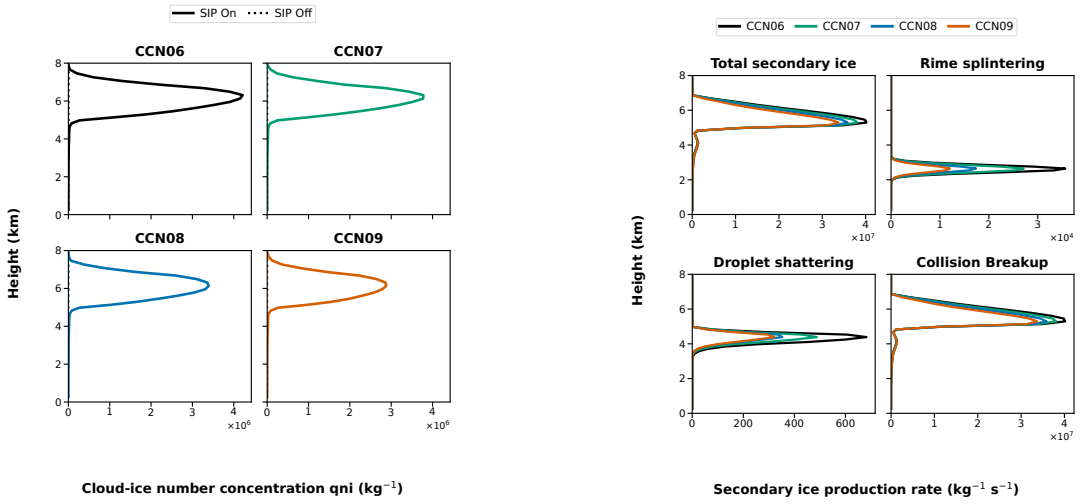

(a) (b)

Figure 6.18: **(a)**: Spatially averaged vertical profile of cloud-ice number concentration at different CCN concentrations at 1400 UTC; **(b)**: Spatially averaged vertical profiles of cloud-ice production rates from different secondary ice processes at different CCN concentrations at 1400 UTC.

activation across all CCN concentrations (due to this, the SIP-Off curves are not visible in Figure **6.18a**, as they are several orders of magnitude smaller).

This substantial increase in ice crystal number concentration is primarily attributed to the collision-breakup process, which is active in the mixed-phase height range of 5-7 km (Figure **6.18b**). This is similar to the Corsica deep convective case, however the vertical location of this mechanism differ due to the difference in the cloud type. The rime-splintering is active in the lower and narrow vertical range of 2-3 km. The droplet shattering active zone (3 - 7 km) overlaps slightly with the collision breakup. However, its contribution to the total ice crystal number concentration is significantly less compared to collision-breakup.

6.4.3 Changes in the rainwater budget and microphysical processes

1 km scaled orography

Figure **6.19** compares rainwater-budget components for the SIP-On scenario and SIP-Off scenario at 1 km scaled orography across all CCN concentrations. Rainwater production by melting increases systematically in the SIP-On scenario relative to the SIP-Off scenario for all CCN concentrations. In absolute terms, mass accumulated by melting increases by about $35-37\%$ across all CCN concentrations. This is also reflected in the fractional contributions. Melting increases from 50% (SIP-Off) to 60% (SIP-On) at CCN06, from 60% to 70% at CCN07, from around 70% to 75% at CCN08, and from 75% to 85% at CCN09. Accretion remains the second-largest rain source in both SIP scenarios across all CCN concentrations. Although its absolute values vary non-systematically between the SIP-On scenario and SIP-Off scenario, its fractional contribution decreases systematically in the SIP-On scenario as compared to the SIP-Off scenario across all

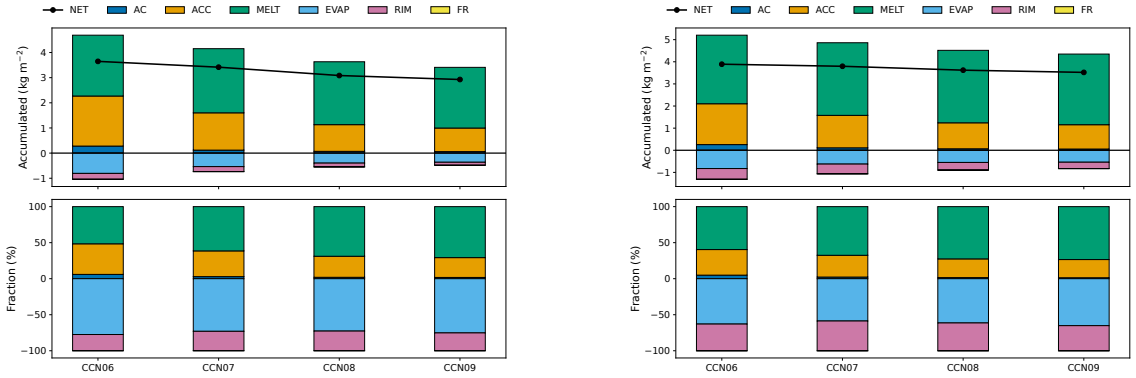

(a) (b)

Figure 6.19: Comparison of vertically integrated and time-accumulated (24 h) rain water budget between SIP-Off **(a)** and SIP-On **(b)** scenarios for 1 km scaled orography

CCN concentrations as melting becomes more dominant. Autoconversion remains the smallest contributor in both SIP scenarios, with similar contributions across all CCN concentrations (around 7% at CCN06 to around 2% at CCN09).

For sink terms, evaporation is the dominant sink in both SIP scenarios across all CCN concentrations, but its fractional contribution decreases in the SIP-On scenario (around 55%) relative to the SIP-Off scenario (around 75%). This is because of the increased contribution of the riming process, which shows systematic increases in the SIP-On scenario (around 45%) compared to the SIP-Off scenario (around 25%) across all CCN concentrations. Rain freezing shows no contribution in either SIP scenario at any CCN concentration.

Overall, the rainwater budget indicates a shift in microphysical pathways where enhanced ice-crystal production through SIP processes strengthens cold-rain processes, particularly riming and melting. To explain these changes, a more detailed analysis of the microphysical process rates is performed.

Figure **6.20** compares vertically integrated, time-accumulated microphysical process rates between the SIP-On scenario and SIP-Off scenario across all CCN concentrations. As shown Figure **6.20a**, deposition, riming, collection, melting and evaporation show a systematic increase with the activation of the SIP across all CCN concentrations. The extra ice fragments created by SIP activation start to grow immediately through vapor deposition. This increased ice mass grows further by colliding with the other ice-crystals to form snow and subsequently grow further by deposing more vapor and collecting ice-crystals. This leads to the enhanced total deposition and collection processes in the SIP-On scenario relative to the SIP-Off scenario.

Thus, total deposition is higher at all CCN concentrations in the SIP-On scenario compared to the SIP-Off scenario and the relative enhancement increases from +33% at CCN06 to +38% at CCN09. Figure **6.20b** shows that this increase is mainly driven by enhanced deposition on snow (increases by about 100% across all CCN concentrations). Deposition on ice increases marginally in the SIP-On scenario when compared to the SIP-Off scenario across all CCN concentrations (around 25% across all CCN concentrations). However, deposition on ice remains the major contributor to

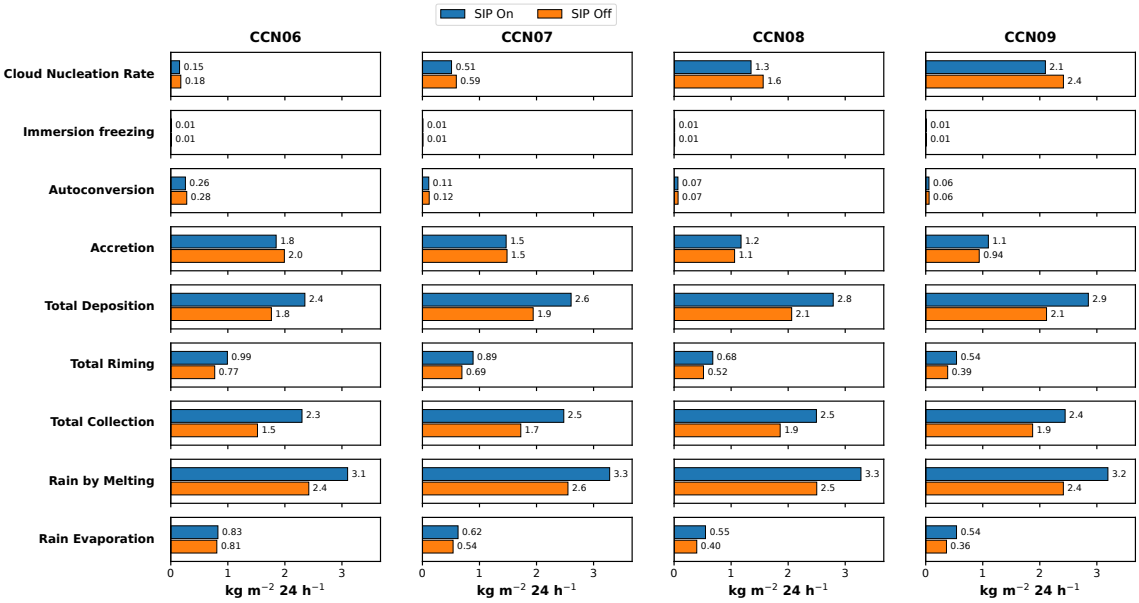

(a)

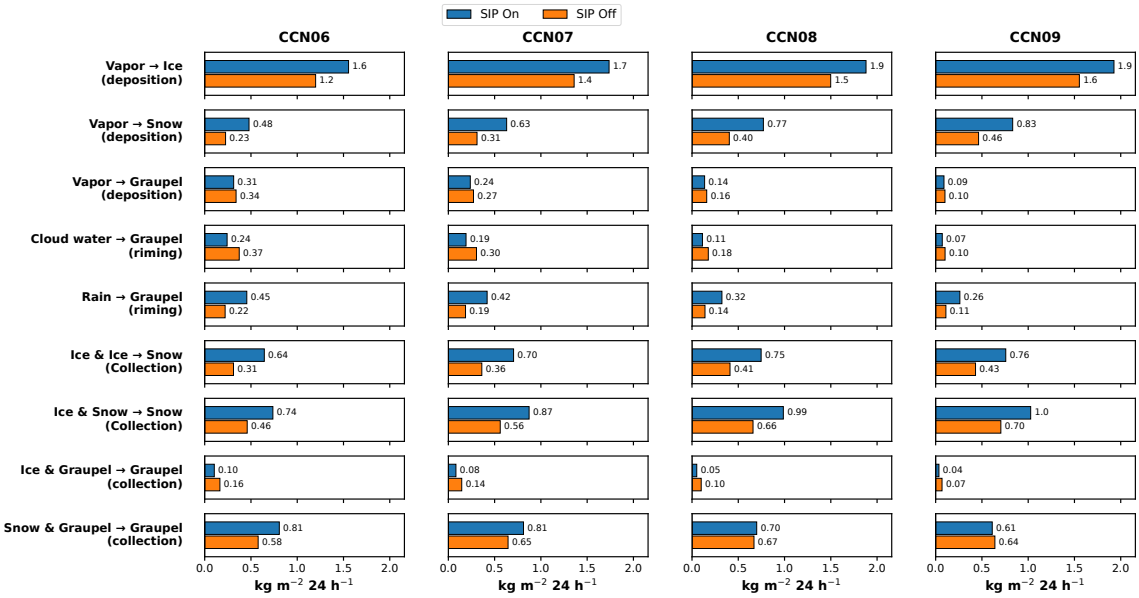

(b)

Figure 6.20: Vertically integrated and time-accumulated microphysical processes' rates comparison between SIP-On and SIP-Off scenarios at 1 km scaled orography for **(a)**: all major processes, **(b)**: significant sub-processes that happen under major processes in **(a)**.

the total deposition in both SIP scenarios (around 70% across all CCN concentrations). Deposition on the graupel particles shows insignificant differences between the two scenarios across all CCN concentrations. This shows the dominant role of snow and ice in the overall deposition process under SIP-on scenario.

Regarding the total collection, the SIP-On scenario consistently exhibits higher total collection compared to the SIP-Off scenario across all CCN concentrations. This enhanced collection is primarily driven by increased collection onto ice, snow and graupel. This is shown in Figure **6.20b** where the SIP-On scenario shows a systematic increase in the ice-ice collection to snow, ice-snow

collection to snow across all CCN concentrations. However, the snow-graupel collection to graupel does not show the systematic increase in the SIP-On scenario across all CCN concentrations. It is highest at CCN06 where it increases by 20%, then decreases systematically and at CCN09, it exhibits a marginal decrease of around 5%. This is because the collection of snow by graupel exhibits an opposite trend with increasing CCN concentrations in the SIP-On scenario when compared to the SIP-Off scenario. However, this reduced collection is compensated by the increased ice-snow collection to snow and ice-ice collection to snow, leading to an overall increase in total collection rates.

Regarding riming, the SIP-On scenario consistently shows higher riming rates than the SIP-Off scenario across all CCN concentrations (Figure **6.20a**). This is primarily due to the enhanced graupel riming with rain drops which increases roughly by around more than 100% across all CCN concentrations (Figure **6.20b**). However, the riming of graupel with cloud water decreases systematically for the SIP-On scenario when compared to the SIP-Off scenario across all CCN concentrations. This reduction in graupel riming with cloud water in the SIP-On scenario is attributed to the reduced availability of the cloud water in the vertical layers where graupel riming with cloud droplets occurs. This is shown in Figure **6.21** where the cloud water is systematically lower in the vertical layers between 2 - 5 km (Figure **6.21a**) for the SIP-On scenario across all CCN concentrations and the riming of graupel with the cloud water is active in this vertical range (Figure **6.21b**).

This enhanced frozen mass generation through riming and collection processes leads to subsequent systematic increase in melting across all CCN concentrations (Figure **6.20a**). This consequently leads to greater surface precipitation in the SIP-On scenario, when accounted for the evaporation and accretion in the lowest layers.

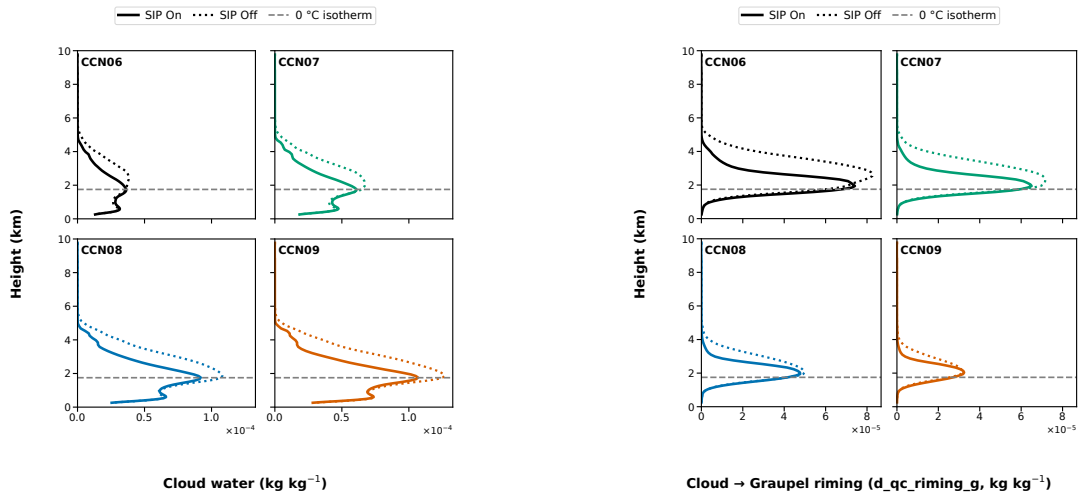

(a) (b)

Figure 6.21: Comparison of spatiotemporal averages over the Iceland island domain (1100 UTC - 1700 UTC) between SIP-On and SIP-Off scenarios for the vertical profiles of **(a)**: Cloud water content and **(b)**: riming of graupel with cloud water for 1 km scaled orography

3 km scaled orography

At 3 km scaled orography, the response is similar in terms of microphysical-process changes (Figure **3** in Appendix **A**) and total surface precipitation. Cold-rain processes, particularly deposition, riming and collection, are enhanced in the SIP-On scenario relative to the SIP-Off scenario, which increases frozen hydrometeor mass and subsequent melting. As a result, total surface precipitation increases in the SIP-On scenario, consistent with the 1 km scaled orography case. However, the magnitudes of the microphysical processes are different. Microphysical process rates of deposition, riming and collection are enhanced at 3 km than at 1 km scaled orography, indicating the impact of stronger terrain forcing on cold-rain pathways and therefore on total surface precipitation.

6.5 General Conclusions

Two days of simulations of deep convection over Corsica reveals a complex effect of SIP activation on the interplay between orography, CCN concentration and surface precipitation. For the 27 August 2024 simulation day where the cold-rain processes are active and contribute significantly to the rainwater budget, the activation of SIP leads to a significant increase in the frozen hydrometeor mass content because of the enhanced riming processes at low CCN concentrations (CCN06 and CCN07) for both 1 and 3 km scaled orography. This ultimately leads to the overall increase in the total surface precipitation. Conversely, under high CCN concentrations (CCN08 and CCN09) where riming is less dominant due to the reduction in the collision efficiency and the collection processes accumulate most of the frozen hydrometeor mass, the impact of SIP on precipitation enhancement diminishes as collection processes do not lead to an increase in frozen mass. This results in minimal changes to the total surface precipitation. This suggests a threshold effect where the microphysical pathways, particularly riming efficiency, drives the degree to which SIP can influence overall precipitation. This threshold effect is also observed in the drop size distribution, where increased number concentration of smaller ice crystals trigger riming at relative smaller particle sizes. This shifts the mass concentration towards smaller melted-equivalent diameters at lower CCN concentrations (CCN06 and CCN07) which are more prone to melting and hence leads to the enhanced contribution of rain as surface precipitation. Conversely, at higher CCN concentrations (CCN08 and CCN09), the diminished riming efficiency leads to almost similar concentration of mass across the different diameters between SIP-On and SIP-Off scenarios, resulting in less pronounced differences in contribution of rain as surface precipitation.

For the simulation case of 04 August 2024 where warm-rain processes (primarily accretion) dominate, SIP activation does not lead to the similar enhancement in surface precipitation as observed in the case of 27 August 2024 where cold-rain processes are dominant. The extra fragments created by the SIP mechanisms consume the available SLWC to grow further. However, most of the LWC is consumed in the lower warm-phase layer which is deeper in case of 04 August 2024 (5 km) as compared to the case of 27 August 2024 (below 4 km). This provides more opportunity for LWC to participate in accretion in the warm-phase layers. This leaves less SLWC available for the further growth of ice crystals by riming processes, thereby mitigating the

impact of SIP on the overall precipitation enhancement. This suggests that the effect of the SIP is dependent on the dominance of warm versus cold rain processes, thermodynamic conditions and the availability of SLWC in the mixed-phase regions where SIP processes are active.

For the Iceland simulation case, the effect of SIP activation is more systematic than in the Corsica simulation cases. This systematic effect is likely due to the different cloud structures. The total surface precipitation is enhanced across both 1 and 3 km scaled orography and CCN concentrations when SIP mechanisms are active. This indicates a more consistent role of SIP in modulating precipitation in colder environments. The extra ice fragments created by the SIP processes grow mainly via deposition and collection. Riming is less dominant in Iceland, primarily due to the reduced availability of SLWC in the higher mixed-phase cloud layers due to lower updrafts. This contrasts with Corsica, where stronger updrafts lead to greater SLWC availability in the mixed-phase layers where SIP processes are active, leading to enhanced riming processes.

7 Conclusions and outlook

This thesis examined how orography, varying CCN concentrations, and SIP jointly shape cloud microphysics and surface precipitation over the contrasting island environments of Corsica and Iceland using the convection-permitting ICON-LAM model with a grid spacing of 1 km. Three cases were analyzed: 27 August 2024 and 04 August 2024 over Corsica, and 07 May 2023 over Iceland. To assess orographic impacts on convection initiation, the terrain was scaled (flat, 1, 2, 3 and 4 km). To quantify aerosol impacts on precipitation formation, four CCN concentrations ranging from maritime to polluted continental conditions were explored. SIP was represented through three mechanisms: rime splintering, droplet shattering and collision breakup.

The analysis followed a stepwise design. First, orography was varied with CCN fixed at intermediate conditions and SIP disabled to isolate topographic effects on convective characteristics and precipitation onset. Second, CCN concentrations were varied for the 1 and 3 km orography cases only, with SIP still off, to evaluate CCN sensitivity under different terrain forcing. Finally, SIP was enabled to assess how it modifies the combined sensitivity to orography scaling and CCN loading. The following discussion evaluates these findings against the research questions.

1. How does changing the orographic scaling affect convection and rain initiation, and convective parameters under standard CCN conditions without SIP processes?

For the Corsica cases, there is a systematic response in the preconvective conditions to the systematic increase in the terrain heights. Both 2 -m temperature and specific humidity decrease with an increase in the orography scaling. Convective parameters such as CAPE, CIN, low-level wind convergence and 500 -m wind speed also show a systematic trend with the increase in the orography scaling (flat terrain to 4 km mountain tops). Similar findings have been shown by other studies such as Barthlott and Kirshbaum (2013); Demko et al. (2009); Metzger et al. (2014). However, the magnitude and the time evolution of these parameters vary between the two cases simulated here. This leads to the different convection and precipitation initiation patterns as well as different spatial precipitation patterns. Specifically, the convection developed earlier for the case of 04 August 2024 for the reference orography due to the occurrence of a relatively early low-level convergence. However, both days show the variation in precipitation around the areas where orography becomes steeper with the change in the scaling.

For the Iceland case, as opposed to the Corsica cases where there is a presence of thermal flows due to the strong solar radiation, the onset of precipitation is primarily dictated by the interaction of the prevailing synoptic flow with the island's topography. However, similar to the Corsica cases, the spatial distribution of precipitation in Iceland is significantly influenced by orography scaling. The

largest variations are around the steeper slopes and the domain-mean peak rain intensity is about 350% higher than in the Corsica domain.

How does varying CCN concentration modify cloud microphysics and surface precipitation across different orography scalings in the absence of SIP processes?

For the Iceland domain, increasing orography scaling leads to a systematic increase in total surface precipitation at each CCN concentration. This results from stronger low-level forcing that enhances condensation. This enhanced condensation effect produces more cloud water which further propagates through the relevant microphysical pathways and ultimately increases surface precipitation. Within each orography scaling, increasing CCN concentration systematically reduces total surface precipitation (around -25% from CCN06 to CCN09). In the mixed-phase layer, frozen-hydrometeor growth is dominated by collection and deposition, and both increase with increasing CCN concentrations. Whereas, the melting, accretion and evaporation in the warm-phase layers decide the final surface precipitation.

In contrast to Iceland, the two Corsica deep-convective cases do not show a consistent systematic surface-precipitation response to changing CCN concentrations. Total surface precipitation still increases systematically with increasing orography scaling at all CCN concentrations, but the magnitude of this increase differs between the two simulation days. Within a given orography scaling, the precipitation sensitivity to CCN concentration also differs between the days. This is linked to shifts in the dominant microphysical pathways controlling precipitation formation. On 27 August 2024, cold-rain processes (riming, melting and rain freezing) dominate, and melting in the warm layer below cloud base largely determines the final total surface precipitation across CCN concentrations. Previous studies such as Barthlott and Hoose (2018); Barthlott et al. (2022a,b) show a similar dominance of cold-rain processes throughout the simulations. However, for 04 August 2024, warm-rain processes play a more significant role and accretion dominates surface-precipitation production. This leads to different sensitivities to CCN concentrations across both simulation days. Thus, the precipitation response to varying CCN concentrations depends on whether warm-rain or cold-rain microphysical pathways control precipitation formation. This highlights the difference in the microphysical pathways between the two domains due to the different cloud structures.

How does activating SIP processes alter the sensitivity of cloud microphysics and surface precipitation to CCN concentration and orography scaling?

For Iceland, activating SIP consistently increases surface precipitation across all orography scalings and CCN concentrations. At 1 km scaled orography, total surface precipitation increases from 5% at CCN06 to 25% at CCN09 and at 3 km the increase ranges from around 10% at CCN06 to 30% at CCN09 compared to the simulations without SIP. This is linked to enhanced deposition and collection. SIP generates additional ice fragments that grow by vapor deposition. As they gain mass, they sediment and either collect similar-sized frozen hydrometeors or are collected by larger particles, before falling through the warm layer where accretion and evaporation act differentially and determine the final surface precipitation.

For the Corsica deep-convective cases, activating SIP produces different precipitation responses depending on the dominant precipitation formation processes. On 27 August 2024, for both 1 and 3 km scaled orography, where cold-rain processes dominate, SIP substantially increases total surface precipitation at low CCN concentration (at least by a factor of three at CCN06 and CCN07), but has little to no effect at higher CCN concentration (CCN08 and CCN09). This is partly consistent with Sun et al. (2025), where they found the strongest SIP-induced precipitation enhancement at an intermediate CCN level (400 cm^{-3}) among 200, 400, and 800 cm^{-3} for a Hector storm under weak instability. In the 27 August 2024 simulation, the enhancement at low CCN is linked to stronger riming, which increases melting and surface precipitation. At high CCN concentration, collection dominates and remains similar in SIP-on and SIP-off runs. This indicates a non-linear sensitivity to CCN concentration. In contrast, on 04 August 2024, when warm-rain processes dominate, SIP affects surface precipitation differently across orography scalings as CCN increases. The response is controlled by how warm-rain processes (mainly accretion) change when SIP is enabled. This indicates that SIP impacts depend strongly on the prevailing microphysical pathways. For 27 August 2024, SIP also modifies the average particle sizes in the mixed-phase layer. At low CCN concentrations, additional small fragments undergo riming and deposition, shifting mass toward smaller diameters. At high CCN concentrations, where riming is inefficient, the particle size distribution changes only weakly. Consistent with this, large hydrometeors (graupel and hail) contribute substantially to surface precipitation at low CCN concentrations in the SIP-Off scenario. These results are consistent with the study Grzegorczyk et al. (2025) where SIP induced a redistribution of the total water content towards smaller particle sizes. However, CCN impacts are not discussed in this study. This is in contrast to the Iceland case, where the precipitation contribution is primarily sensitive to orography scaling and only weakly to CCN concentrations.

The insights gained from this thesis provide an initial understanding of how orography, aerosol concentration, and SIP interact with each other in two contrasting cloud structures. The analysis shows that enabling SIP in the numerical model can substantially modify the dominant microphysical pathways and, consequently, surface precipitation in both cloud structures. This highlights the importance of routinely representing the SIP processes in the numerical models. Consistent with this, several recent studies showed how the inclusion of SIP processes can significantly re-balance the ice phase of the mixed-phase clouds (Costa-Surós et al., 2025; Grzegorczyk et al., 2025; Sun et al., 2025).

However, in this thesis, SIP impact differs between cold-rain and warm-rain dominated pathways for the mixed-phase deep convective clouds. Therefore, additional real-case simulations are needed to better constrain SIP-CCN interactions at different orography scaling. In addition, evaluating the sensitivity to individual SIP mechanisms will further explain their relative contributions to the overall enhancement or suppression of precipitation. Since changes in CCN concentration can shift microphysical pathways and thereby influence cloud optical properties and cloud radiative effects (CRE) (Forster et al., 2023), it is also important to assess how CRE responds to orography and CCN variations, and whether SIP modulates these radiative responses.

Appendices

A Appendix to Chapter 6

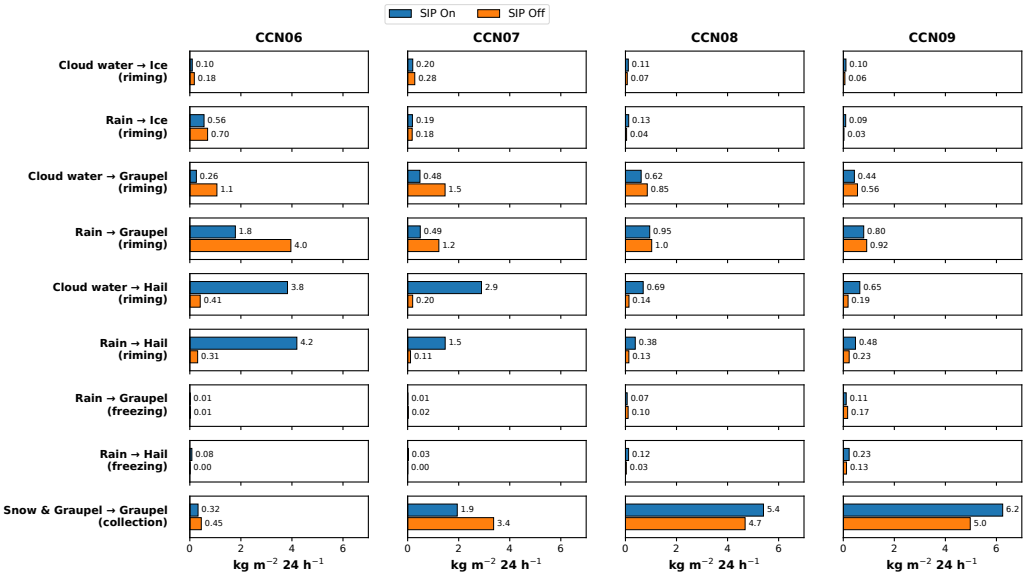

Figure 1: Vertically integrated and time-accumulated microphysical processes rates comparison between SIP-On and SIP-Off scenario for Corsica domain at 3 km scaled orography for the 27 August 2024 simulation case.

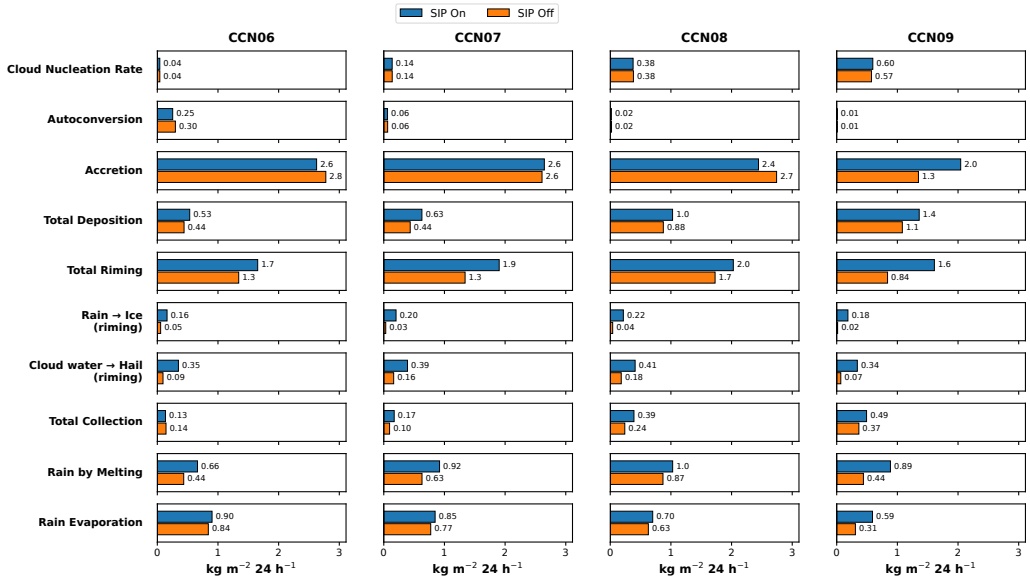

Figure 2: Vertically integrated and time-accumulated microphysical processes rates comparison between SIP-On and SIP-Off scenario for Corsica domain at 3 km scaled orography for the 04 August 2024 simulation case.

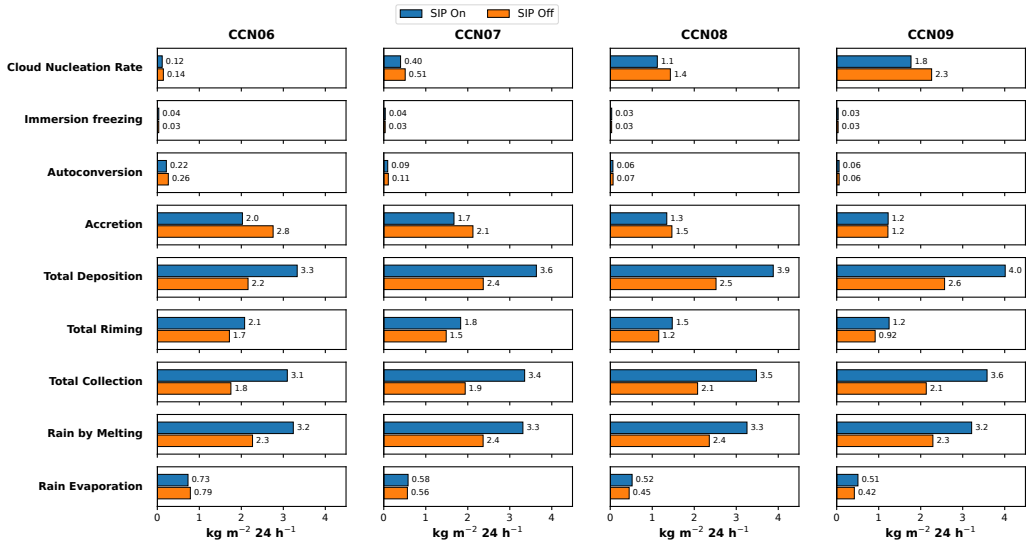

Figure 3: Vertically integrated and time-accumulated microphysical processes rates comparison between SIP-On and SIP-Off scenario for Iceland domain at 3 km scaled orography for the 07 May 2023 simulation case.

Bibliography

Adler, B., and N. Kalthoff, 2014: Multi-scale transport processes observed in the boundary layer over a mountainous island. *Boundary-Layer Meteorology*, **153 (3)**, 515–537, https://doi.org/10.1007/s10546-014-9957-8.

Altaratz, O., I. Koren, T. G. Reisin, A. B. Kostinski, G. Feingold, Z. Levin, and Y. Yin, 2008: Aerosols' influence on the interplay between condensation, evaporation and rain in warm cumulus cloud. *Atmospheric chemistry and physics*, **8 (1)**, 15–24, https://doi.org/10.5194/acp-8-15-2008, publisher: Copernicus Publications.

Altaratz, O., I. Koren, L. A. Remer, and E. Hirsch, 2014: Review: Cloud invigoration by aerosols—Coupling between microphysics and dynamics. *Atmospheric Research*, **140**, 38–60, https://doi.org/10.1016/j.atmosres.2014.01.009.

Arfin, T., A. M. Pillai, N. Mathew, A. Tirpude, R. Bang, and P. Mondal, 2023: An overview of atmospheric aerosol and their effects on human health. *Springer Nature*, **30**, https://doi.org/https://doi.org/10.1007/s11356-023-29652-w.

Austin, G. L., and K. N. Dirks, 2005: Topographic effects on precipitation. *Encyclopedia of Hydrological Sciences*, Wiley, URL https://onlinelibrary.wiley.com/doi/10.1002/0470848944.hsa033.

Banta, R. M., 1990: The role of mountain flows in making clouds. *American Meteorological Society eBooks*, American Meteorological Society, 229–283, https://doi.org/10.1007/s11356-023-29652-w.

Barrett, A. I., and C. Hoose, 2023: Microphysical Pathways Active Within Thunderstorms and Their Sensitivity to CCN Concentration and Wind Shear. *Journal of Geophysical Research Atmospheres*, **128 (5)**, https://doi.org/10.1029/2022jd036965.

Barthlott, C., and S. Davolio, 2015: Mechanisms initiating heavy precipitation over Italy during HyMeX Special Observation Period 1: a numerical case study using two mesoscale models. *Quarterly Journal of the Royal Meteorological Society*, **142**, 238–258, https://doi.org/10.1002/qj.2630.

Barthlott, C., and C. Hoose, 2018: Aerosol effects on clouds and precipitation over central europe in different weather regimes. *Journal of the Atmospheric Sciences*, **75 (12)**, 4247–4264, https://doi.org/10.1175/jas-d-18-0110.1.

Barthlott, C., and D. J. Kirshbaum, 2013: Sensitivity of deep convection to terrain forcing over Mediterranean islands. *Quarterly Journal of the Royal Meteorological Society*, **139 (676)**, 1762–1779, https://doi.org/10.1002/qj.2089.

Barthlott, C., B. Mühr, and C. Hoose, 2017: Sensitivity of the 2014 Pentecost storms over Germany to different model grids and microphysics schemes. *Quarterly Journal of the Royal Meteorological Society*, **143 (704)**, 1485–1503, https://doi.org/10.1002/qj.3019.

Barthlott, C., A. Zarboo, T. Matsunobu, and C. Keil, 2022a: Impacts of combined microphysical and land-surface uncertainties on convective clouds and precipitation in different weather regimes. *Atmospheric Chemistry and Physics*, **22 (16)**, 10 841–10 860, https://doi.org/10.5194/acp-22-10841-2022.

Barthlott, C., A. Zarboo, T. Matsunobu, and C. Keil, 2022b: Importance of aerosols and shape of the cloud droplet size distribution for convective clouds and precipitation. *Atmospheric Chemistry and Physics*, **22 (3)**, 2153–2172, https://doi.org/10.5194/acp-22-2153-2022.

Barthlott, C., R. Burton, D. J. Kirshbaum, K. Hanley, E. Richard, J. Chaboureau, J. Trentmann, B. Kern, H. Bauer, T. Schwitalla, C. Keil, Y. Seity, A. Gadian, A. Blyth, S. Mobbs, C. Flamant, and J. Handwerker, 2011: Initiation of deep convection at marginal instability in an ensemble of mesoscale models: a case-study from COPS. *Quarterly Journal of the Royal Meteorological Society*, **137**, 118–136, https://doi.org/10.1002/qj.707.

Behrendt, A., S. Pal, F. Aoshima, M. Bender, A. Blyth, U. Corsmeier, J. Cuesta, G. Dick, M. Dorninger, C. Flamant, P. D. Girolamo, T. Gorgas, Y. Huang, N. Kalthoff, S. Khodayar, H. Mannstein, K. Träumner, A. Wieser, and V. Wulfmeyer, 2011: Observation of convection initiation processes with a suite of state-of-the-art research instruments during COPS IOP 8b. *Quarterly Journal of the Royal Meteorological Society*, **137**, 81–100, https://doi.org/10.1002/qj.758.

Bolton, D., 1980: The computation of equivalent potential temperature. *Monthly Weather Review*, **108 (7)**, 1046–1053, https://doi.org/10.1175/1520-0493(1980)108<1046:tcoept>2.0.co;2.

Brownscombe, J. L., and N. S. C. Thorndike, 1968: Freezing and Shattering of Water Droplets in Free Fall. *Nature*, **220 (5168)**, 687–689, https://doi.org/10.1038/220687a0.

Bryan, G. H., and M. J. Fritsch, 2000: Moist absolute instability: The sixth static stability state. *Bulletin of the American Meteorological Society*, **81 (6)**, 1207–1230, https://doi.org/10.1175/1520-0477(2000)081<1287:MAITSS>2.3.CO;2.

Choudhury, G., B. Tyagi, J. Singh, C. Sarangi, and S. N. Tripathi, 2019: Aerosol-orography-precipitation – A critical assessment. *Atmospheric Environment*, **214**, 116 831–116 831, https://doi.org/10.1016/j.atmosenv.2019.116831.

Clapeyron, E., 1834: Mémoire sur la puissance motrice de la chaleur. *Journal de l'École polytechnique*, **14 (23)**, 153–190, URL https://gallica.bnf.fr/ark:/12148/bpt6k4336791/f157.item.

Clausius, R., 1850: Ueber die bewegende Kraft der Wärme und die Gesetze, welche sich daraus für die Wärmelehre selbst ableiten lassen. *Annalen der Physik*, **155 (4)**, 500–524, https://doi.org/10.1002/andp.18501550403.

Costa-Surós, M., M. G. Ageitos, M. Chatziparaschos, P. Georgakaki, M. A. Thomas, G. Montané, S. Myriokefalitakis, T. v. Noije, P. L. Sager, M. Kanakidou, A. Nenes, and C. P. García-Pando, 2025: Implementation of Primary and Secondary Ice Production in EC-Earth3-AerChem: Global Impacts and Insights. *EGUsphere*, **2025**, https://doi.org/10.5194/egusphere-2025-4659.

Cui, Z., S. Davies, K. S. Carslaw, and A. Blyth, 2011: The response of precipitation to aerosol through riming and melting in deep convective clouds. *Atmospheric chemistry and physics*, **11 (7)**, 3495–3510, https://doi.org/10.5194/acp-11-3495-2011.

Davolio, S., A. Volonté, A. Manzato, A. Pucillo, A. Cicogna, and M. E. Ferrario, 2015: Mechanisms producing different precipitation patterns over north-eastern Italy: insights from HyMeX-SOP1 and previous events. *Quarterly Journal of the Royal Meteorological Society*, **142**, 188–205, https://doi.org/10.1002/qj.2731.

de la Torre, A., V. Daniel, R. Tailleux, and H. Teitelbaum, 2004: A deep convection event above the Tunuyán valley near the Andes mountains. *Monthly Weather Review*, **132 (9)**, 2259–2268, https://doi.org/10.1175/1520-0493(2004)132<2259:adceat>2.0.co;2.

Demko, J. C., and B. Geerts, 2010: A numerical study of the evolving convective boundary layer and orographic circulation around the santa catalina mountains in arizona. Part II: Interaction with deep convection. *Monthly Weather Review*, **138 (9)**, 3603–3622, https://doi.org/10.1175/2010MWR3318.1.

Demko, J. C., B. Geerts, Q. Miao, and J. A. Zehnder, 2009: Boundary layer energy transport and cumulus development over a heated mountain: An observational study. *Monthly Weather Review*, **137 (1)**, 447–468, https://doi.org/10.1175/2008MWR2467.1.

Ducrocq, V., and Coauthors, 2013: HyMeX-SOP1: The field campaign dedicated to heavy precipitation and flash flooding in the northwestern mediterranean. *Bulletin of the American Meteorological Society*, **95 (7)**, 1083–1100, https://doi.org/10.1175/bams-d-12-00244.1.

Dye, J. E., and P. V. Hobbs, 1968: The Influence of Environmental Parameters on the Freezing and Fragmentation of Suspended Water Drops. *Journal of the Atmospheric Sciences*, **25 (1)**, 82–96, https://doi.org/10.1175/1520-0469(1968)025<0082:tioepo>2.0.co;2, URL https://doi.org/10.1175/1520-0469(1968)025<0082:tioepo>2.0.co;2, publisher: American Meteorological Society.

Fan, J., Y. Wang, D. Rosenfeld, and X. Liu, 2016: Review of aerosol–cloud interactions: Mechanisms, significance, and challenges. *Journal of the Atmospheric Sciences*, **73 (11)**, 4221–4252, https://doi.org/10.1175/jas-d-16-0037.1.

Fan, J., Y. Zhang, Z. Li, H. Yan, T. Prabhakaran, D. Rosenfeld, and Khain, 2025: Unveiling Aerosol Impacts on Deep Convective Clouds: Scientific Concept, Modeling, Observational Analysis, and Future Direction. *Journal of Geophysical Research Atmospheres*, **130 (15)**, https://doi.org/10.1029/2024jd041931.

Fernández, J., J. Sáenz, and E. Zorita, 2003: Analysis of wintertime atmospheric moisture transport and its variability over southern Europe in the NCEP Reanalyses. *Climate Research*, **23**, 195–215, https://doi.org/10.3354/cr023195.

Field, P. R., R. P. Lawson, P. R. A. Brown, G. Lloyd, C. D. Westbrook, D. Moisseev, A. Miltenberger, A. Nenes, A. Blyth, T. W. Choularton, P. Connolly, J. Buehl, J. Crosier, Z. Cui, C. Dearden, P. J. DeMott, A. I. Flossmann, A. J. Heymsfield, Y. Huang, H. Kalesse-Los, Z. A. Kanji, A. Korolev, A. Kirchgaessner, S. Lasher-Trapp, T. Leisner, G. M. McFarquhar, V. T. J. Phillips, J. L. Stith, and S. Sullivan, 2017: Chapter 7. Secondary Ice Production - current state of the science and recommendations for the future. *Meteorological Monographs*, https://doi.org/10.1175/amsmonographs-d-16-0014.1.

Forster, P., K. C. Armour, T. Storelvmo, W. J. Collins, J.-L. Dufresne, D. J. Frame, L. D.J, T. Mauritsen, P. M.D, M. Watanabe, M. Wild, and Z. H, 2023: The Earth's Energy Budget, Climate Feedbacks and Climate Sensitivity. *Cambridge University Press eBooks*, Cambridge University Press, 923–1054, https://doi.org/10.1017/9781009157896.009.

Gao, X., J. S. Pal, and F. Giorgi, 2006: Projected changes in mean and extreme precipitation over the Mediterranean region from a high resolution double nested RCM simulation. *Geophysical Research Letters*, **33 (3)**, https://doi.org/10.1029/2005gl024954.

Gaßmann, A., and H. J. Herzog, 2008: Towards a consistent numerical compressible non-hydrostatic model using generalized Hamiltonian tools. *Quarterly Journal of the Royal Meteorological Society*, **134 (635)**, 1597–1613, https://doi.org/10.1002/qj.297.

Georgakaki, P., G. Sotiropoulou, E. Vignon, A.-C. Billault–Roux, A. Berne, and A. Nenes, 2022: Secondary ice production processes in wintertime alpine mixed-phase clouds. *Atmospheric chemistry and physics*, **22 (3)**, 1965–1988, https://doi.org/10.5194/acp-22-1965-2022.

Gold, L. W., 1963: CRACK FORMATION IN ICE PLATES BY THERMAL SHOCK. *Canadian Journal of Physics*, **41 (10)**, 1712–1728, https://doi.org/10.1139/p63-172.

Gordon, H., F. Glassmeier, and D. T. McCoy, 2023: An Overview of Aerosol-Cloud Interactions. *Clouds and Their Climatic Impacts: Radiation, Circulation, and Precipitation*, Geophysical Monograph Series, 2024 John Wiley & Sons, https://doi.org/10.1002/9781119700357, iSSN: 0065-8448, 2328-8779 Pages: 13-45.

Grzegorczyk, P., W. Wobrock, A. Canzi, L. Niquet, F. Tridon, and C. Planche, 2024: Investigating secondary ice production in a deep convective cloud with a 3D bin microphysics model: Part II - Effects on the cloud formation and development. *Atmospheric Research*, **314**, 107 797–107 797, https://doi.org/10.1016/j.atmosres.2024.107797.

Grzegorczyk, P., W. Wobrock, A. Dziduch, and C. Planche, 2025: Influence of secondary ice production on cloud and rain properties: analysis of the HYMEX IOP7a heavy-precipitation event. *Atmospheric chemistry and physics*, **25 (17)**, 10 403–10 420, https://doi.org/10.5194/acp-25-10403-2025.

Hallett, J., and S. C. Mossop, 1974: Production of secondary ice particles during the riming process. *Nature*, **249 (5452)**, 26–28, https://doi.org/10.1038/249026a0.

Han, C., C. Hoose, and V. Dürlich, 2024: Secondary ice production in simulated deep convective clouds: a sensitivity study. *Journal of the Atmospheric Sciences*, **81 (5)**, 903–921, https://doi.org/10.1175/jas-d-23-0156.1.

Hande, L. B., C. Engler, C. Hoose, and I. Tegen, 2015: Seasonal variability of Saharan desert dust and ice nucleating particles over Europe. *Atmospheric Chemistry and Physics*, **15 (8)**, 4389–4397, https://doi.org/10.5194/acp-15-4389-2015.

Hande, L. B., C. Engler, C. Hoose, and I. Tegen, 2016: Parameterizing cloud condensation nuclei concentrations during HOPE. *Atmospheric Chemistry and Physics*, **16 (18)**, 12 059–12 079, https://doi.org/10.5194/acp-16-12059-2016.

Hanley, K., R. S. Plant, T. H. M. Stein, R. J. Hogan, J. Nicol, H. Lean, C. Halliwell, and P. Clark, 2014: Mixing-length controls on high-resolution simulations of convective storms. *Quarterly Journal of the Royal Meteorological Society*, **141 (686)**, 272–284, https://doi.org/10.1002/qj.2356.

Hogan, R. J., and A. Bozzo, 2018: A Flexible and Efficient Radiation Scheme for the ECMWF Model. *Journal of Advances in Modeling Earth Systems*, **10 (8)**, 1990–2008, https://doi.org/10.1029/2018ms001364.

Holton, J. R., 2013: *An Introduction to Dynamic Meteorology*. Elsevier BV, https://doi.org/10.1016/c2009-0-63394-8, URL https://doi.org/10.1016/c2009-0-63394-8.

Hoose, C., and O. Möhler, 2012: Heterogeneous ice nucleation on atmospheric aerosols: a review of results from laboratory experiments. *Copernicus Publications*, **12**, 9817–9854, https://doi.org/10.5194/acp-12-9817-2012.

Horak, J., M. Hofer, E. D. Gutmann, A. Gohm, and M. W. Rotach, 2021: A process-based evaluation of the intermediate complexity atmospheric research model (ICAR) 1.0.1. *Geoscientific model development*, **14 (3)**, 1657–1680, https://doi.org/10.5194/gmd-14-1657-2021.

Houston, A. L., and D. Niyogi, 2007: The sensitivity of convective initiation to the lapse rate of the active cloud-bearing layer. *Monthly Weather Review*, **135 (9)**, 3013–3032, https://doi.org/10.1175/mwr3449.1.

Ickes, L., A. Welti, C. Hoose, and U. Lohmann, 2014: Classical nucleation theory of homogeneous freezing of water: thermodynamic and kinetic parameters. *Physical Chemistry Chemical Physics*, **17 (8)**, 5514–5537, https://doi.org/10.1039/c4cp04184d.

Kalthoff, N., M. Kohler, C. Barthlott, B. Adler, S. Mobbs, U. Corsmeier, K. Träumner, T. Foken, R. Eigenmann, L. Krauss, S. Khodayar, and P. D. Girolamo, 2010: The dependence of convection-related parameters on surface and boundary-layer conditions over complex terrain. *Quarterly Journal of the Royal Meteorological Society*, **137**, 70–80, https://doi.org/10.1002/qj.686.

Kanji, Z. A., L. A. Ladino, H. Wex, Y. Boose, M. Burkert-Kohn, D. J. Cziczo, and M. Krämer, 2017: Overview of Ice Nucleating Particles. *Meteorological Monographs*, **58**, https://doi.org/10.1175/amsmonographs-d-16-0006.1.

Khain, A. P., K. D. Beheng, A. Heymsfield, A. Korolev, S. O. Krichak, Z. Levin, M. Pinsky, V. Phillips, T. Prabhakaran, A. Teller, S. C. v. d. Heever, and J.-I. Yano, 2015: Representation of microphysical processes in cloud-resolving models: Spectral (bin) microphysics versus bulk parameterization. *Reviews of Geophysics*, **53 (2)**, 247–322, https://doi.org/10.1002/2014rg000468.

Kirshbaum, D. J., 2010: Cloud-resolving simulations of deep convection over a heated mountain. *Journal of the Atmospheric Sciences*, **68 (2)**, 361–378, https://doi.org/10.1175/2010jas3642.1.

Kirshbaum, D. J., 2016: On upstream blocking over heated mountain ridges. *Quarterly Journal of the Royal Meteorological Society*, **143 (702)**, 53–68, https://doi.org/10.1002/qj.2945.

Kirshbaum, D. J., B. Adler, N. Kalthoff, C. Barthlott, and S. Serafin, 2018: Moist orographic convection: Physical mechanisms and links to surface-exchange processes. *Atmosphere*, **9 (3)**, 80–80, https://doi.org/10.3390/atmos9030080.

Kirshbaum, D. J., and D. R. Durran, 2004: Factors governing cellular convection in orographic precipitation. *Journal of the Atmospheric Sciences*, **61 (6)**, 682–698, https://doi.org/10.1175/1520-0469(2004)061<0682:fgccio>2.0.co;2.

Korolev, A., G. M. McFarquhar, P. R. Field, C. Franklin, P. Lawson, Z. Wang, E. Williams, S. J. Abel, D. Axisa, S. Borrmann, J. Crosier, J. Fugal, M. Krämer, U. Lohmann, O. Schlenczek, M. Schnaiter, and M. Wendisch, 2017: Mixed-Phase Clouds: Progress and Challenges. *Meteorological Monographs*, **58**, https://doi.org/10.1175/amsmonographs-d-17-0001.1.

Korolev, A., I. Heckman, M. Wolde, A. S. Ackerman, A. M. Fridlind, L. A. Ladino, R. P. Lawson, J. A. Milbrandt, and E. Williams, 2020: A new look at the environmental conditions favorable to secondary ice production. *Atmospheric chemistry and physics*, **20 (3)**, 1391–1429, https://doi.org/10.5194/acp-20-1391-2020.

Kuntze, P., 2019: Sensitivity of Mixed-Phase Low-Level Clouds to Secondary Ice Formation Processes. M.S. thesis, Karlsruhe Institute of Technology, Karlsruhe, URL https://www.imk-tro.kit.edu/english/5734.php.

Kärcher, B., J. Hendricks, and U. Lohmann, 2006: Physically based parameterization of cirrus cloud formation for use in global atmospheric models. *Journal of Geophysical Research: Atmospheres*, **111**, https://doi.org/10.1029/2005jd006219.

Kärcher, B., and U. Lohmann, 2002: A parameterization of cirrus cloud formation: Homogeneous freezing of supercooled aerosols. *Journal of Geophysical Research Atmospheres*, **107**, https://doi.org/10.1029/2001jd000470.

Lamb, D., and J. Verlinde, 2011: *Physics and Chemistry of Clouds*. Cambridge University Press, https://doi.org/10.1017/cbo9780511976377, cambridge University Press eBooks.

Lauber, A., J. Henneberger, C. Mignani, F. Ramelli, J. T. Pasquier, J. Wieder, M. Hervo, and U. Lohmann, 2021: Continuous secondary-ice production initiated by updrafts through the melting layer in mountainous regions. *Atmospheric chemistry and physics*, **21 (5)**, 3855–3870, https://doi.org/10.5194/acp-21-3855-2021.

Lauber, A., A. Kiselev, T. Pander, P. Handmann, and T. Leisner, 2018: Secondary ice formation during freezing of levitated droplets. *Journal of the Atmospheric Sciences*, **75 (8)**, 2815–2826, https://doi.org/10.1175/jas-d-18-0052.1.

Leuenberger, D., M. Koller, O. Fuhrer, and C. Schär, 2010: A Generalization of the SLEVE Vertical Coordinate. *Monthly Weather Review*, **138 (9)**, 3683–3689, https://doi.org/10.1175/2010mwr3307.1.

Levizzani, V., and C. Kidd, 2025: Cloud Physics. *Precipitation: From Cloud Physics to Satellite Observations*, Springer, 47–146, https://doi.org/10.1007/978-3-031-97096-2_3.

Lin, Y., S. Chiao, T.-A. Wang, M. L. Kaplan, and R. P. Weglarz, 2001: Some common ingredients for heavy orographic rainfall. *Weather and Forecasting*, **16 (6)**, 633–660, https://doi.org/10.1175/1520-0434(2001)016<0633:scifho>2.0.co;2.

Markowski, P., and Y. Richardson, 2010: *Mesoscale meteorology in midlatitudes*. John Wiley & Sons, 2011, https://doi.org/10.1002/9780470682104.

Mason, B. J., and J. Maybank, 1960: The fragmentation and electrification of freezing water drops. *Quarterly Journal of the Royal Meteorological Society*, **86 (368)**, 176–185, https://doi.org/10.1002/qj.49708636806.

Metzger, J., C. Barthlott, and N. Kalthoff, 2014: Impact of upstream flow conditions on the initiation of moist convection over the island of Corsica. *Atmospheric Research*, **145**, 279–296, https://doi.org/10.1016/j.atmosres.2014.04.011.

Miltenberger, A., P. R. Field, A. Hill, P. Rosenberg, B. Shipway, J. M. Wilkinson, R. Scovell, and A. Blyth, 2018: Aerosol–cloud interactions in mixed-phase convective clouds – Part 1: Aerosol perturbations. *Atmospheric chemistry and physics*, **18 (5)**, 3119–3145, https://doi.org/10.5194/acp-18-3119-2018.

Mroz, K., A. Battaglia, and A. M. Fridlind, 2024: Enhancing consistency of microphysical properties of precipitation across the melting layer in dual-frequency precipitation radar data. *Atmospheric Measurement Techniques*, **17 (5)**, 1577–1597, https://doi.org/10.5194/amt-17-1577-2024.

Nicosia, A., M. Piazza, G. Santachiara, and F. Belosi, 2017: Heterogeneous nucleation of ice in the atmosphere. *Journal of Physics Conference Series*, **841**, 12 028–12 028, https://doi.org/10.1088/1742-6596/841/1/012028.

Nugent, A. D., R. B. Smith, and J. R. Minder, 2014: Wind speed control of tropical orographic convection. *Journal of the Atmospheric Sciences*, **71 (7)**, 2695–2712, https://doi.org/10.1175/jas-d-13-0399.1.

Onishi, R., and K. Takahashi, 2012: A Warm-Bin–Cold-Bulk Hybrid Cloud Microphysical Model*. *Journal of the Atmospheric Sciences*, **69 (5)**, 1474–1497, https://doi.org/10.1175/jas-d-11-0166.1.

Oraltay, R. G., and J. Hallett, 1989: Evaporation and melting of ice crystals: A laboratory study. *Atmospheric Research*, **24**, 169–189, https://doi.org/10.1016/0169-8095(89)90044-6.

Phillips, V. T. J., 2024: A theory for the balance between warm rain and ice crystal processes of precipitation in mixed-phase clouds. *Journal of the Atmospheric Sciences*, **81 (2)**, 317–339, https://doi.org/10.1175/jas-d-23-0054.1.

Phillips, V. T. J., J.-I. Yano, and A. Khain, 2017: Ice Multiplication by Breakup in Ice–Ice Collisions. Part I: Theoretical Formulation. *Journal of the Atmospheric Sciences*, **74 (6)**, 1705–1719, https://doi.org/10.1175/jas-d-16-0224.1.

Raschendorfer, M., 2001: The new turbulence parameterization of LM. *COSMO Newsletter*, **1**, 89–97, URL http://www.cosmo-model.org.

Reinert, D., D. Rieger, and F. Prill, 2024: ICON Tutorial 2024: Working with the ICON Model. *German Meteorological Service*, https://doi.org/10.5676/DWD_PUB/NWV/ICON_TUTORIAL2024.

Ricard, D., V. Ducrocq, and L. Auger, 2011: A climatology of the mesoscale environment associated with heavily precipitating events over a northwestern mediterranean area. *Journal of Applied Meteorology and Climatology*, **51 (3)**, 468–488, https://doi.org/10.1175/jamc-d-11-017.1.

Robinson, F. J., S. C. Sherwood, and Y. Li, 2008: Resonant response of deep convection to surface hot spots. *Journal of the Atmospheric Sciences*, **65 (1)**, 276–286, https://doi.org/10.1175/2007jas2398.1.

Roe, G. H., 2005: Orographic precipitation. *Annual Review of Earth and Planetary Sciences*, **33 (1)**, 645–671, https://doi.org/10.1146/annurev.earth.33.092203.122541.

Romero, R., C. A. Doswell, and C. Ramis, 2000: Mesoscale numerical study of two cases of long-lived quasi-stationary convective systems over eastern spain. *Monthly Weather Review*, **128 (11)**, 3731–3751, https://doi.org/10.1175/1520-0493(2001)129<3731:mnsotc>2.0.co;2.

Rosenfeld, D., U. Lohmann, G. B. Raga, C. D. O'Dowd, M. Kulmala, S. Fuzzi, A. Reissell, and M. O. Andreae, 2008: Flood or drought: How do aerosols affect precipitation? *Science*, **321 (5894)**, 1309–1313, https://doi.org/10.1126/science.1160606.

Rutledge, S. A., and P. V. Hobbs, 1984: The Mesoscale and Microscale Structure and Organization of Clouds and Precipitation in Midlatitude Cyclones. XII: A Diagnostic Modeling Study of Precipitation Development in Narrow Cold-Frontal Rainbands. *Journal of the Atmospheric Sciences*, **41 (20)**, 2949–2972, https://doi.org/10.1175/1520-0469(1984)041<2949:tmamsa>2.0.co;2.

Schultz, D. M., P. N. Schumacher, and C. A. Doswell, 2000: The intricacies of instabilities. *Monthly Weather Review*, **128 (12)**, 4143–4148, https://doi.org/10.1175/1520-0493(2000)129<4143:tioi>2.0.co;2.

Segal, Y., and Khain, 2006: Dependence of droplet concentration on aerosol conditions in different cloud types: Application to droplet concentration parameterization of aerosol conditions. *Journal of Geophysical Research Atmospheres*, **111**, https://doi.org/10.1029/2005jd006561.

Seifert, A., and K. D. Beheng, 2006: A two-moment cloud microphysics parameterization for mixed-phase clouds. Part 1: Model description. *Meteorology and Atmospheric Physics*, **92**, 45–66, https://doi.org/10.1007/s00703-005-0112-4.

Seifert, A., C. Köhler, and K. Beheng, 2012: Aerosol-cloud-precipitation effects over Germany as simulated by a convective-scale numerical weather prediction model. *Atmospheric chemistry and physics*, **12 (2)**, 709–725, https://doi.org/10.5194/acp-12-709-2012.

Seinfeld, J. H., and S. N. Pandis, 2016: *Atmospheric Chemistry and Physics From Air Pollution to Climate Change*. 3rd ed., John Wiley & Sons.

Smith, R. B., 1989: Hydrostatic airflow over mountains. *Advances in Geophysics*, Vol. 31, Elsevier, 1–41, URL https://linkinghub.elsevier.com/retrieve/pii/S0065268708600527.

Sotiropoulou, G., L. Ickes, A. Nenes, and A. M. L. Ekman, 2021a: Ice multiplication from ice–ice collisions in the high Arctic: sensitivity to ice habit, rimed fraction, ice type and uncertainties in the numerical description of the process. *Atmospheric chemistry and physics*, **21 (12)**, 9741–9760, https://doi.org/10.5194/acp-21-9741-2021.

Sotiropoulou, G., E. Vignon, G. Young, H. Morrison, S. O'Shea, T. Lachlan-Cope, A. Berne, and A. Nenes, 2021b: Secondary ice production in summer clouds over the Antarctic coast: an underappreciated process in atmospheric models. *Atmospheric chemistry and physics*, **21 (2)**, 755–771, https://doi.org/10.5194/acp-21-755-2021.

Sullivan, S., C. Barthlott, J. Crosier, I. Zhukov, A. Nenes, and C. Hoose, 2018a: The effect of secondary ice production parameterization on the simulation of a cold frontal rainband. *Atmospheric chemistry and physics*, **18 (22)**, 16 461–16 480, https://doi.org/10.5194/acp-18-16461-2018.

Sullivan, S., C. Hoose, A. Kiselev, T. Leisner, and A. Nenes, 2018b: Initiation of secondary ice production in clouds. *Atmospheric chemistry and physics*, **18 (3)**, 1593–1610, https://doi.org/10.5194/acp-18-1593-2018.

Sun, M., P. Connolly, P. R. Field, and A. Blyth, 2025: Secondary ice production affects tropical convective clouds under different aerosol conditions. *Copernicus Publications*, https://doi.org/10.5194/egusphere-2025-5665.

Takahashi, T., Y. Nagao, and Y. Kushiyama, 1995: Possible High Ice Particle Production during Graupel–Graupel Collisions. *Journal of the Atmospheric Sciences*, **52 (24)**, 4523–4527, https://doi.org/10.1175/1520-0469(1995)052<4523:phippd>2.0.co;2.

Tao, W., X. Li, Khain, T. Matsui, S. Lang, and J. Simpson, 2007: Role of atmospheric aerosol concentration on deep convective precipitation: Cloud-resolving model simulations. *Journal of Geophysical Research Atmospheres*, **112**, https://doi.org/10.1029/2007jd008728.

Trapp, R. J., 2013: Mesoscale-convective processes in the atmosphere. *Cambridge University Press*, https://doi.org/10.1017/cbo9781139047241, iSBN: 9780521889421, 9781139047241.

Vali, G., P. J. DeMott, O. Möhler, and T. F. Whale, 2015: Technical Note: A proposal for ice nucleation terminology. *Atmospheric chemistry and physics*, **15 (18)**, 10 263–10 270, https://doi.org/10.5194/acp-15-10263-2015.

Vardiman, L., 1978: The Generation of Secondary Ice Particles in Clouds by Crystal–Crystal Collision. *Journal of the Atmospheric Sciences*, **35 (11)**, 2168–2180, https://doi.org/10.1175/1520-0469(1978)035<2168:tgosip>2.0.co;2.

Wallentin, G. L., 2025: The Microphysical and Radiative Interactions of Arctic Multilayer Clouds. *KIT Library repository*, https://doi.org/10.5445/IR/1000179667.

Wang, P. K., and W. Ji, 2000: Collision Efficiencies of Ice Crystals at Low–Intermediate Reynolds Numbers Colliding with Supercooled Cloud Droplets: A Numerical Study. *Journal of the Atmospheric Sciences*, **57 (8)**, 1001–1009, https://doi.org/10.1175/1520-0469(2000)057<1001:ceoica>2.0.co;2.

Wang, Y., and J. Wu, 2022: Overview of the application of orographic data in numerical weather prediction in complex orographic areas. *Advances in Meteorology*, **2022**, 1–13, https://doi.org/10.1155/2022/1279625.

Wilson, J. W., and W. E. Schreiber, 1986: Initiation of convective storms at radar-observed boundary-layer convergence lines. *Monthly Weather Review*, **114 (12)**, 2516–2536, https://doi.org/10.1175/1520-0493(1986)114<2516:iocsar>2.0.co;2.

Zardi, D., and C. D. Whiteman, 2012: Diurnal mountain wind systems. *Springer atmospheric sciences*, Springer Nature (Netherlands), 35–119, https://doi.org/10.1007/978-94-007-4098-3_2, iSSN: 2194-5225, 2194-5217.

Zängl, G., D. Reinert, P. Rípodas, and M. Baldauf, 2014: The ICON (ICOsahedral Non-hydrostatic) modelling framework of DWD and MPI-M: Description of the non-hydrostatic dynamical core. *Quarterly Journal of the Royal Meteorological Society*, **141 (687)**, 563–579, https://doi.org/10.1002/qj.2378.

Acknowledgments

First, I would like to thank Prof. Dr. Corinna Hoose for the warm welcome to the group and for her continuous support: not only for this thesis, but also for being open to discussing my future interests and for providing personalized reference letters. Thank you very much for your support and valuable feedback!

A big and special thank you goes to my supervisors, Dr. Gabriella Wallentin and Dr. Christian Barthlott. Your guidance, supervision, and continuous feedback consistently helped me improve and think from different perspectives. Thank you for always being available when I felt stuck or faced technical difficulties. Your support made a significant positive difference. I learned a lot from both of you, both personally and regarding good scientific practices. Thanks a ton!

I would also like to thank Prof. Dr. Michael Kunz for his valuable feedback on my specialization phase presentation and for his role as co-advisor.

Thank you to Ariane, Alejandro, and Ed for the time we spent together whenever I visited Karlsruhe during our master's studies. I truly enjoyed our meals, talks and laughter together!

Thank you to one of my best friends, Thomas, for always taking an interest in my progress. You were the first person to know when I started this master's program, and you encouraged me throughout. Thanks a lot and best of luck with finishing your PhD!

Above all, I would like to thank my beloved partner, Alison, for being in my life. Your belief in me made all the difference in the world. Thanks for listening patiently to all my concerns, ideas and achievements throughout my studies. Thanks for helping me whenever I needed it, whether through proofreading or presentation ideas. You are my strongest pillar of support, and I feel incredibly lucky to have you in my life.

I would like to extend my thanks to my colleagues at Öko-Recherche GmbH for giving me the flexibility to focus fully on completing my thesis in the final three months leading up to the deadline.

Finally, I thank my parents and my sister for their endless support throughout my studies and for always supporting my ideas.

Erklärung

Ich versichere wahrheitsgemäß, die Arbeit selbstständig verfasst, alle benutzten Hilfsmittel vollständig und genau angegeben und alles kenntlich gemacht zu haben, was aus Arbeiten anderer unverändert oder mit Abänderungen entnommen wurde sowie die Satzung des KIT zur Sicherung guter wissenschaftlicher Praxis in der jeweils gültigen Fassung beachtet zu haben.

Karlsruhe, den 12.01.2026

(Bhawuk Verma)